ELECTRODEPOSITION OF TUNABLE ZINC OXIDE NANOMATERIALS FOR OPTICAL APPLICATIONS

ELECTRODEPOSITION OF TUNABLE ZINC OXIDE NANOMATERIALS FOR OPTICAL APPLICATIONS

By Joey Pavlovski, B.Sc.

A Thesis Submitted to the School of Graduate Studies in Partial Fulfillment of the Requirement for the Degree Master of Applied Science.

McMaster University © Copyright by Joey Pavlovski, August 2013

MASTER OF APPLIED SCIENCE (2013) McMaster University
Engineering Physics Hamilton, Ontario

TITLE: Electrodeposition of Tunable ZnO Nanomaterials for Optical Applications

AUTHOR: Joey Pavlovski (McMaster University)

SUPERVISOR: Professor L. Soleymani

NUMBER OF PAGES: X, 155

Abstract

Renewable energy technologies and the development of cleaner and more environmentally friendly power have been at the forefront of research for the past few decades. Photovoltaic systems – systems that convert photon energy to electrical energy – are at the center of these research efforts. Decreasing the cost of energy production, through increasing the power conversion efficiency or decreasing the device cost, is a key factor in widespread use of these energy production systems. To increase the energy conversion efficiency, ideally, all useful photons should be absorbed by the solar cell; however, due to the large discontinuity in the refractive index at the solar cell/air interface, a large fraction of incidence light is lost due to reflection (30% loss in crystalline silicon cells). The currently used single and double layer anti-reflection coatings reduce the reflection losses, but their optimal performance is limited to a narrow range of wavelengths and angles of incidence. Moth-eye anti-reflection coatings are composed of patterned single layer films having a gradual decrease in refractive index from the solar cell surface to air. This study is focused on developing an inexpensive method for direct deposition of patterned films – in the form of moth-eye anti-reflection coatings – on solar cell surface.

In this research, the creation of moth-eye anti-reflection coatings has been attempted through the process of electrodeposition. ZnO was chosen for the thin film material, and the ability to develop the required moth-eye structure by changing the electrodeposition parameters including temperature, applied potential, type and concentration of solution-borne species, and type of substrate was investigated. Using this method, pyramidal and hemispherical structures with a 100-200 nm diameter and 100-200 nm height were created directly on ITO substrates. Similar structures were also developed on silicon substrates. The anti-reflection properties of ZnO-coated silicon substrates were investigated by comparing their broadband and broad angle reflection-mode UV-VIS spectrum with uncoated silicon. The optimized ZnO-coated silicon substrate showed a reflectance of at most 20% for wavelengths between 400-1500 nm at angles of incidence less than 50^{O}.

Acknowledgements

There are many people who have helped me in completing my thesis over the past two years. First and foremost, I would like to offer my sincere gratitude to my supervisor, Dr. Leyla Soleymani. Her guidance and experience were the major contributing factors in my development as a researcher.

Many thanks to my research group/partner Christine Gabardo, who helped me with the building of our lab from the ground up.

From the Center for Emerging Device Technology (CEDT), Doris Stevanovic and Zhilin Peng have assisted me greatly with training and learning all safety procedures. I was able to sputter and conduct photolithography processes with their guidance.

I would like to acknowledge the staff at the Canadian Centre for Electron Microscopy (CCEM). In Particular, Chris Butcher whose knowledge and experience helped to develop my skills on the JEOL 7000 scanning electron microscope.

I would also like to thank Victoria Jarvis, an XRD Specialist in the McMaster Analytical X-ray Diffraction Facility. Her assistance and knowledge has helped me understand how to perform and analyze XRD composition data.

Lastly, I would like to thank my family and Ewa Gajek, whose support and encouragement has allowed me to successfully complete my Master's degree in engineering physics.

Table of Contents

List of Figures

Chapter 1: Introduction

1.1 Background

The solar cell industry has grown tremendously over the last decade, and generating sufficient renewable energy for the foreseeable future has become one of society's main goals. Due to the environmental risks associated with other forms of energy production, renewable energy has been at the forefront of modern day research. With this in mind, the advancement in photovoltaics has been apparent all over the world. In the United States, the California Energy Commission has estimated the cost of producing 1MWH of energy using solar technology to be between \$116 - \$312 USD compared to coal which is between \$74 - \$88 USD, and nuclear energy which costs approximately \$67 USD per 1MWH.[1] It is clear therefore that at this point in time, electrical energy generated using solar power is not cost effective compared to other mainstream sources of energy.

There have been three generations of solar cells developed to date. As depicted in Figure 1, the first generation solar cells demonstrate moderate power conversion efficiency (up to 20% efficiency) but at a very high cost (\$200-\$500 per m^2).[2] The second generation were produced at a lower cost (~\$100 per m^2) but also had a lower efficiency (approximately 12%).[2] Lastly, the third generation cells were created to demonstrate a high power conversion efficiency (up to 80%

efficiency) at a relatively low cost (under \$200).[2] These third generation cells are still in research and development however, and are being used primarily in satellite photovoltaics in space due to the increased intensity from the sun outside of our atmosphere. For residential applications, silicon and thin film technology has been used in the past decade and within the last few years, concentrator photovoltaics with the use of III-V semiconductors have begun implanting themselves in the commercial market. One of the main components that can be optimized further to reduce the cost and increase the efficiency in all three generations of solar cells is the anti-reflection coating (ARC).

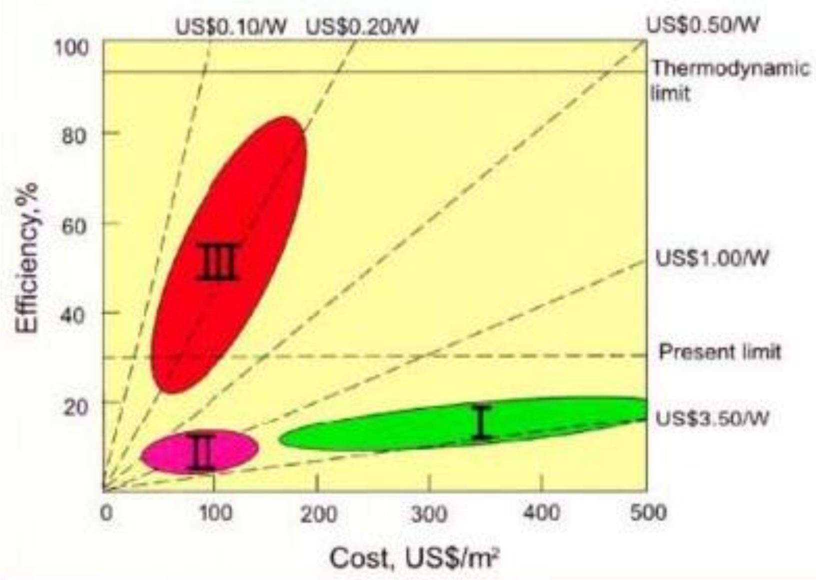

Figure 1: The three generations of solar cells.[2]

Currently, both single and double layer anti-reflection coatings are in use for industrial applications in photovoltaics. In a single layer coating however, the reflectance is zero only at a given wavelength and not over the entire spectrum.

A double layer coating reduces the effective reflectance over a broader range, relative to a single layer coating. The materials used in commercial single layer coatings are silicon nitrides and titanium oxide on silicon solar cells. This is due to their appropriate refractive indexes and their ability to be processed at temperatures as low as 200ºC.[3] Silicon dioxide is also used and though it provides better surface passivation, it is more expensive as it is processed at high temperatures above 900ºC.[3]

ARCs can be deposited on solar cells in multiple ways. These include chemical vapor deposition, plasma-enhanced chemical vapor deposition, spray coating, spin coating, or screen printing. While spray coating, spin coating, and screen printing are significantly less expensive than CVD-based methods, they are not suitable for depositing coatings of uniform thickness on textured surfaces.[4]

Generation III solar cells are still relatively new for industry use, but some companies have begun manufacturing them at a large scale. These third generation solar cells (III-V semiconductors) also have double layer ARCs; usually a TiO_2 and an Al_2O_3 because of their appropriate refractive indexes. Though it is more expensive to process these double layer ARCs, they offer a broader range over which reflection is reduced in comparison to single layer ARCs. There is a need for an inexpensive single layer coating that can achieve broadband anti-reflection properties in the photovoltaic industry.

Another type of ARC which is still primarily in the research and development phase is the moth-eye ARC. This is a nature-inspired anti-reflection coating that reduces the reflection from light over broadband of wavelengths and large angles of incidence.[5–7] This is achieved due to the process of creating high aspect ratio nanoscale protuberances – similar to those found on the surface of moth corneas – on the surface of the substrate. The moth-eye coating is a compelling candidate for broadband and broad angle anti-reflection coatings applicable to photovoltaic cells. A reduction of at least 2-3% in reflectance has been reported over the 400-1200 nm wavelength range when comparing moth-eye anti-reflective coatings (<1% reflectance) and double layer anti-reflective coatings (<3-4% reflectance) at the time of day when the solar irradiance is most intense (normal incidence, around midday on the same day and location).[8] The development of low-cost and low-temperature methods applicable to large volume production of these coatings is currently under intense investigation.[9–12]

Electrodeposition is a bottom-up fabrication method where ions are reduced and deposited at the surface of an electrode with the application of electric potential or current. In addition to being low-temperature and low-cost, electrodeposition allows for precise and facile control over the density, size, and morphology of deposited particles. Consequently, direct electrodeposition of moth-eye ARCs on solar cell substrates holds great promise for large volume fabrication of such coatings for industrial applications. This work aims at developing a moth-eye array directly on solar cell substrates and without the need for post-deposition patterning by controlling the electrodeposition parameters including the temperature, applied potential, concentration and type of reaction precursors, and time. A more comprehensive list of thesis objectives is presented in the following section.

1.2 Objectives

The major goal for this research project was to create a self-assembled moth-eye array through the process of electrodeposition at low temperature (<100ºC) and low cost. A self-assembled array eliminates the need for a patterning step in the ARC manufacturing process; eliminating this step can allow for an inexpensive coating to be produced in large volumes at an industry level. This work focuses on:

1) The fabrication of tunable ZnO nanostructures using electrodeposition and studying the role of electrodeposition parameters including temperature, applied potential, type and concentration of the reaction precursors, and time on the morphology, geometry and size of these nanostructures.

2) The characterization of these ZnO nanostructures to show the tunability and control over multiple length scales: the 100-400 nm length scale and the 1-50 µm length scale.

3) The development of patterning techniques to pattern the ZnO nanostructures using a conventional top-down technique such as photolithography.

4) The tuning of the optical properties of substrate materials and the creation of anti-reflection coatings – with hemispherical protuberances similar to those observed in moth's eyes – that reduce reflectance from solar cell surfaces.

1.3 Outline

This thesis is comprised of 6 other chapters. Chapter 2 provides the background and theory behind anti-reflection coatings. The moth-eye anti-reflection coating design requirements, fabrication limitations, and previously developed patterning techniques are included as well. In Chapter 3, electrodeposition, ZnO as a material, and ZnO electrodeposition are described. Chapter 4 discusses the techniques and procedures used for ZnO electrodeposition in this research, including deposition techniques such as sputtering, as well as electrochemical methods for thin film deposition. The procedures used for the electrodeposition and patterning of ZnO are also included in this chapter. Chapter 5 describes the characterization techniques and the theoretical and practical aspects of the devices used for analyzing the structural and optical properties of the ZnO nanostructures. Chapter 6 includes the results and corresponding discussions of the characterization methods used, such as scanning electron microscopy (SEM), X-ray diffraction (XRD), and UV-Vis Spectroscopy. Lastly, Chapter 7 provides the final conclusions of this research and outlines some recommended future work that may be conducted.

Chapter 2: Anti-Reflection Coatings

2.1 Anti-Reflection Coatings – Theory and Background

The purpose of an anti-reflection coating (ARC) is to reduce the amount of light reflected from a surface. This coating is designed to be transparent so that light is able to transmit through the media while at the same time minimizing reflected light. From optical theory, incoming light is described as an electromagnetic wave which when interacts with a medium, can either reflect off the surface, transmit through the medium, or become absorbed in the medium. Absorption involves the raising of a molecule to a higher internal energy level which can be completed through three transitions:

- Rotational: a molecule rotating at a definite energy level which through absorption goes to a higher rotational energy level
- Vibrational: vibrating molecules or atoms relative to each other absorb energy and move to a higher vibrational energy
- Electronic: transitions which cause electrons to increase to a higher energy level.[13]

These transitions will be described further in Section 5.4, but if the molecule does not go to a higher internal energy level then there is no absorption.[13] There are three factors that affect the reflectance and transmission of light: the refractive index of the media which is defined as n=c/v (where the refractive index is the ratio between the speed of light in free space over the speed of light in the medium), the angle of incident light (θ), and the polarization of the incident light. The Fresnel equations are used to calculate both transmission and reflection coefficients. A simplified derivation is presented below:[14,15]

In Figure 2, a linearly polarized electromagnetic wave that travels to a point P between two media is defined by an electric field and a magnetic field in that plane of incidence. When the electric field is oscillating orthogonally to the plane of incidence and the magnetic field component lies in the plane of incidence, this is known as transverse electric (TE) mode of propagation. However if the magnetic field component of the wave were oscillating orthogonally to the plane of incidence while the electric field component were to lie in the plane of incidence, then the mode of propagation would instead be transverse magnetic (TM).

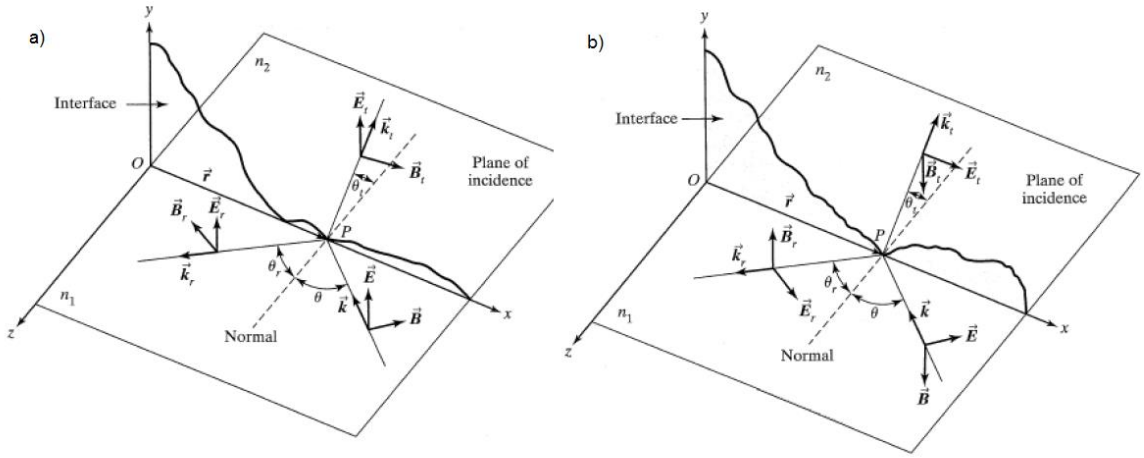

Figure 2: a) TE-polarized light incident on the boundary between two media, b) TM-polarized light incident on the boundary between two media.[15]

For **TE** polarized light, it is required that at the boundary, the components of the E-field parallel to the interface be continuous. Therefore the amplitudes of the components must be:

$$E_i + E_r = E_t \qquad (1)$$

Similarly are the parallel components for the magnetic field:

$$B_i\cos(\theta) - B_r\cos(\theta) = B_t\cos(\theta_t) \qquad (2)$$

For **TM** polarized light, the components parallel to the interface are still required at the boundary:

$$-B_i\ B_r = -B_t \qquad (3)$$

$$E_i\cos(\theta) + E_r\cos(\theta) = E_t\cos(\theta_t) \qquad (4)$$

By using the relation between electric and magnetic fields, E = (c/n)B, equation (2) and (3) can be rewritten:

$$E_i + E_r = E_t \qquad (1)$$

Equation (2) becomes:

$$n_1E_i\cos(\theta_i) - n_1E_r\cos(\theta_i) = n_2E_t\cos(\theta_t) \qquad (5)$$

Equation (3) becomes:

$$-n_1E_i + n_1E_r = -n_2E_t \qquad (6)$$

$$E_i\cos(\theta_i) + E_r\cos(\theta_i) = E_t\cos(\theta_t) \qquad (4)$$

Therefore the TE equations (1) and (5) and the TM equations (4) and (6) can be solved by eliminating E_t and defining the ratio $r = E_r/E_i$ for reflection:

$$r_{TE} = \frac{\cos(\theta_i) - (n_2/n_1)\cos(\theta_t)}{\cos(\theta_i) + (n_2/n_1)\cos(\theta_t)} \tag{7}$$

$$r_{TM} = \frac{\cos(\theta_t) - (n_2/n_1)\cos(\theta_i)}{\cos(\theta_t) + (n_2/n_1)\cos(\theta_i)} \tag{8}$$

By using the trigonometric equation $1= \cos^2(\theta) + \sin^2(\theta)$ and Snell's law for refraction $[n_1\sin(\theta_i) = n_2\sin(\theta_t)]$ we can eliminate the transmission angle:

$$r_{TE} = \frac{\cos(\theta_i) - (n_2/n_1)\sqrt{1-[(n_1/n_2)\sin(\theta_i)]^2}}{\cos(\theta_i) + (n_2/n_1)\sqrt{1-[(n_1/n_2)\sin(\theta_i)]^2}}$$

$$r_{TM} = \frac{\sqrt{1-[(n_1/n_2)\sin(\theta_i)]^2} - (n2/n1)\cos(\theta_i)}{\sqrt{1-[(n_1/n_2)\sin(\theta_i)]^2} + (n_2/n_1)\cos(\theta_i)}$$

Since the energy of reflection is proportional to the absolute square of the electric field amplitude, the reflection coefficients R_{TE} and R_{TM} are:

$$R_{TE} = | r_{TE} |^2 \qquad R_{TM} = | r_{TM} |^2$$

For unpolarized light, the linear combination of both reflection coefficients are used and the transmission coefficient for each mode of propagation is $T = 1 - R$.

An anti-reflection coating eliminates or reduces reflections through the interference of light, which refers to interference of light reflected from two interfaces; the air/coating interface and the coating/substrate interface. At the first interface, the light wave with wavelength λ is reflected. If the wave reflected at the second interface experiences a phase shift of λ/2, then the two reflected waves are completely out of phase and undergo destructive interference as depicted in Figure 3. This phase shift between the two refracted light waves is caused by the thickness and refractive index of the intermediate layer.

The optical path length (the path light travels in the medium) is described as:[15]

$$\Delta = 2n_1d \qquad (2.1.1)$$

where the light travels twice the thickness of the intermediate layer (2d) that has a refractive index of n_1. Therefore, to achieve total destructive interference the optical path length has to equal λ/2:[16]

$$\Delta = 2n_1d = \lambda/2 \text{ or } d = \lambda/4n_1$$

If the optical path length difference between the two waves was equal to λ instead, then the two reflected waves would have been in phase and constructive interference would have occurred. From this understanding, at a given refractive index, the thickness of the layer can be adjusted so reflection waves from each interface partake in total destructive interference at one selected wavelength, leaving only transmitted light.

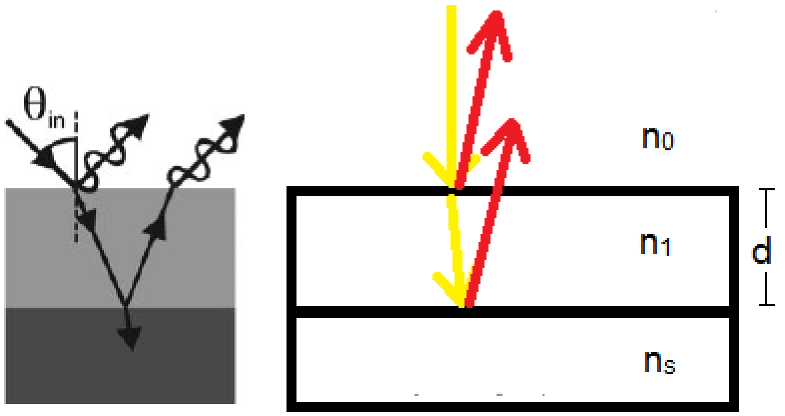

Figure 3: Anti-reflection coating with total destructive interference.[12]

The most optimal refractive index for the intermediate layer can be calculated using the Fresnel equations above. For simplicity, we consider the case where the incident light is normal to the surface of the intermediate layer. Therefore using the Fresnel equation $R_{TE} = R_{TM}$ at 0º incidence, the equation at the first interface (air/intermediate layer) becomes:

$$R_{TE} = R_{TM} = \frac{\{1-(n_1/n_0)\}^2}{\{1+(n_1/n_0)\}^2} \tag{2.1.2}$$

At the second interface (intermediate layer/substrate) it becomes:

$$R_{TE} = R_{TM} = \frac{\{1-(n_s/n_1)\}^2}{\{1+(n_s/n_1)\}^2} \tag{2.1.3}$$

In order to achieve maximum destructive interference, the reflection coefficients at each interface must equal each other. Therefore:

$$n_1/n_0 = n_s/n_1$$

The optimal refractive index for the anti-reflection layer is then given by:[17]

$$n_1 = \sqrt{(n_o * n_s)} \tag{2.1.4}$$

where n_1 is the refractive index of the anti-reflection layer, n_o is the refractive index of the layer on the top side of the coating (ex. air), and n_s is the refractive index of the substrate.

Designing an anti-reflection coating with a thickness that results in destructive interference at only a single wavelength presents a major drawback; the coating reduces the reflection to zero only at that specified wavelength, while the reflection is non-zero at other wavelengths. This is why double layer ARCs are used, as they help to achieve lower reflection values over a broader part of the spectrum. Double layer ARCs function the same way as a single layer ARCs, only now there are three interfaces and two different layers with thicknesses

$d_1=\lambda/4n_1$ and $d_2=\lambda/4n_2$, which is shown in Figure 4. The Fresnel equations can be used to calculate the total reflection with a double layer as well. These layers can now effectively reduce the reflection at two separate wavelengths, consequently reducing the reflection over a broader spectrum.

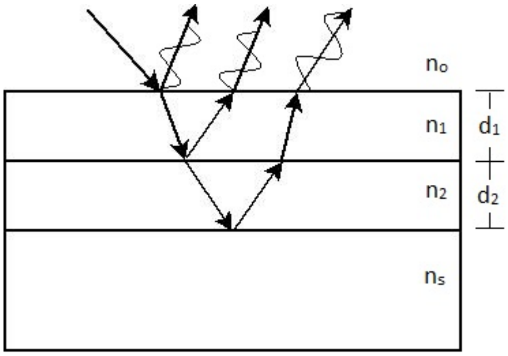

Figure 4: Double layer ARC

2.2 Moth-Eye Anti-Reflection Coating

A study was conducted which recognized that the subwavelength-structured corneas of a nocturnal moth cause them to act as a camouflage at night.[7] This effectively reduces the reflection of incoming light off the moth's eyes, protecting it from predators. The same concept could be adapted in photovoltaics with the use of an anti-reflection coating that behaves in the same way. Figure 5 demonstrates the difference between having a moth-eye coating on the surface of the cornea, versus not having one at all. The effect of a refractive index gradient is observed, which means that the deeper the light penetrates into the material, the larger the effective index of refraction becomes.[6] In order to achieve this gradual change in refractive index, the structures/tapered pillars need to occur with a period d (distance between nearest pillar centre), and have a height h. The basic understanding of this system is that the array's features are on a scale below the wavelength of incident light, so incoming photons do not react to the structures. However, in the medium, the refractive index essentially varies from air/moth-eye coating to that of the bulk material, as shown in Figure 6. Reflection only occurs at abrupt changes in the refractive index; by removing this abrupt change, the moth-eye features cause an increase in transmission over a broader range of the spectrum.

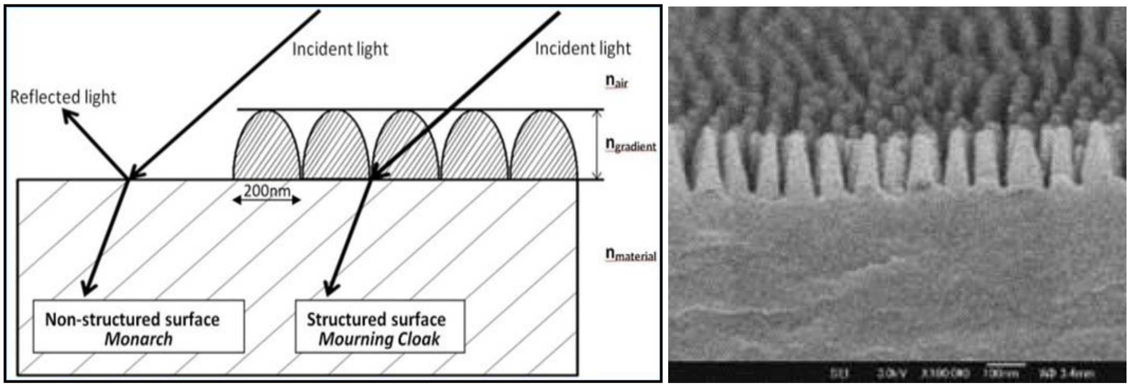

Figure 5: Depiction and scanning electron microscopy (SEM) image of a moth-eye array.[6]

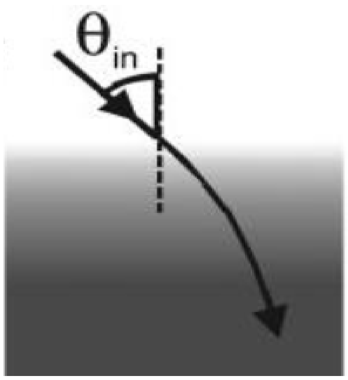

Figure 6: Gradient refractive index that changes gradually from air to substrate.[12]

2.3 Fabrication Limitations

To construct a moth-eye array – applicable to reducing reflections from a specific solar cell surface – there are multiple design and fabrication criteria that must be achieved. For a moth-eye array, the height and periodicity of each structure play a major role in obtaining optimal results. The theory derived and experimentally tested by Wilson et al[5] showed that the height of the protuberances had to be designed by considering the wavelength of incoming light. Modelling of the moth-eye structure was completed by both Wilson et al[5] and Aydin et al,[18] by representing this structure as a multi-layer film with a graded refractive index composed of several layers of equal thickness and progressively increasing refractive index. As shown in Figure 7, when h (the thickness of all the layers combined) $<<\lambda$, the reflectance is essentially that of a discontinuous boundary. As h/λ increases, a local minimum in reflectance is displayed at $h/\lambda = 0.4$. When considering an optical coating with a refractive index, n, the equation for the minimum height of a moth-eye structure is:

$$h = 0.4\lambda_L / n_1 \qquad (2.3.1)$$

where h is the height of the protuberance, λ_L is the longest operational wavelength, and n_1 is the refractive index of the material used for the moth-eye ARC. The longest operational wavelength is displayed on the solar intensity distribution. As the intensity of solar energy from the sun becomes relatively low at around 2000 nm in the infrared (shown in Figure 8), the goal is to develop a broadband anti-reflection coating for operation in the 400 – 2000 nm range.[19]

Therefore, this moth-eye ARC would be optimized for almost 95% of the solar spectrum.[5] The details of the curve shown in Figure 7 vary depending on the refractive index profile used in the modelling, but the main conclusions remain the same; if the thickness of the optical coating or structure height is on the order of half a wavelength or more, then the reflectance is considerably reduced.[5,6]

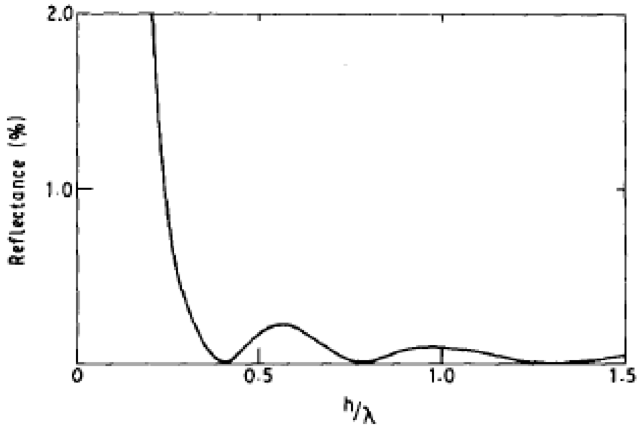

Figure 7: Optimal reflectance for a given ratio between the height of a moth-eye structure and the wavelength of incoming light.[5]

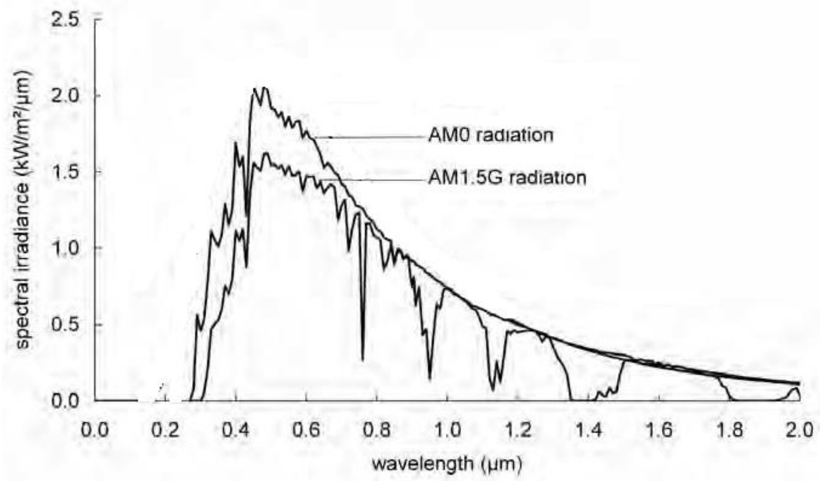

Figure 8: Irradiance vs. wavelength of the sun outside the atmosphere (AMO), and after entering the Earth's atmosphere (AM1.5G).[19]

An additional requirement that needs to be optimized, unlike in the planar ARC, is the periodicity of these moth-eye structures in order to form an array as shown in the SEM image in Figure 5. The periodicity of the array must be small enough with respect to the wavelength, so that the incident light cannot resolve the individual features; otherwise the array will act as a diffraction grating and simply redistribute the light into diffracted orders. The diffraction equation is represented by:[14,15]

$$d(\mathrm{Sin}\ \theta_i + \mathrm{Sin}\ \theta_m) = m\lambda \tag{2.3.2}$$

where d is the period of the grating, θ_i is the angle of incidence, θ_m is the diffracted angle maxima, m is the order of the diffracted maxima, and λ is the wavelength. Considering a normal angle of incidence, at the 1st diffracted maxima, at the largest diffracted angle possible (90º), one is able to show:

$$d[\sin(0) + \sin(90)] = \lambda$$
$$d = \lambda$$

Therefore, in order for the optical coating not to function as a diffraction grating, d must be less than λ so that the incident light cannot resolve the individual features. Thus, the first diffracted maxima angle would always be greater than 90º with respect to the normal of the substrate. The same theory applies for oblique incidence, except now the maximum angle of incidence is 90º (θ_i).

$$d[\sin(90) + \sin(90)] = \lambda$$
$$d = \lambda/2$$

Therefore d must be less than λ/2 so the incident light cannot resolve the individual features and a diffraction grating is not created.[5] When considering transmission where one must suppress orders diffracted inside the ARC itself, we require that the periodicity be less than half the smallest operational wavelength divided by the refractive index.[5] The smallest operational wavelength would correspond to the band gap of the optical coating being used as the ARC. This is because the optical coating no longer functions as a transparent film for photons having a wavelength corresponding to an energy larger than the band gap energy.

2.4 Patterning a Moth-Eye Array

Patterning of structures to achieve these types of dimensions has been conducted previously through the use of many different techniques including: interference lithography, the use of self-assembled silica beads, electron beam lithography, nano-imprinting, and dip pen nanolithography. In the sections to follow, these techniques will be described in an effort to show how a moth-eye array with structures of a known periodicity can be constructed in the nanoscale.

2.4.1 Interference Lithography

Interference lithography is a well-known technique for patterning structures with a periodicity as low as 75 nm using visible and UV lasers.[20] In order to create a moth-eye array, the periodicity must be approximately 100 nm, which can be achieved using this technique. First a layer of material used for the optical coating is deposited on the substrate, and then a layer of photoresist is spin coated on the coating. The next step is the interference lithography step where optical beams interfere to create an image on the surface of the photoresist. Gratings are used to create interference patterns by splitting and expanding multiple beams and having them interfere in a plane on the photoresist-covered substrate.[20–22] In order to create the desired pattern, the two optical beams generated using a laser(s) must have a certain wavelength so that structures with a desired periodicity are created. This can be expressed in the form of:[21]

$$\Lambda = \lambda/2\mathrm{Sin}\theta \qquad (2.4.1.1)$$

where λ is the wavelength of the optical beam, θ is the angle between the two interfering waves, and Λ is the periodicity of the pattern. Therefore one can calculate the lowest possible periodicity, which would be half of the wavelength of the optical beam. This means that in order to have a 100 nm periodicity, a UV laser with an optical wavelength of at most 200 nm must be used, such as the ArF laser (193 nm).

Figure 9 shows the interference lithography process for the formation of a ZnO moth-eye array.[22] An image is first formed on the positive photoresist through exposure, and then the photoresist is developed so as to remove it from the patterned areas. The patterned photoresist can be then reshaped at a specific temperature and duration of time. This is shown in Figure 9, step 4.[22] An etch is then performed in one of two ways; either a wet etch is performed in a solution that isotropically etches the thin film into the formed pattern, or reactive ion etching (RIE) is performed in a vacuum where plasma is formed and anisotropic etching occurs due to chemical reactions. The final step is photoresist removal, and the end product is a moth-eye array. This process is known as top-down fabrication.

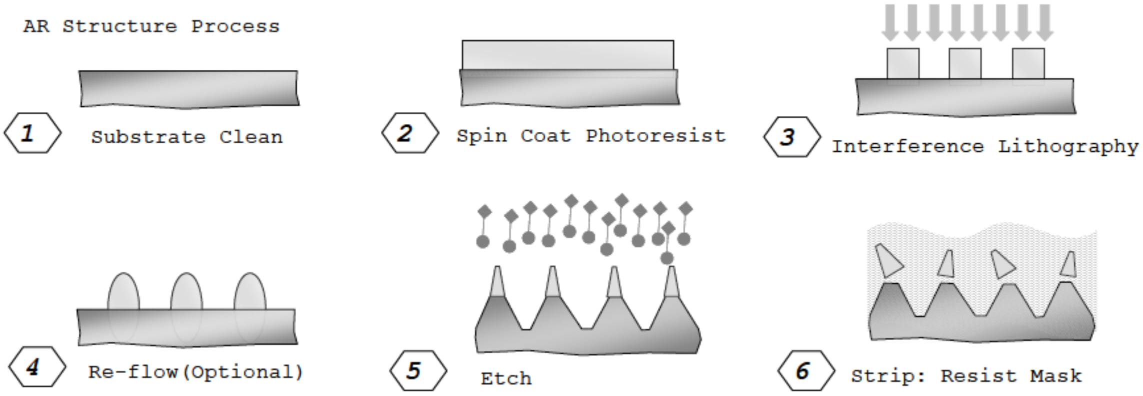

Figure 9: Interference lithography process for the formation of a ZnO moth-eye array.[22]

2.4.2 Patterning Using Self-Assembled Silica Bead Etch Masks

Another method of patterning the moth-eye array can be conducted using silica bead masks. A monolayer of silica colloidal crystals in a non-close-packed configuration is deposited on a substrate using a spin-coatable polymer supspension.[7] The polymer solution that forms these colloidal crystals was originally developed by Jiang et al.[23,24] Once spin coated, the polymer is etched away with oxygen plasma. The substrate (in this case silicon) is then reactive ion etched by SF_6 for a duration of nine minutes to form a nipple array .[7] The silica spheres on top of the substrate are then removed by an HF dip for two minutes. This method is depicted in Figure 10. Following this, an optical coating can be deposited on the patterned silicon to act as an effective moth-eye ARC.

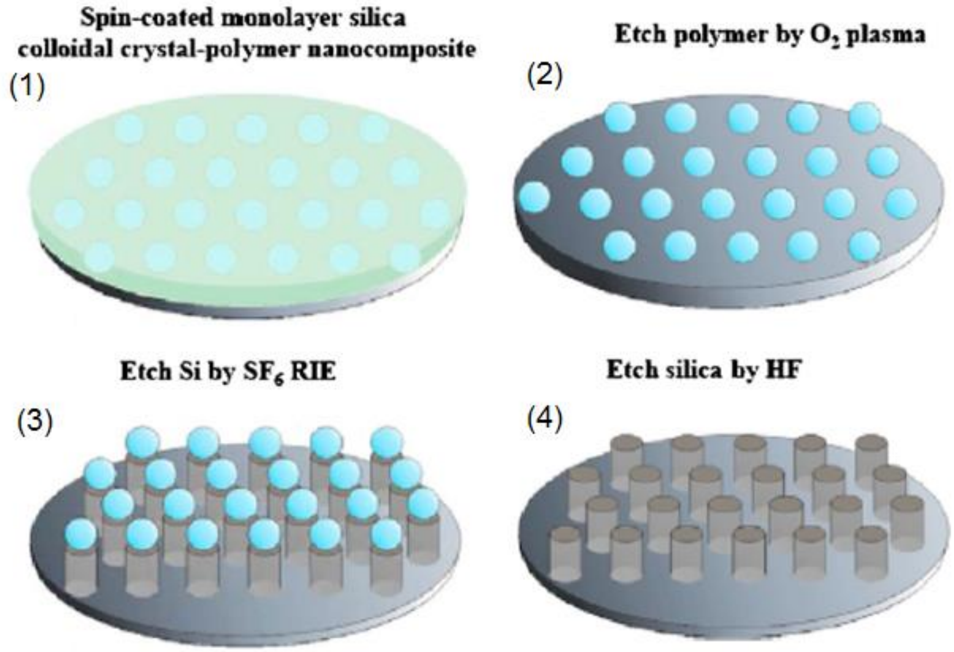

Figure 10: Fabrication of patterned moth-eye array using monolayer silica colloidal crystals with non-close-packed structures.[7]

2.4.3 Electron Beam Lithography

Electron beam lithography (EBL) is also used to form nanoscale structures with nanoscale periodicities. Photoresist is applied to the substrate, however unlike interference lithography, this method does not need a template or mask to create a pattern as it is a direct write method which is not limited by the optical diffraction limit. An electron beam is emitted and focused on the photoresist with the desired pattern dimensions, completing one patterned structure in the photoresist at a time. Thus, patterning larger areas takes a long period of time. After the patterning of the photoresist is complete, etching is completed using the same method as in Section 2.4.1. This process is depicted in Figure 11.

Kanamori et al completed transmission measurements on a moth-eye array that was created from PMMA using this technique.[25] Once the pattern was etched into the substrate, PMMA was then spin coated into the patterned structure as shown in Figure 11, step d. EBL created a pattern with a periodicity of 200 nm, and through the process of different etch parameters in the RIE system, the heights varied. The PMMA pattern underwent a lift off process and was bonded to glass for optical characterization. Therefore, Kanamori et al developed a technique to pattern a moth-eye array with a 200 nm periodicity and a height of these structures varying from 50 to 250 nm.[25]

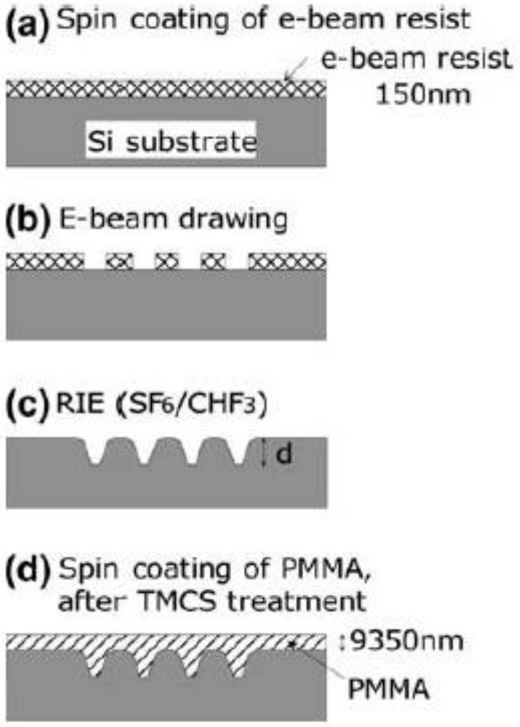

Figure 11: Patterning a moth-eye array with EBL.[25]

2.4.4 Nano-imprinting

Another example of patterning is the nano-imprinting technique. This technique is a modified version of interference lithography and EBL. For nano-imprinting, the moth-eye structures are patterned on a master (nickel substrate) using either EBL or interference lithography to create the proper periodicity. This master mould is then used to create a flexible master (various materials used) which is rolled over a layer of photoresist as shown in Figure 12. This process is a roll-to-roll method which then uses ultraviolet light to cure the photoresist.[11] This photoresist layer now acts as an etch mask which can be used in the etching processes described in section 2.4.1.

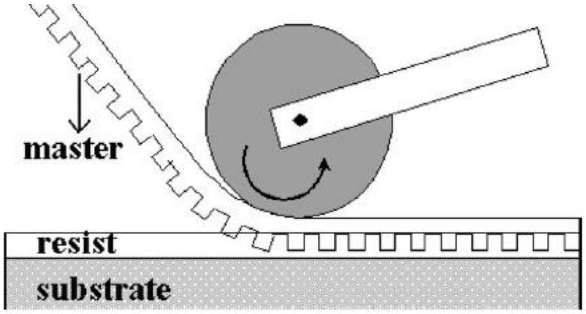

Figure 12: Roller nano-imprint method.[11]

Moth-eye arrays were developed using this method by Chen et al.[11] Structures were nano-imprinted with a periodicity of approximately 200 nm, which are shown in Figure 13. By adjusting the dry etch parameters, they were able to develop a structure with heights varying from 100 to 700 nm.[11] This moth-eye array was created on a silicon substrate and shows that nano-imprinting is a quick and easy method to pattern these structures without individually exposing each substrate to a laser interference or electron beam. It also establishes the ability to pattern large areas with minimal time and lower cost compared to the previous patterning techniques.

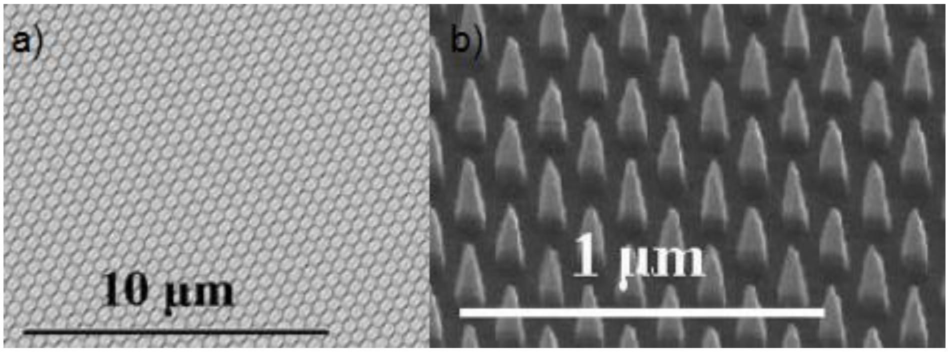

Figure 13: Nano-imprinted structures a) topographical view b) zoomed in view at a tilted angle.[11]

In each of the aforementioned methods of fabricating a nanoscale structured array, some type of patterning step was always completed. Thus far, patterning samples was the only way to accurately develop structures with nanoscale dimensions. Each of these methods has a drawback however. In interference lithography, the pattern's periodicity is limited by optical diffraction. Though EBL does not have this limitation, it is in turn costly (>$150/h) and time consuming (>5 hours for 5mmx5mm areas with nanoscale dimensions), particularly at this small nanoscale periodicity. Though silica-template and nano-imprinting are the preferred techniques, they are still costly as RIE is an expensive and sophisticated piece of equipment. The overall drawback to patterning is thus the cost required to pattern in these dimensions, and this is a problem that limits mass production. These techniques do prove to be useful however, as they allow for accurate patterning in the nanoscale. Though there are many other methods being researched today, the goal in this research is to fabricate a self-assembled moth-eye array that effectively eliminates the patterning cost from the manufacturing budget.

2.5 ARC Requirements

In order to design a suitable anti-reflection coating with an appropriate refractive index and thickness profile for photovoltaic cells, the type of substrate, the operating wavelength range, and the range of angle of incidence must all be considered. While working in collaboration with a concentrating photovoltaics company, the end goal of this research was to deposit moth-eye anti-reflection coatings on their III-V semiconductor solar cells. Their solar cells consist of a multilayer stack of InGaP, GaAs and Ge on a Ge wafer with a top layer that has a refractive index of approximately 4. In order to develop a versatile method for inexpensive, rapid (in the order of minutes), and low temperature (<100ºC) deposition of moth-eye anti-reflection coatings directly on semiconductor substrates, we began our experiments on widely available semiconductor substrates. Our vision was to develop a versatile method that could be easily transferred to any semiconducting substrate of similar doping and conductivity. For this purpose, we initiated our developmental work on widely available and low-cost substrates including Indium tin oxide (ITO) and silicon. The material chosen for the ARC was ZnO because of its large band gap of approximately 3.3

eV, its affordability, its refractive index, and most of all because it is transparent in most of the visible and infrared range. This material will be placed between a substrate with a refractive index of approximately 4, and air with a refractive index of 1, so ZnO having a refractive index of approximately 2 makes it ideal as an anti-reflection coating.

Once the material and substrate were chosen, the next major limitation to address was the process used to create the moth-eye anti-reflection coating. Many methods have been previously used to deposit ZnO such as chemical vapor deposition (CVD)[26], physical vapor deposition (PVD)[27], pulsed laser deposition (PLD)[28], spray-on techniques[29], and electrochemical techniques.[30–35] However, CVD, PVD, and PLD are expensive techniques requiring a long deposition time, and spray on techniques lack the proper control to deposit a uniform layer. This is the reason electrodeposition was chosen as the depositing process; it offers control of the deposited thin film on the nanoscale at low temperatures. It is also rapid, affordable, and controllable for direction deposition of structures with tunable morphology so post-patterning is not needed in the overall manufacturing process.

Chapter 3: Zinc Oxide Electrodeposition

3.1 Zinc Oxide

ZnO has been used in electronics, acoustics, sensing, piezoelectric transducers, and photovoltaics. In photovoltaics, ZnO has been used as an anti-reflection coating, as an initial window layer, which is a highly conductive flat material on which light-generated electrons can travel laterally to the electrical contact, and as the as core semiconductor for solar cell technology. ZnO has multiple material characteristics that make it desirable for use in photovoltaic systems. It has a wide band gap of approximately 3.3 eV at room temperature, allowing a large fraction of the solar spectrum to transmit through the ZnO layer. This is possible because it absorbs light at its band gap energy, which corresponds to a wavelength of approximately 380 nm. This means that it absorbs the photons' energy only in the ultraviolet (UV) range, therefore transmitting the visible and infrared photons right through to the substrate to be absorbed. Another advantage of ZnO is its refractive index of approximately 1.98. In most silicon substrates in use in industry today, the refractive index is approximately 3.85, so by using the optimal refractive index for an ARC equation (2.1.4) with air as the other boundary, an optimal ARC would have a refractive index of 1.97. This value almost matches that of ZnO. If using a III-V semiconductor or a substrate such as InGaP or GaAs as the next layer – which have refractive indices of approximately 4 – ZnO could be an optimal ARC for these materials as well. Therefore, study of electrodepositing ZnO should be completed to see if it can operate as an ARC.

3.2 Electrodeposition Theory

Electrodeposition is the deposition of a substance on an electrode by the action of electricity. A current or voltage is applied to a system and the reduction of ions from an aqueous solution at the surface of the electrode forms structures that are integrated into the substrate lattice. The definition of reduction is ions gaining charge:

$$M^{z+} + ze \rightarrow M$$

This is the reaction of charged particles at the interface between an electrode and a liquid solution. Once they have gained their charge, they are able to cross this interface; they diffuse into the substrate or onto another deposited particle. There are three factors that affect electrodeposition: the metal-solution interface, mass transport, and nucleation and growth.[36]

At the metal-solution interface, there is the creation of an electrical double layer. In solution, two planes are defined to describe the double layer: the inner Helmholtz plane (IHP) and the outer Helmholtz plane (OHP). The region between the IHP (closest to metal) and the metal electrode, consists of solvent molecules and specifically absorbed species.[37] At the OHP, solvated cations or anions (depending on the applied potential) are attracted to the metal by electrostatic forces only. These ions build up charge from the OHP and outward, and this is called the diffuse layer because non-specifically absorbed species are contained in this three dimensional space. This is displayed in Figure 14.

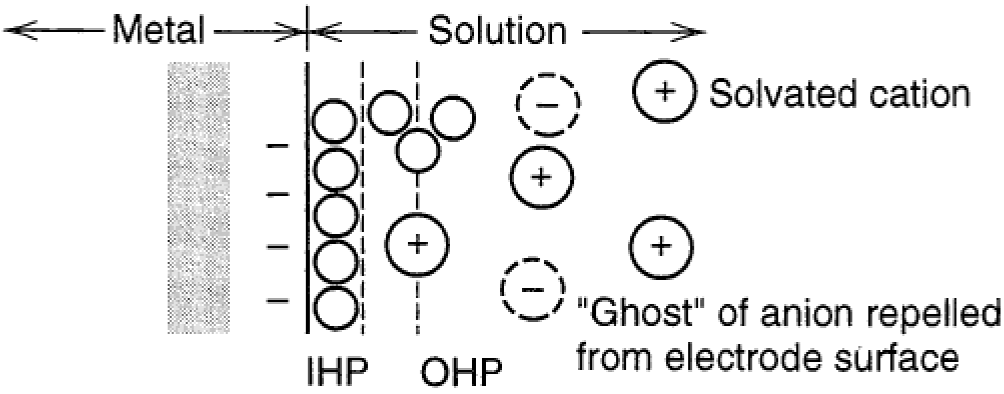

Figure 14: The IHP and the OHP and the interaction of ions at the interface.[37]

In electrodeposition, when a potential is applied to the solution, this electrical double layer acts like a capacitor and the buildup of charge yields a charging current. The concentration of ions in the solution controls the solution resistance, which in turn affects this charging current. An ideal polarizable electrode with an applied potential is represented in the following circuit:

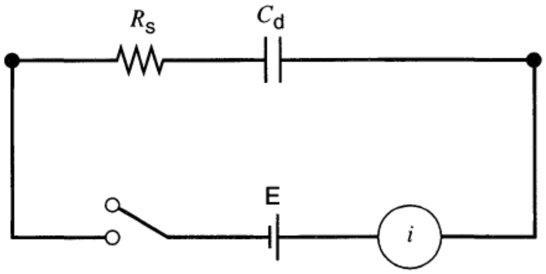

Figure 15: RC circuit representing an ideal polarized electrode.[37]

Therefore the current can be calculated like in a normal RC circuit, by the following equation, which describes the relationship between the charging current and the capacitor:[37]

$$i = (E/R_s)e^{[-t/(R_s C_d)]} \qquad (3.2.1)$$

where E is the applied potential, R_s is the solution resistance, t is time, and C_d is the capacitance of the double layer. This decay in current represents the initial charging of the electrical double layer before the faradaic current can be displayed in the electrodeposition of a material. Equation (3.2.1) originates from the equation for charge of the capacitor: [37]

$$q = q_{max}[1-e^{-t/(R_s C_d)}] \qquad (3.2.2)$$

where $q_{max} = C_dE$ (the capacitance of the double layer and the applied potential), t in the time, R_s is the resistance of solution, and C_d is the capacitance of the double layer. By rearranging the charge equation we can solve for the time it takes to fully charge the capacitor.

$$q/ q_{max} = [1-e^{-t/(R_s C_d)}]$$

where q/ q_{max} is the percentage of how much the double layer is charged. Therefore at t = 0, q must be zero, the voltage of the capacitor is zero, and the current is $I=E/R_s$. However, as $t \rightarrow \infty$, $q \rightarrow q_{max}$ (fully charged), voltage at the capacitor approached the applied potential and the current decays to a minimum as shown in equation 3.2.1. Therefore with the resistance of the solution and the capacitance of the double layer we are able to solve for the time it takes for the current to decay to a local minimum on an electrodeposited current transient.

The effect of mass transport in electrodeposition is the movement of all ions and solvents from one location in solution to another, and the movement of these species has a direct effect on the overall reaction rates. Mass transport in electrodeposition is completed in three ways: diffusion, migration, and convection. Diffusion is the movement of particles in solution from high to low concentration.[37] This concentration gradient is the driving force for the molecules in the solution. Migration is a process through which an external field, capable of exerting an electrostatic force on a charged species, can thereby induce movement of ions on the electrode surface. Lastly, convection is a process through which mechanical forces act on a solution and cause movement. Convection can be caused by natural forces exerted by density or temperature gradients in solution or by external forces applied using stirring, pumping, or bubbling. Mass transport can be described (in one dimension only) by the Nerst-Planck equation as:[37]

$$J_i(x) = -D_i \frac{dC_i(x)}{dx} - z_i F\, D_i C_i \frac{d\phi(x)}{dx} + C_i v(x) \tag{3.2.3}$$

where $J_i(x)$ is the flux of species i (mol $s^{-1}cm^{-2}$) at distance x from the surface, D_i is the diffusion coefficient (cm^2/s), $dC_i(x)/dx$ (mol/cm^4) is the concentration gradient at distance x, $d\phi(x)/dx$ is the potential gradient, z_i and C_i are the charge (dimensionless) of the species i and concentration (mol cm^{-3}) of species i respectively, and v(x) is the velocity (cm/s) with which a volume element in solution moves along the axis.[37] The three parts of the equation correspond to diffusion, migration, and convection respectively.

Nucleation and growth is affected by the rate of electrode reactions in solution. The four main factors affecting the electrode reaction rate are:[37]

1) mass transfer,
2) electron transfer at the electrode surface,
3) chemical reactions in solution or on the electrode surface before or after electron transfer, and
4) other surface reactions such as crystallization.

Mass and electron transfer have already been discussed above. Chemical reactions (3) can occur in solution or on the electrode surface, and this can slow down or speed up the overall rate of reaction. An example of this is the formation of ZnO at lower temperatures; a layer of zinc hydroxide is first formed on the electrode surface, which then dehydrates and forms a ZnO seed layer. The last factor, other surface reactions (4) can be attributed primarily to crystallization, which is the formation or build-up of a material. Instead of creating new nuclei, material builds up off of existing deposited material.[36] This process is affected by the population of adatoms and the overpotential.[36] Assuming the deposition solution and substrate stay constant, the overpotential becomes the main component in structural formation. Nucleation occurs because the potential has been shifted negatively from the equilibrium potential of the ions and the material. This is why it is called the overpotential and is defined as:[38,39]

$$| U_n - U_{eq} | \tag{3.2.4}$$

where U_n is the overpotential and U_{eq} is the equilibrium potential in solution with the electrode surface present. Therefore, depending on the magnitude of the nucleation overpotential, there can be three regimes where the overall electrodeposition is controlled by: 1) surface kinetics, 2) a combination of kinetics and diffusion, and 3) the diffusion of ions to the electrode surface. In case 1) where the nucleation overpotential is close to U_{eq}, the reaction is kinetically controlled, causing slow growth after initial nucleation which is also relatively sparse. This is the kinetically-controlled regime and growth occurs in two ways: either adatoms attach directly to the islands formed, or the adatoms form indirectly on the substrate through absorption followed by surface diffusion.[40] This displays both vertical and lateral growth respectively. In case 2) where there is moderate increase in nucleation overpotential, the potential increases farther away from equilibrium, which in turn causes a high flux of ions on the growing islands. This prevents faceted structures from growing, but hemispherical structures can grow because of radial transport.[40] This deposition is both kinetic and diffusion-controlled. Lastly in case 3), large nucleation overpotential causes island growth right after nucleation, at very high rates. This deposition is in the diffusion regime, and growth instabilities cause the deposition of material at the most preferred spot in that region.[40] This causes the formation of unlikely structures such as dense branching or dendrites.[40] All three of these deposition regimes are displayed in Figure 16.

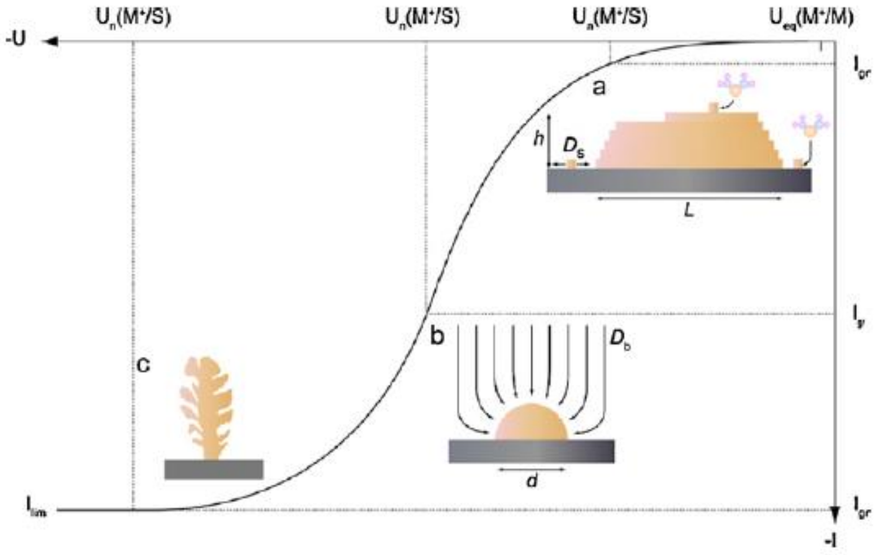

Figure 16: a) small nucleation overpotential in the kinetic regime, b) moderate nucleation potential in the kinetic and diffusion regime, c) large nucleation overpotential in the diffusion regime.[40]

The rate of nucleation is also important when trying to electrodeposit materials. The rate of nucleation is affected by the overpotential, the solution composition, and the surface free energy of the substrate. All three of these relationships can be described by the nucleation rate:[41]

$$N(t) = N_\infty[1- \exp(-AN_\infty t)] \qquad (3.2.5)$$

where N is the number of nuclei per surface area, t is time, and A is the steady state nucleation constant per site which is a function of overpotential, solution composition, and substrate surface free energy.[41] By keeping time constant and modifying different parameters of A, one is able to increase initial nucleation. As A increases, this causes the differential of 1 to approach zero and N to approach

N_∞, which is the maximum number of nuclei per surface area obtainable under those conditions.

3.3 ZnO Electrodeposition-Pertinent Literature

ZnO electrodeposition has been researched widely over the last decade as it is a cost effective way of depositing thin films, applicable to several industrial applications. ZnO electrodeposition is conducted with two main ions in solution; zinc (Zn^{2+}) ions and hydroxide (OH^-) ions. Zinc oxide electrodeposition can be described via the following chemical reactions:[31]

$$Zn^{2+} + 2OH^- \rightleftharpoons Zn(OH)_2 \tag{3.3.1}$$

$$Zn(OH)_2 \rightarrow ZnO + H_2O \tag{3.3.2}$$

Initially, the zinc ions react with the hydroxide ions to form zinc hydroxide at the electrode surface, which then spontaneously dehydrates to form ZnO.[31] However, in order to have these ions in solution, a zinc salt precursor and an oxygen precursor must be present. There are different zinc and oxygen precursors used in ZnO electrodeposition, and adjusting these precursors and their concentrations in solution can have drastic effects over the deposition rate and structures formed.[30,32,33,42] Deposition parameters such as overpotential have also been the main focus of research in the last decade. The ability to control the nucleation rate and develop ZnO structures with set dimensions that are reproducible, are just some of the developments still being optimized today. The following sections describe different approaches for electrodepositing ZnO.

3.3.1 Hydrogen Peroxide as an Oxygen Precursor

ZnO electrodeposition always requires some type of oxygen precursor. The most commonly used precursor has been the inclusion of oxygen into the electrodeposition solution via bubbling. This technique allows for a limited concentration of oxygen (10^{-3}M) to be available for electrodeposition due to the low (14.6mg/L at 0ºC and 7.6mg/L at 20ºC, so temperature dependant) solubility of oxygen in a hot water bath, which hinders growth.[43] Pauporte et al demonstrated that the reduction of hydrogen peroxide can be used for generating the hydroxide ions required for ZnO electrodeposition, and that hydrogen peroxide is highly soluble in water. The following series of reactions describe the electrodeposition of ZnO in a bath containing hydrogen peroxide:[30]

$$H_2O_2 + 2e^- \rightarrow 2OH^- \text{ (cathodic reaction)} \qquad (3.3.1.1)$$

$$Zn^{2+} + 2OH^- \rightleftharpoons Zn(OH)_2 \qquad (3.3.1.2)$$

$$Zn(OH)_2 \rightarrow ZnO + H_2O \qquad (3.3.1.3)$$

The ability to adjust the amount of H_2O_2 and study its effects offers another form of control in the deposition. Pauporte et al used hydrogen peroxide as the oxygen precursor and zinc perchlorate as the zinc salt, with the addition of $LiClO_4$ to fix the perchlorate concentration so the solution was at the desired pH (5.5-6.5).[30] Furthermore, it was demonstrated that the optical properties of the film changed with the addition of hydrogen peroxide. This is depicted in Figure 17. The four following films were deposited: a) containing 2.5 mM of H_2O_2 deposited for 3600s which created a thickness of 0.63 µm, b) containing 5 mM of H_2O_2

deposited for 1800s which created a thickness of 0.6 µm c) containing 25 mM of H_2O_2 deposited for 514s which created a thickness of 0.9 µm, and d) containing 40 mM of H_2O_2 deposited for 300s which created a thickness of 0.93 um.[30] The conclusions were that increasing the concentration also increased the deposition rate, and the higher the concentration of H_2O_2, the more transmission occurred over the whole spectrum.[30] Pauporte et al concluded that this was a result of the change in morphology of the thin films; from sharp-edged structures at low concentrations (5mM) of H_2O_2, to smooth thin film-like features at 40mM concentrations. Overall, the effect of H_2O_2 has many advantages when used as an oxygen precursor for ZnO electrodeposition.

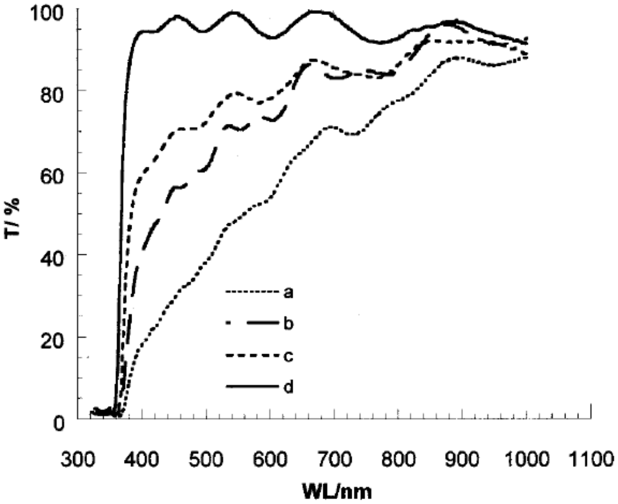

Figure 17: Optical transmission of ZnO films deposited at different hydrogen peroxide concentrations: a) 2.5mM, b) 5mM, c) 25mM, d) 40mM[30]

3.3.2 The Effect of Temperature

As discussed by Giroux et al, temperature directly affects the type of material deposited and the rate at which electrodeposition occurs. In this work, the electrodeposition solution contained $ZnCl_2$ salt and oxygen supplied through the bubbling of O_2. The depositions were conducted at a slow rate (due to dissolving oxygen), although there was an increase in rate as the temperatures rose. SEM images of the structures grown on tin oxide are shown in Figure 18. As temperature increases, the structures slowly change from small, faceted structures to a smooth, thin film layer.

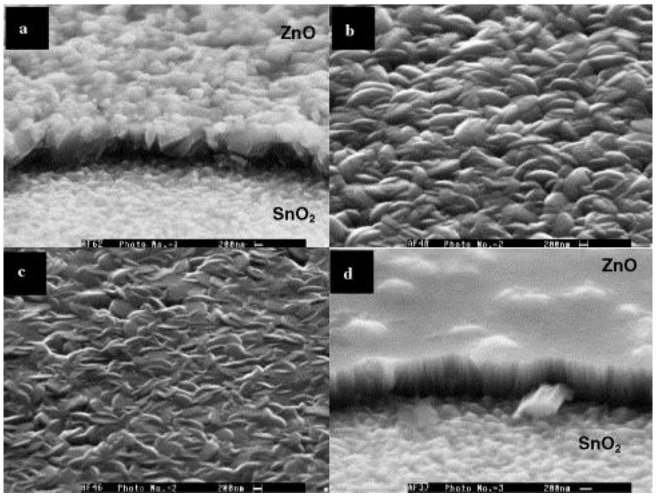

Figure 18: Electrodeposition of ZnO films deposited at a) 34ºC, b) 40ºC, c) 50ºC, d) 80ºC.[31]

Giroux et al observed that at temperatures below 34ºC, a layer of zinc hydroxide forms.[31] At 34ºC a slow dehydration reaction of this layer occurs, creating a ZnO seed layer for nucleation. Above 34ºC the process for growing ZnO includes deposition of a zinc hydroxide layer, dehydration of the zinc hydroxide layer, creation of a seed layer, and growth. This is depicted in Figure 19. First a gel layer of zinc hydroxide is formed, effectively passivating the surface. At higher temperatures this layer instantly dehydrates into ZnO seeds, a few seconds after potential application.[31] After these seed layers are formed, ZnO growth occurs.

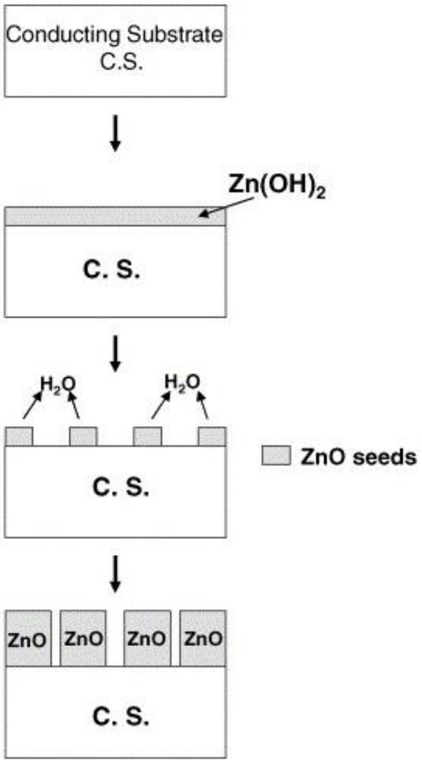

Figure 19: The process for electrodeposition of ZnO at a temperature above 34ºC.[31]

3.3.3 Zinc Salts

ZnO thin films are also deposited using different salts, of which $Zn(NO_3)_2$ and $ZnCl_2$ are most the commonly used. In literature[33,35,42,44] the $Zn(NO_3)_2$ salt was used both as the zinc and oxygen precursor. The nitrate reaction was:

$$NO_3^- + H_2O + 2e \rightarrow NO_2^- + 2OH^- \qquad (3.3.3.1)$$

Once this reaction was completed, then reactions (3.3.1) and (3.3.2) followed, reacting with the zinc and hydroxide ions. The formation of ZnO from this salt in a water bath with no other reagents is shown in Figure 20. This deposition occurred with a potential of -1.1V at 89ºC.

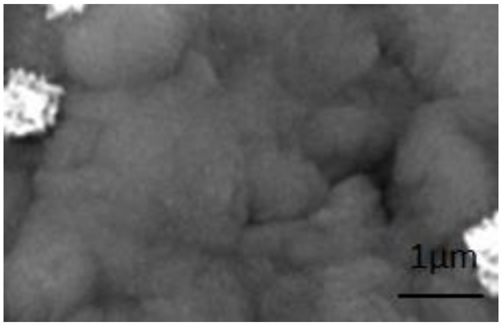

Figure 20: Electrodeposition of ZnO in a solution of 0.1M $Zn(NO_3)_2$ with a potential of -1.1V at 89ºC.[42]

Research from Mahalingam et al demonstrated the relationship between the ZnO deposition rate and the concentration of $Zn(NO_3)_2$, as well as the applied potential.[33] This is depicted in Figure 21. As both graphs demonstrate, there is an increase in rate with an increase in both potential and concentration; however, there is also a local maximum in both. After reaching a certain overpotential and concentration, the deposition rate decreases. This overpotential window (-0.8V to -1.2V) in which electrodeposition can occur at high rates, has been found through the use of CV measurements to be the optimal potential for the formation of ZnO structures. With regards to concentration (>0.15M), the reaction of nitrate reduction produces nitrite and ammonia, which progressively accumulates in the deposition bath and leads to deposition instabilities at high concentrations.[33,43]

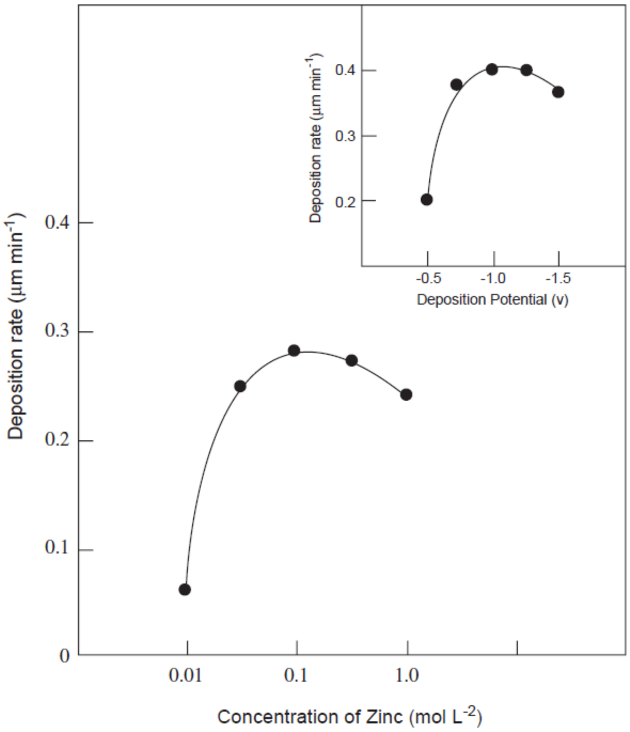

Figure 21: The varying of the deposition rate with respect to both concentration and potential when using a $Zn(NO_3)_2$ solution[33]

In literature[32,34,45,46] the $ZnCl_2$ salt is also used for zinc oxide deposition along with an additional oxygen precursor such as dissolved oxygen through bubbling. However, at high concentrations of $ZnCl_2$, other materials such as zinc oxychloride are deposited due to the formation of complex zinc ions such as $ZnCl^+$ or $ZnCl_2^-$, instead of Zn+.[46] The formation of these complex ions is not well-studied in literature, and further analysis should be completed on $ZnCl_2$ solutions containing different concentrations.

3.3.4 Addition of an Electrolyte

The addition of an electrolyte is usually for the purpose of adding conductivity to a solution, or to affect the overall pH of the solution. Research has been conducted to study the effects of adding Cl^- ions to a solution through the addition of potassium chloride (KCl) or sodium chloride (NaCl) on the structure of ZnO.[44,47] The results of this study are shown in Figure 22 and 23. In Figure 22, Liu et al used NaCl with $Zn(NO_3)_2$ salt in an electrodeposition solution. As the concentration of NaCl increased, the size of the resulting deposited structures increased, and the particles became more faceted.[44] In Figure 23, Tena-Zaera et al used $ZnCl_2$ salt with varying concentrations of KCl in an electrodeposition solution. With an increase in KCl concentration, the nanowires grew in size (both in height and diameter) and became more perpendicular to the surface. The increase in chloride concentration proves to increase deposition rate, creating both wider and taller structures. This is attributed to the increase in reactant concentrations caused by the “salt effect”.[44]

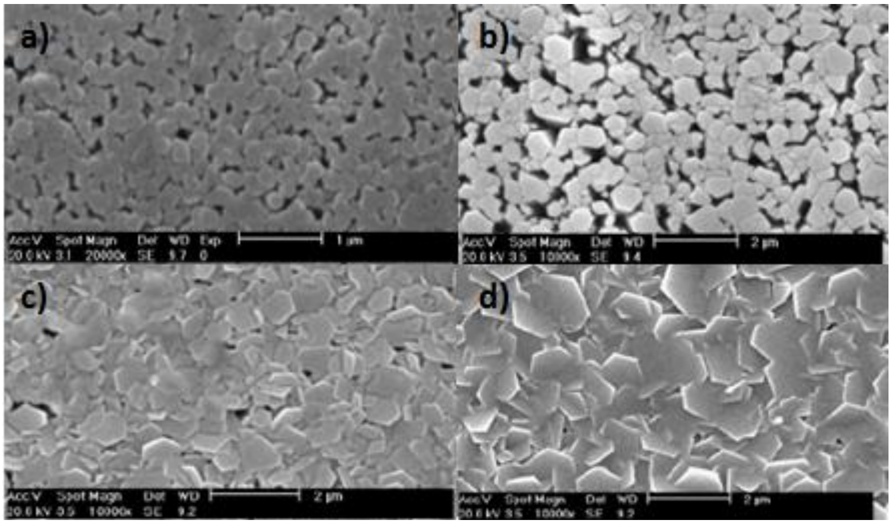

Figure 22: ZnO electrodeposition in a solution of $Zn(NO_3)_2$ with varying NaCl: a) 0M, b) 0.01M, c) 0.05M, d) 0.1M (Topographical View).[44]

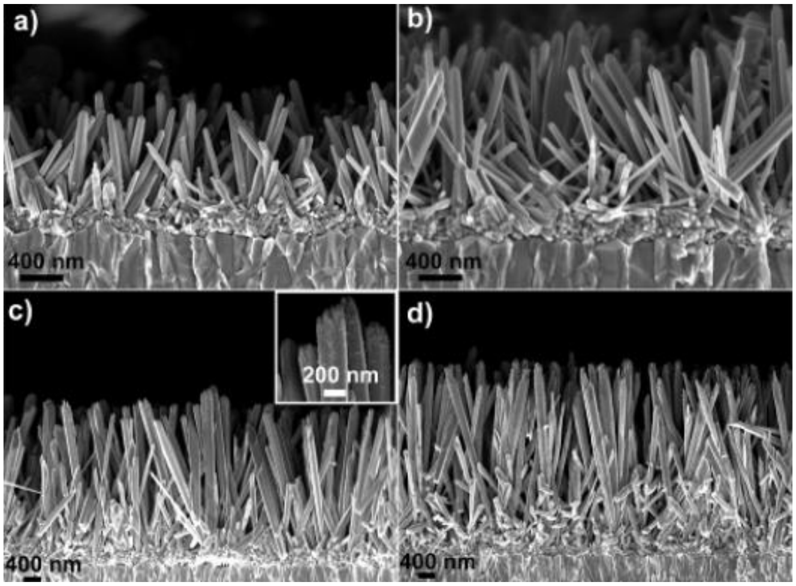

Figure 23: ZnO electrodeposition in a solution of $ZnCl_2$ with varying KCl: a) 0.05M, b) 1M, c) 2M, d) 3.4M (Tilted View).[44]

Optimization of the electrodeposited ZnO structures for the purpose of making ZnO nipple arrays for moth-eye anti-reflection coatings has not been completed to date. In this research, the ability to control the periodicity of the ZnO structures, aspect ratio and the nucleation rate will be the main focus. The overall goal is to create a self-assembled electrodeposited ZnO moth-eye array. If this can be achieved at the nanoscale, then effective patterning methods can be omitted in subsequent steps. The control and tunability of the depositions in this research can then be implemented in other ZnO photovoltaic applications. The following chapter will discuss the procedures involved in the electrodeposition of ZnO and will explain the experimental apparatus used for creating these ZnO nanostructures.

Chapter 4: Zinc Oxide Thin Film Electrodeposition Technique

4.1 Structure Geometry – Design Considerations

Prior to the fabrication of the ZnO coatings, the requirements for a moth-eye anti-reflection coating had to be calculated for a ZnO material. The first requirement was the height (h) of the protuberances:

$$h = 0.4\lambda_L / n_a \tag{4.1.1}$$

where the longest operational wavelength (λ_L) was estimated to be 2000 nm, and the refractive index of ZnO (n_a) was 1.98. As the intensity of solar energy from the sun becomes relatively low at around 2000 nm in the infrared, the goal was to develop a broadband anti-reflection coating operational up to this wavelength. Therefore, the heights of these ZnO moth-eye structures were calculated to be approximately 400 nm. The second requirement was the periodicity of these ZnO moth-eye arrays, $d < \lambda_m / 2n_a$, where the smallest wavelength (λ_m) is equal to the band gap of ZnO (~380 nm), and the refractive index (n_a) is 1.98. The smallest operational wavelength would correspond to the band gap of the ZnO because ZnO no longer functions as a transparent film in wavelengths below this value, as it absorbs photons. Therefore, the periodicity of these ZnO moth-eye structures was calculated to be approximately 100 nm. This indicates that a 4:1 aspect ratio is required in order to fabricate the most optimal ZnO moth-eye ARC, which is displayed in Figure 24.

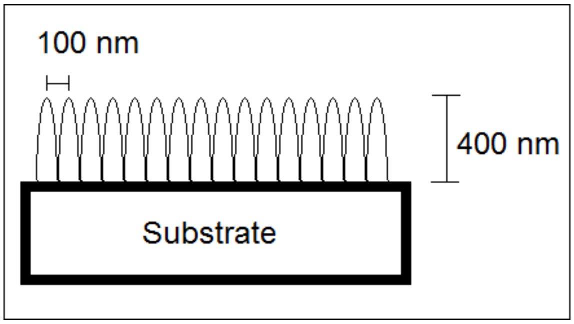

Figure 24: An optimal ZnO moth-eye anti-reflection coating with a 4:1 aspect ratio.

For the preliminary stages of this research, experimentation began with the selection of a substrate that was easy to prepare, conductive, and transparent. Due to their high cost and the presence of native oxides, neither silicon nor III-V semiconductors were chosen for the preliminary experiments. ITO was the first substrate used for optimizing the deposition of ZnO moth-eye structures as it is easily and inexpensively fabricated at our cleanroom facilities, while being a transparent conducting substrate suitable for electrodeposition purposes and optical measurements. ITO was fabricated using the sputtering technique described in the following section.

4.2 Deposition Techniques

4.2.1 Sputtering

The sputtering technique is a physical vapor deposition method for depositing materials on a substrate. It involves the ejecting of a material (ITO) from a target onto a substrate. First, an inert gas (argon) is flowed into the system and a voltage is applied, causing the argon to form a plasma; ions from the plasma then bombard the target material at the cathode. The higher the pressure of the inert gas, the lower the energy of the bombarding ions from the plasma, so energy of the ions can be controlled. In order for the Indium, tin, and oxygen atoms to be ejected from the target and form on the substrate (anode), they are bombarded by ions formed from the argon plasma. Sputtering is therefore a collision process where atoms and ions exchange momentum.[48,49] Once the atoms have an energy greater than that of the surface binding energy of the target, they are ejected and deposited on the substrate or chamber walls.[48,49] In RF sputtering, an oscillating voltage is applied at a radio frequency of about 13.5MHz. On the positive cycle, electrons are attracted to the cathode creating a negative bias; on the negative cycle, ion bombardment occurs.[50] Since there is no constant voltage on the cathode, this helps prevent ion build-up on the target.[51] Plasmas formed from RF tend to fill the whole chamber, as opposed to DC which is confined to the cathode. This system can be seen in Figure 25.

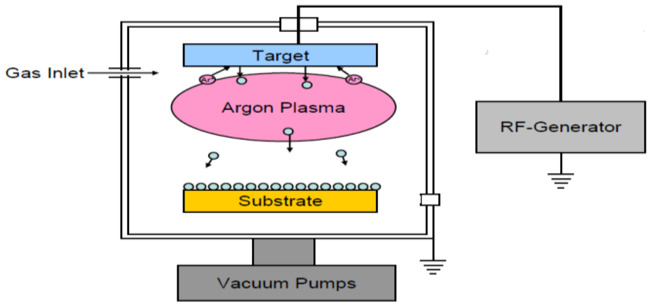

Figure 25: Chamber used for RF sputtering materials on a substrate.

4.2.2 Electrochemical Methods for Thin Film Deposition

4.2.2.1 Electrochemical Cell

Next, the experimental apparatus was built. In the electrochemical cell there were three electrodes. The first electrode was the working electrode, which is the conductive substrate that is being deposited on. Electrochemical reactions occur at the interface between the working electrode and the solution. These reactions (described in Section 3.3) cause the deposition of ions from the solution to the electrode. The second electrode in the cell is the reference electrode, which has a stable and well-known electrode potential. The high stability of the electrode potential is reached by employing a redox system with constant concentrations of each participant of the redox reaction.[37] Typically, the reference electrode includes a saturated solution of an insoluble salt, which in these experiments is a silver-silver chloride electrode. Figure 26 depicts the reference electrode used in the following experiments, which is comprised of a silver wire inserted in a saturated KCl solution. The silver wire is coated with AgCl from the ionic reaction between the silver wire and chloride ions.[52]

$$AgCl_{(s)} + e^- \rightleftharpoons Ag_{(s)} + Cl^- \qquad (4.2.2.1.1)$$

The constant and stable potential of this system allows the potential of the working electrode to be determined with respect to the Ag/AgCl (0.197 V vs. SHE) reference electrode. The reference electrode can be used to simultaneously apply the potential and to measure the current; however if this electrode carries current, its constant voltage will be affected and can no longer act as a robust reference electrode.[37] This is why a three electrode system is used, which is depicted in Figure 27. The third electrode – a platinum wire, is the counter electrode which is used to complete the circuit with the working electrode, and carry current which can then be recorded for electrochemical analysis.

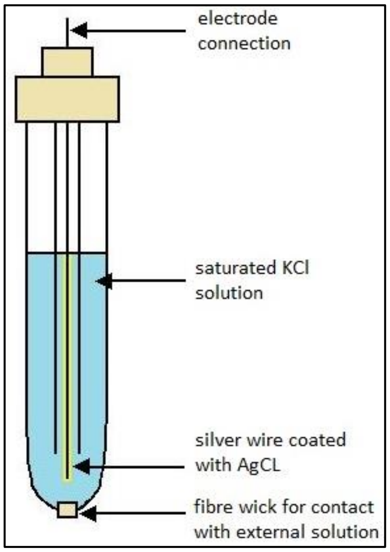

Figure 26: Silver-silver chloride reference electrode.

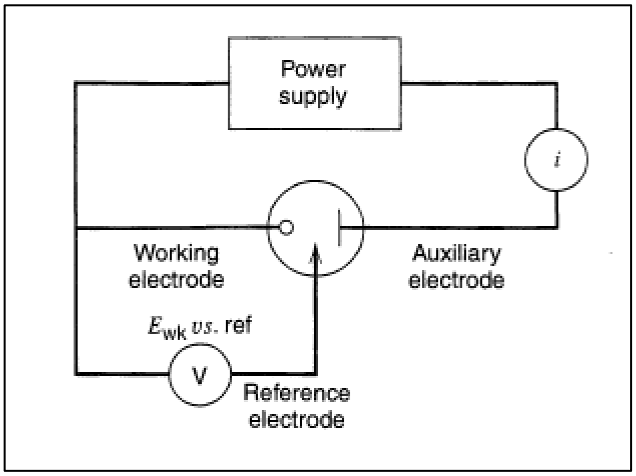

Figure 27: Three electrode electrochemical cell in a solution.[37]

4.2.2.2 The Potentiostat

These experiments were conducted with the use of a potentiostat which is a device used for enforcing a controlled potential at an electrode.[37] It is made up of a function generator to produce the desired perturbation, and a recording and display system for measuring and presenting current, potential, and time.[37] A basic electrical schematic is shown in Figure 28. A potentiostat controls the potential across the cell by sensing changes in the resistance, and accordingly varying the current applied to the system to keep the voltage constant. Its operation is in the form of a control amplifier which in theory comes with two main assumptions. The first assumption is that the op amp is being operated in linear mode (not saturated) so the voltage difference between the two inputs is negligible. The second assumption is that the input pin impedances are very high, causing the initial voltage to appear at both input pins. Therefore, the control amplifier's job in a potentiostat is to amplify the potential difference between the two inputs. This causes a lower impedance at the output so the reference electrode is always at $-e_i$ (potential) vs. ground, and the working electrode is grounded, e_{wk}(vs. ref) = e_i, regardless of the impedances caused by the solution.[37] In these experiments, a CH instrument (660 Model) potentiostat was used. The potential control range of the device is ±10 V, the current range is ± 250 mA, and it is capable of measuring current in the picoamperes.[53]

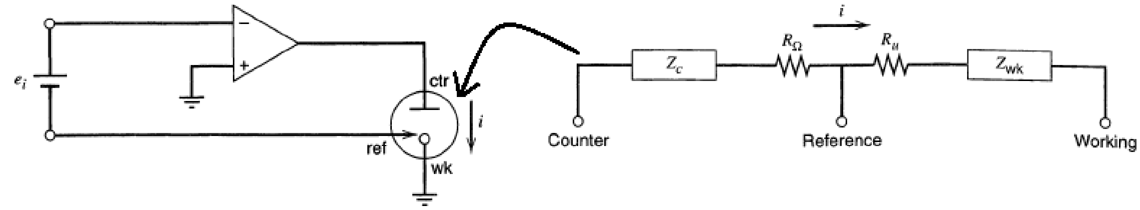

Figure 28: Electrical schematic of a potentiostat and electrochemical cell in solution.[37]

4.2.2.3 Chronoamperometry

The main focus of this project was constant voltage deposition using a technique called chronoamperometry. In chronoamperometry, current was monitored between the working and counter electrodes versus time, as the potential between working and reference electrodes was held constant. The voltage was held constant because in electrodeposition there is a range in potential where certain metals can optimally be deposited. This selectivity is necessary to deposit ZnO, which will be discussed in Chapter 5. This is also the main method used in all ZnO depositions from literature.[30–34,42,44,45,54–56] Using this technique ZnO was deposited on ITO and silicon substrates. The full detailed experimental fabrication procedures can be found in Appendix A.

4.3 Patterning of Electrodeposited ZnO

Although a self-assembled moth-eye array with nanoscale periodicity and height was the end goal of this research, the ability to pattern ZnO on the nanoscale is essential for many optical applications with set dimensions and requirements such as UV photodetectors, or dye-sensitized solar cells.[57,58] For the fabrication of a UV photodetector, ZnO nanowires are grown thermally at 500ºC for 2 hours, ranging in thickness from 40 – 400 nm.[57] From Zhang et al,[58] ZnO nano arrays compiled in a two electrode photocapacitor showed outstanding photoresponse, rechargeability, and long-term storage properties.[58] These nano arrays had a periodicity of 140 nm. In order to engineer materials that are controllable in the micro/nanoscale for achieving specific optical properties such as absorption and photoluminescence, which are additionally tunable in the micro/millimetre length scale for effective electrical biasing and contact, a new fabrication method was created based on top-down and bottom-up fabrication and patterning of semi-conductive materials.

The electrodeposition process used in both methods described below was performed at a potential of -1.1V at 65ºC for 2 minutes with the same procedure described in Appendix A. The solution consisted of 0.05M $Zn(NO_3)_2$ and 0.025M H_2O_2. The substrate used was ITO, which was fabricated the same way as shown in Appendix A.

Two methods were used for combining electrodeposition with photolithography: 1) Top-down + bottom-up, and 2) Bottom-up + top-down. Top-down + bottom-up is a fabrication method where the photolithography patterning is completed on the substrate and then the ZnO is grown in the pattern already formed. In Bottom-up + top-down, the ZnO is grown on the bare substrate and photolithography patterning is conducted on top of the thin film. The film is then etched to form the mask pattern used. The patterned structure deposited was rails that were staggered one over the other, which can be seen in Figure 29. Figure 30 shows the fabrication and photolithography of both processes of patterning ZnO. The detailed fabrication method can be found in Appendix A.

Figure 29: The mask used for photolithography.

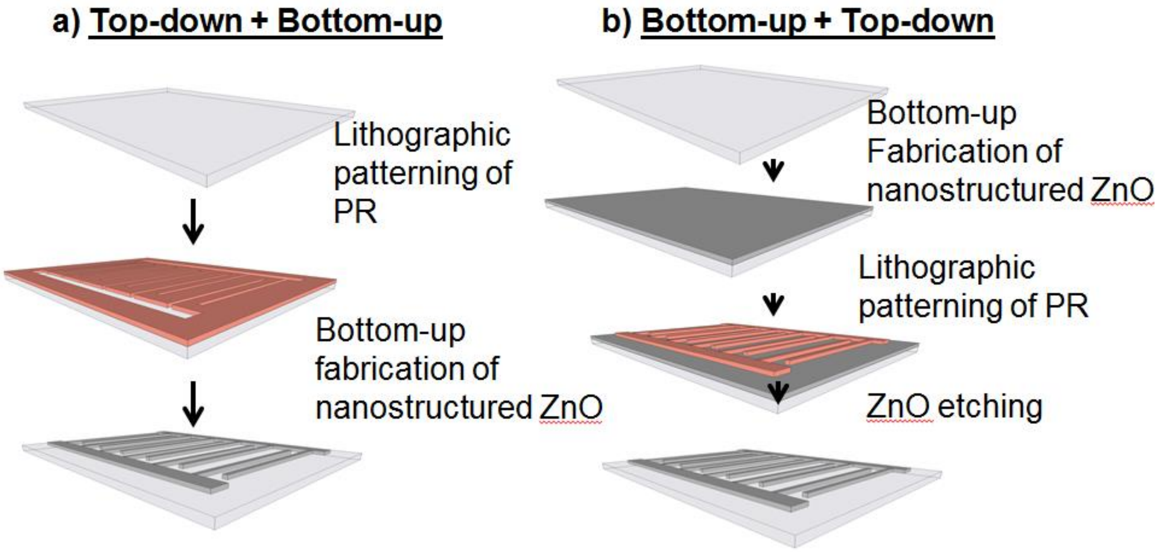

Figure 30: ZnO patterning fabrication a) Top-down + bottom-up, and b) Bottom-up + top-down.

In Appendix A, the detailed methods used for the fabrication of ZnO through electrodeposition on ITO and silicon substrates are presented. Multiple parameters were changed including: voltage, solution composition, temperature, substrate used, and deposition time to create thin films with different characteristics. Patterning of these ZnO thin films was also conducted using photolithography techniques and wet etching. The result was the completion of two patterning fabrication methods for these ZnO electrodeposited films; Top-down + bottom-up and Bottom-up + top-down fabrication. The next chapter will demonstrate the characterization of these ZnO thin films that have been electrodeposited and also patterned.

Chapter 5: Characterization Techniques

Once the ZnO thin films were prepared, they needed to be characterized in order to better understand their optical properties and to study the role of structure on the functionality of this material. First, scanning electron microscopy (SEM) was used to show the thin film structures and how they formed on the nano-scale. SEM was also used to compare structures with different deposition parameters, which include the electrodeposition parameters in Appendix A, Table 1. X-ray diffraction and energy dispersive X-ray spectroscopy were used to prove that the thin films were indeed composed of ZnO. The ability to transmit light and reduce reflection over the solar spectrum are important optical properties for any anti-reflection coating, so UV-Vis spectroscopy was completed on different ZnO electrodeposited films.

5.1 Scanning Electron Microscopy

The operation and background theory on SEM can be found in Appendix B. The SEM system can be operated under different modes by varying the accelerating voltage, probe current, detector type, and working distance. We used the low voltage mode of 1 kV at a working distance of 6mm in order to capture as much detail on the surface of the structure formed. This mode operates at an accelerating voltage of about 1kV which corresponds to a low beam energy, and the penetration depth is defined as:[59]

$$R = \frac{0.0276A*E_o^{1.67}}{Z^{0.89}p} \quad (5.1.2)$$

where R is the penetration depth in micrometers, A is the atomic weight, Z is the atomic number, p is the density, and E_o is the beam energy. At higher voltages, higher beam energy results in image distortion due to charging effects from the penetration depth. The low voltage imaging mode was chosen to reduce the charging effects when non-conducting layers were present beneath the deposited layer (such as glass). Figure 31 displays the penetration depths when using different electron beam energies. In Figure 32, the difference in image quality with accelerating voltages at two different levels is shown. The left image is taken at 10keV while the right image is taken at 25keV. The loss of detail is apparent on the surface of the structures in the right image, and some charging is occurring around the large structure.

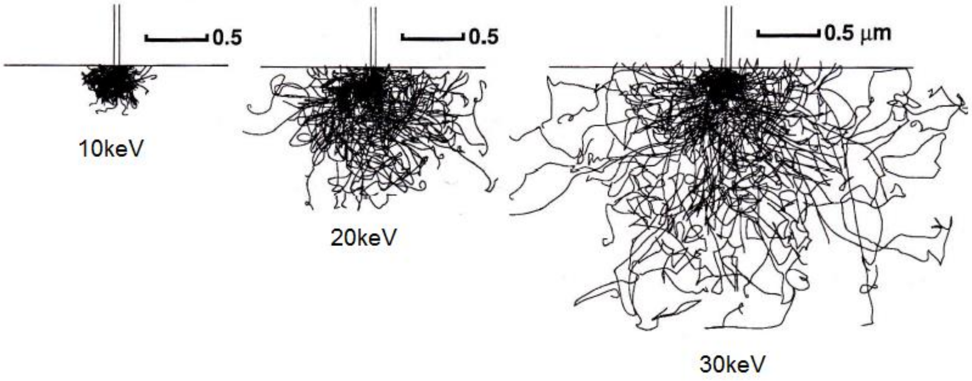

Figure 31: The effect of accelerating voltage creating a beam energy on the penetration depth in a sample.[59]

The contrast and the brightness of the image are directly related to the accelerating voltage; consequently, using a lower voltage results in an image that is dim, and the contrast is low compared to the higher voltage image in which structure boundaries are easily seen. Since we were analyzing the surface structure of ZnO thin films with depths of less than a micron, a 1kV accelerating voltage was used to better resolve the samples' features at over 50,000 times the magnification.

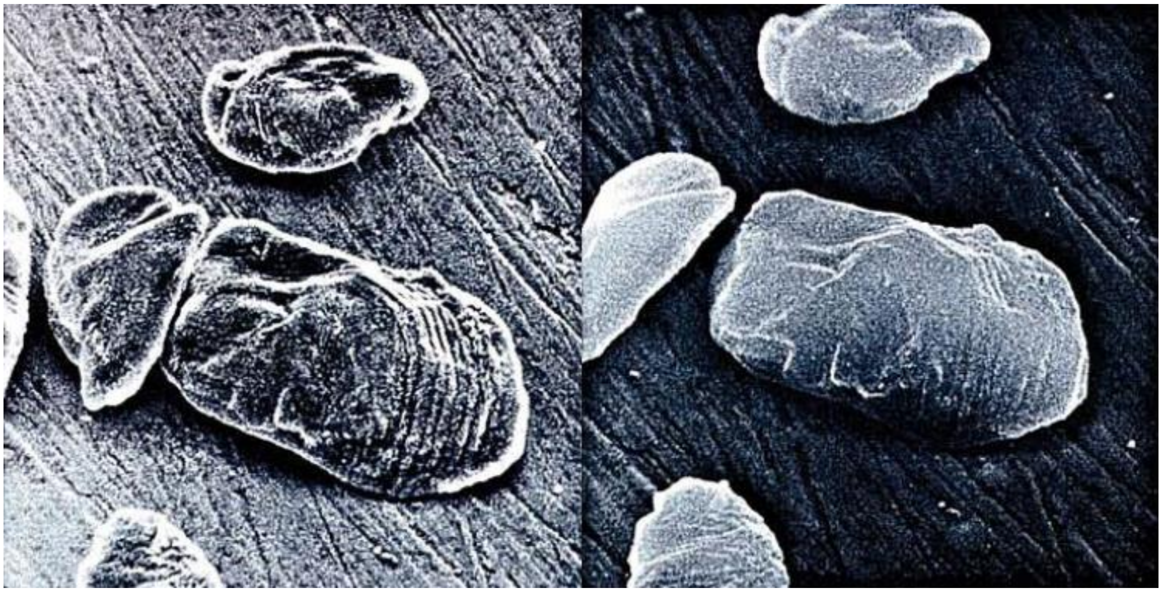

Figure 32: Comparison of voltage chosen: left voltage is 10keV and right voltage is 25keV.[60]

5.2 Energy Dispersive X-ray Spectroscopy

Energy dispersive X-ray analysis was completed with the SEM system. In this technique, the electron beam was focused on the sample with an accelerating voltage of 15kV. This voltage was chosen as it causes the excitation of a zinc atom with X-rays, in turn causing emission. Once excited, the zinc atom ejects an electron from its inner shell.[59] An electron from the outer shell then fills its place, and the extra energy of transforming from a high energy shell to a low energy shell is released as an X-ray.[59] The number and energy of these X-rays is then measured, and since these X-rays have an energy which corresponds to the atomic structure of the element from which they were emitted, we are able to obtain information regarding the composition of the specimen. This allows for the identification of the types of elements and their relative abundance in the selected region.

5.3 X-ray Diffraction: Composition Analysis

The X-ray diffraction (XRD) technique was used to ascertain the composition of electrodeposited thin films. The theory behind X-ray diffraction and the operation of the X-ray diffraction machine can be found in Appendix B. Once a diffraction pattern was formed, it was then possible to determine the material's composition by using the 2θ peak locations and searching the database for a similar peak distribution. By using Bragg's Law (Appendix B), one can see that low 2θ angle peaks correspond to planes with large d-spacing and vice-versa.[61] This is beneficial when identifying different materials and matching experimental data with known diffraction patterns.

5.4 UltraViolet-Visible Spectroscopy

UV-Vis spectroscopy was used to measure the transmission of light in the 300-1100 nm wavelength range. The results are discussed in the following chapter and the theory can be found in Appendix B. The Cary 50 system located in the Department of Chemistry at McMaster University was used for performing the absorption/transmission measurements. This type of spectroscopy measures the transmission of radiation with respect to wavelength. Figure 33 shows the operation of the Cary 50 system. First, a beam of light is generated from a source in complete darkness. Part of this emission is absorbed by the sample, while the other part is transmitted through the sample to the spectrometer on the other side. The spectrometer has the ability to detect radiation between 300 nm and 1100 nm by the use of a CCD. Light strikes the individual pixels across the CCD and each pixel represents a portion of the spectrum that the electronics can translate and display with a given intensity. The spectrometer essentially has the ability to resolve light into different wavelengths; therefore, a relationship between the transmission of light over the wavelength range is displayed.

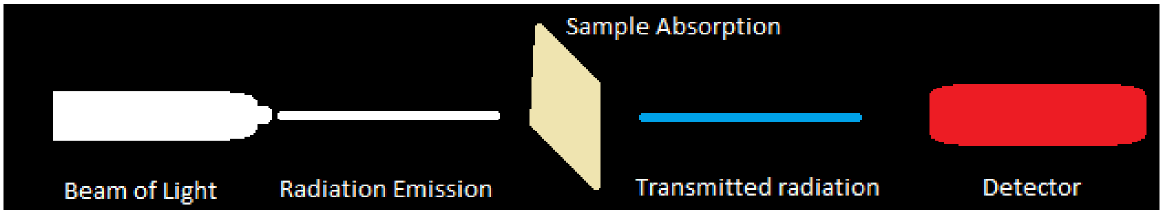

Figure 33: The Cary 50 spectroscopy system.

Reflection mode UV-Vis spectroscopy was also completed on these ZnO thin films. The substrate used was a highly reflective substrate (silicon -

approximately 35% reflection) on which the ZnO thin films were electrodeposited. Reflection mode UV-Vis spectroscopy is very similar to the transmission mode UV-Vis spectroscopy. The main difference is that the detector is positioned at the highest intensity of reflection, which is at the angle of incidence. This is depicted in Figure 34. The incident light is focused on the substrate at a known angle of incidence with respect to the substrate normal. The detector is then positioned at that known angle on the other side of the normal plane. The reflected light is captured by the detector, which is then represented as a percentage of reflected light vs. wavelength in the spectrum. The detector and spectrometer function the same way as in transmission mode UV-Vis spectroscopy. From the results of reflection-mode UV-Vis spectroscopy, we are able to compare the reflection over many different angles of incidence (10º-70º) in the designated wavelength range (300 nm – 1150 nm). The results for reflection from these ZnO thin films are then compared to bare silicon substrates, and differences in reflection percentages are noted.

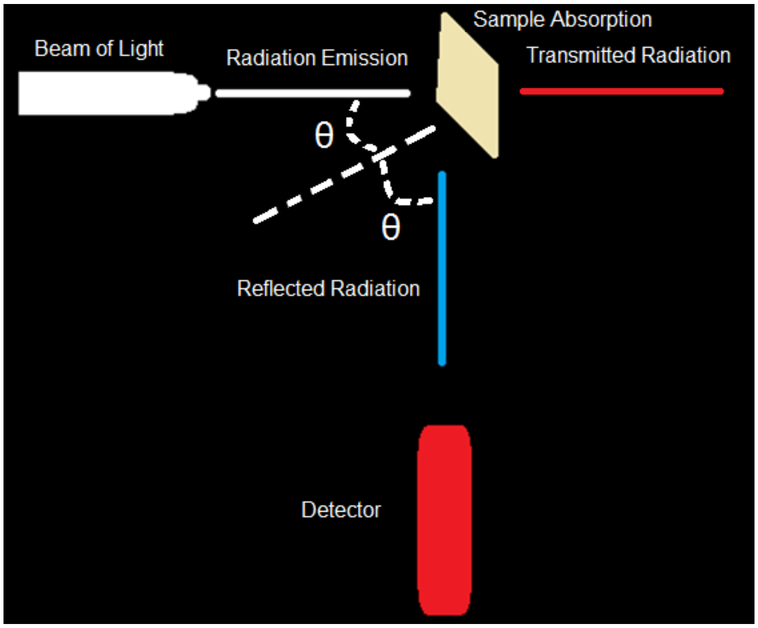

Figure 34: Reflection mode UV-Vis spectroscopy.

In the next chapter, the characterization results of the structures deposited using the fabrication procedures from Appendix A and characterization methods of Chapter 5 are presented and discussed.

Chapter 6: Results and Discussion

This research was focused on developing and optimizing methods for controllable deposition of ZnO over multiple lengthscales ranging from the microscale to the nanoscale. Bottom up electrodeposition and a combined top-down/bottom up method for deposition and patterning of ZnO were developed and optimized. With the vision of creating a moth-eye antireflection coating, we conducted a study to understand the effect of electrodeposition parameters including temperature, applied potential, type of reagents and their concentrations on the morphology of deposited particles. This moth-eye array would need to have a height of 400 nm with a periodicity of about 100 nm as discussed in Chapter 1; this 4 to 1 aspect ratio can promote optimal antireflective properties. Two different substrates were used for deposition: (100) silicon and indium tin oxide (ITO). The bulk of this work deals with the electrodeposition of ZnO thin films on ITO; however the findings from the ITO-based experiments were transferred to electrodeposition on silicon substrates to create proof-of-concept anti-reflection material on this substrate. Different electrochemistry parameters were altered to achieve an optimal ZnO structure for optical applications. The structures of the thin films were then analyzed using Scanning Electron Microscopy (SEM), while reflectance measurements were conducted using UV-VIS Spectroscopy. The presence of ZnO was confirmed via the use of X-ray Diffraction and Energy Dispersive X-ray Spectroscopy (EDS or EDX).

6.1: Initial Electrodeposition Parameters

6.1.1 Effect of Temperature

Films were first deposited using a solution of 0.05M $ZnCl_2$ and 0.025M H_2O_2. The voltage and deposition time was kept constant at -1.4V and 2 minutes in order to observe the change in density and structure with temperature.

6.1.1.1 Results

Figure 35 shows the electrodeposition of thin films at two temperatures. The structures in Image a) were deposited at 65^{o}C; we see elongated particles tangential to the substrate surface that had an average particle size of 1 - 3 um. Figure 35b demonstrates ZnO deposited at 80^{o}C containing three dimensional flake-like structures having a particle size of 2 – 5 um. There seems to be an uncoated region in between particles of Figure 35a, whereas the substrate of Figure 35b is densely coated with deposited particles. Image b) which was deposited at 80^{0}C had a considerably higher density than structures in image a). Multilayers were forming causing the electrodeposited thin film to be less uniform. This deposition started growing layer upon layer as can be seen in image b). The sharp blades started forming clusters on the bottom deposited layer.

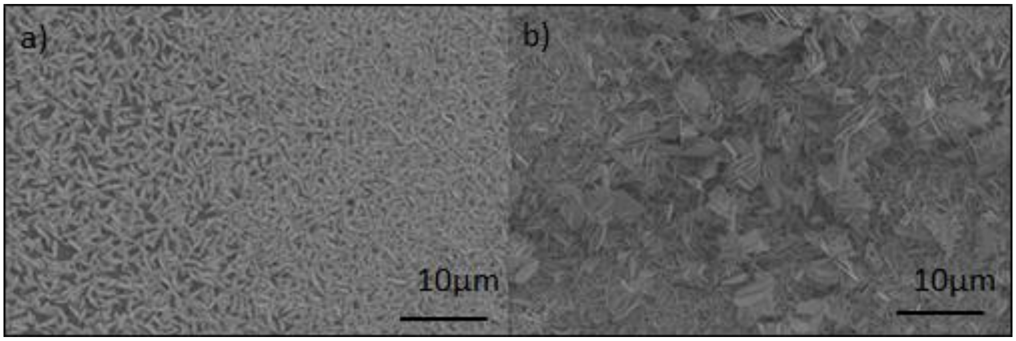

Figure 35: Topographical images of thin film deposited with 0.05M $ZnCl_2$ and 0.025M H_2O_2 solution with an applied potential of -1.4V at temperatures, a) 65^{0}C b) 80 ^{0}C.

6.1.1.2 Discussion

Based on SEM micrographs demonstrated in Figure 39, we see that depositions performed under the same conditions (Solution - 0.05M $ZnCl_2$ and 0.025M H_2O_2 at-1.4 V) and duration, yield larger structures at higher temperatures. Consequently we expect the deposition rate to increase with increasing temperature. Previous studies, performed at -0.75V, using 0.005M $ZnCl_2$ and 0.1M KCl solution demonstrated an increase in deposition rate when temperature was increased in the 25-90ºC range. Based on work from Pauporte et al., the increased dissociation rate of H2O2 at elevated temperatures resulting in increased concentration of reactive oxygen radicals has been associated with this increased ZnO electrodeposition rate.[30,43] The temperature of a solution has a direct relationship to the deposition rate.[31] Based on the above mentioned results and literature findings, I hypothesize that heating up a solution of 0.05M $ZnCl_2$ and 0.025M H_2O_2 allows the oxygen bond in hydrogen peroxide to dissociate in order to combine with zinc; the lower the temperature of the solution, the slower the decomposition. An increase in temperature will thus result in two highly reactive oxygen radicals, which in turn increases the rate of electrodeposition. From the literature[30,43,62] ZnO is widely electrodeposited at a temperature of 65^{0}C or higher with potentials in the range of -0.75V to -1.4V, which is in line with our findings that controllable deposition with moderate deposition rate is achievable at this temperature. The next parameter to be tested is the overpotential/voltage applied to the electrochemical cell.

6.1.2 Effect of Voltage

6.1.2.1 Results

In Figure 36 the temperature was held constant using the same solution as in section 6.1.1 and the voltage was changed for the two depositions, one at -1.1V and the other at -1.7V. The samples were electrodeposited for 2 minutes. Structures presented in Figure 36 images a) and b) were deposited and measured for film thickness by using an optical profilometer in the CEDT clean room. The thicknesses of the two films presented in images a) and b) were approximately 1.3 μm and 2.2 μm respectively. When depositing at -1.1V as depicted in image a), the features are in the form of polygons with edges of approximately 1um that formed at random angles with respect to the surface (blades), and there is a large particle density. The structures in image b) show a completely different morphology, nodular structures have formed, combining with each other to form snake-like structures. However, the sample deposited at -1.7V was not completely uniform. There were areas with different densities (data not shown) as the deposited region got closer to the deposition- solution interface the density reduced. This visible observation was confirmed by the profile recorded on the optical profilometer computer interface; it displayed the thickness of the film, and it was reducing as the measurement came close to the deposited area-ITO interface, while at -1.1V the density was uniform throughout.

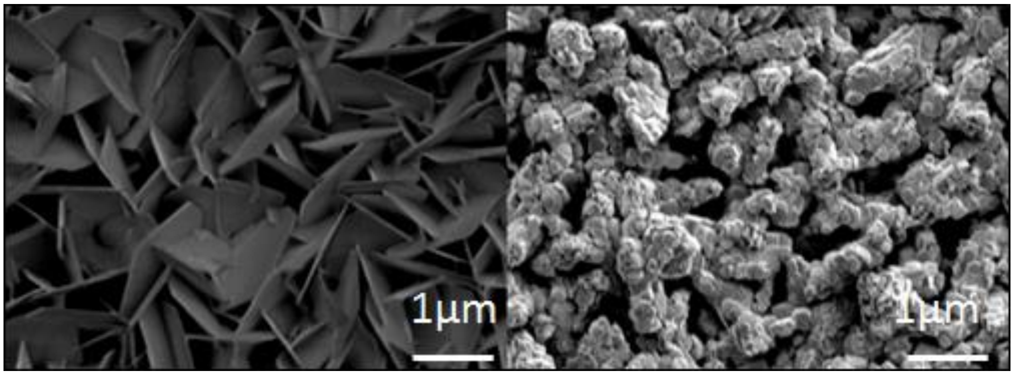

Figure 36: Topographical images of thin film deposited with 0.05M $ZnCl_2$ and 0.025M H_2O_2 solution at 65ºC, for 120s with different voltages a) -1.1V b) -1.7V.

6.1.2.2 Discussion

The voltage applied to the electrochemical cell is the driving force of the reaction required to electrodeposit ZnO on the working electrode in solution. In the results presented above there was a change in morphology with the change in potential. The density of the structures, and particle sizes were also directly related to the potential change. In ZnO electrodeposition study completed by Marotti et al[42] with using a 0.1M $Zn(NO_3)_2$ solution at 85ºC, he also recorded a morphology, density, and particle size change by effectively changing the potential from -0.8V to -1.1V. Therefore one hypothesize is that by varying the voltage in electrodeposition one can fine tune structural properties. The uniformity of the deposition was the most important part going forward. When characterizing the surface, only the thin film at -1.1V, deposited uniformly. At -1.7 V, the structures were not uniform and thickness of the thin film decreased the closer the thin film came to the ITO interface. This was due to the fact that the overpotential was moving farther away from the equilibrium potential discussed in Chapter 3.[39] Given that more uniform deposition was observed at -1.1 V compared to deposition at -1.7, -1.1 V was chosen as the deposition potential for the remainder of the experiments.

6.2: Time Evolution Studies

In order to better understand the effect of different electrodeposition parameters including potential, concentration of the zinc salt, and type of the zinc salt, on the morphology and density of the ZnO thin film building blocks, we perform time evolution studies of the electrodeposition processes. Time evolution studies involved performing electrodeposition at 10s, 20 s, 30s, and 40s on ITO samples that were prepared through identical processes based on the protocols presented in Appendix A. We assume that the electrodeposition occurring on substrates prepared using identical methods are equivalent. Electrodeposition experiments were repeated multiple times to lessen the effect of substrate to substrate variation.

6.2.1: 0.05M $ZnCl_2$ and 0.025M H_2O_2 Solution – results

The same electrodeposition conditions used in section 6.1.2 for fabrication of the blade structures shown in Figure 36a) were employed for performing the first series of time evolution studies. These experiments were done in solutions containing 0.05 M ZnCl2 and 0.025M H2O2, heated at 65°C, at a potential of -1.1 V. In order to have the same substrate surface area exposed to the solution for the following electrodeposition experiments, and for having similar optically-transparent surface areas for optical measurement, we use the vinyl masking technique described in Appendix A to solely expose a 6mmx 6mm area.

The SEM images shown in Figure 37 display the growth of the blades following 10s, 20s, 30s, and 40s of electrodeposition. At 10s, worm-like flakes with lengths in the range of 100nm to 500nm formed on the electrode surface. These would be the nucleation sites formed. At 20s, the blade structure is starting to grow off the initial nucleation sites formed; these beginning stages of blade growth have widths in the range of 300 nm to about 1 um. At 30s, these blades grow in random orientations with lengths ranging from 500nm to 2 um. At 40 s the growth of these structures has just about covered the whole surface of the electrode and these blades, which are randomly oriented, are no larger than 2 um in length and no wider than 1 um in width. From the tilted sample at this deposited time the peaks of some of the blades are visible but still they are randomly oriented.

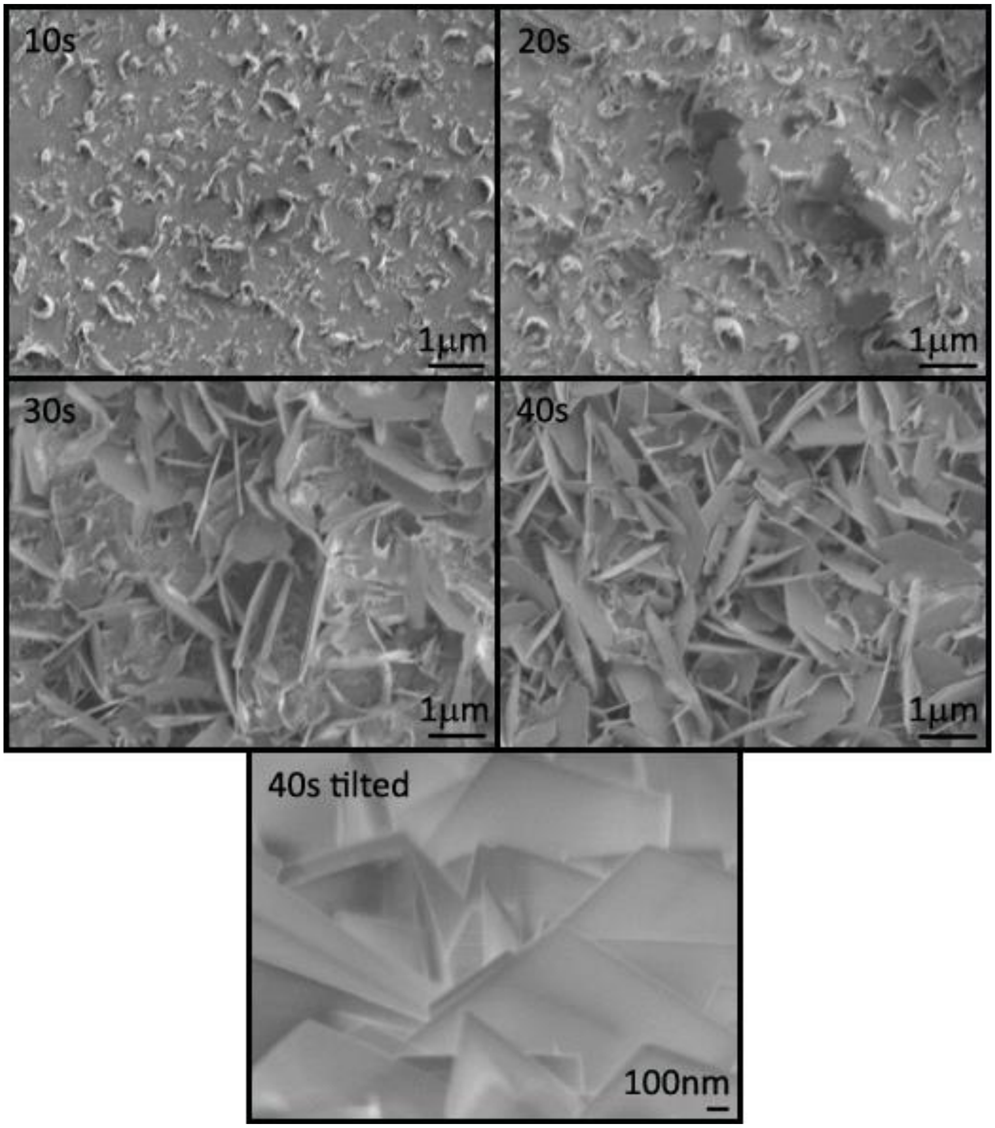

Figure 37: Time Evolution for electrodeposition using 0.05M $ZnCl_2$ and 0.025M H_2O_2 Solution at -1.1V, and $65^{o}C$ with magnified 40s sample that was tilted to 80^{0}.

The I-t curve in Figure 38 represents the electrodeposition current response for these blade structures deposited in Figure 37 at -1.1V. The first thing that can be seen is the initial current drop to a local minimum at 6s. Then there is a rapid linear increase in current and a gradual leveling off and small decrease tailing off (onset at 27s) at the end of the 40s.

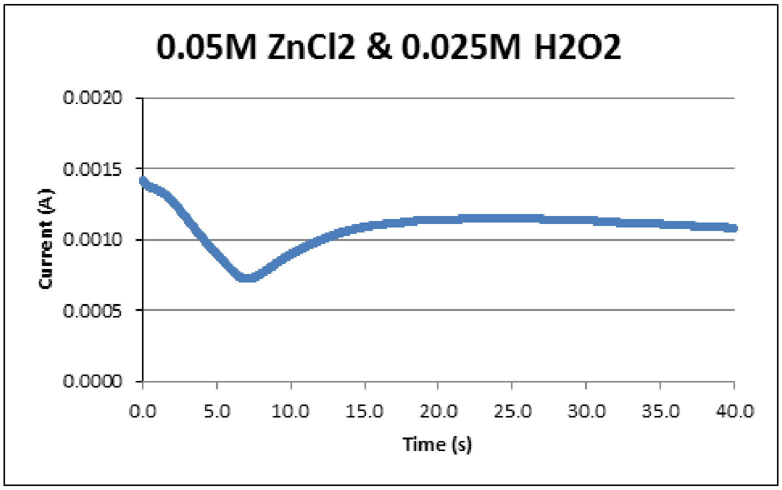

Figure 38: Current vs. time graph when using the 0.05M $ZnCl_2$ and 0.025M H_2O_2 Solution for electrodeposition.

6.2.2: 0.005M $ZnCl_2$ and 0.0025M H_2O_2 Solution

The concentration of the previous solution was then lowered to one tenth of its initial concentration, based on the previous work by Peulon at el[32] showing a decrease in growth rate with decreasing zinc salt concentration. We hypothesized that obtaining smaller features in the 100nm-400nm lengthscale could be achieved by lowering the concentration of the Zinc salt. The results can be seen in Figure 39. At the 10s deposition, it can be seen that very little nucleation has occurred on the electrode. Approximately 49 structures formed with an average diameter of 100nm and an oval/circular projection that covers about 1% of the total area. At 20 s, these structures did not grow in average diameter but the coverage increased to approximately 4% with 220 structures forming. At 30s, a fractional increase in the amount of structures was formed, with approximately 240 but the average diameter of structures has grown to about 150 nm, covering approximately 6% of the total area. At 40s the circular/oval structures did not grow in size having approximately the same average diameter as in 30s but the coverage has increased to 9% of the total area with increase in the number of structures to roughly 355. As evidenced in the 40s, tilted at 80^0 image shown in Figure 39, the structure is no longer grown in micron blades as seen with higher ZnCl2 concentration demonstrated in Figure 37. The low concentration solution formed pyramidal structures with a base of approximately 150 nm in length. This is why the structures look oval/circular from the topographical view. The growth characteristics, as well as the density of these structures have vastly changed from those at high concentration. Though, this provides the required lateral nanoscale dimension for a moth-eye array, the structure height and density must be further optimized.

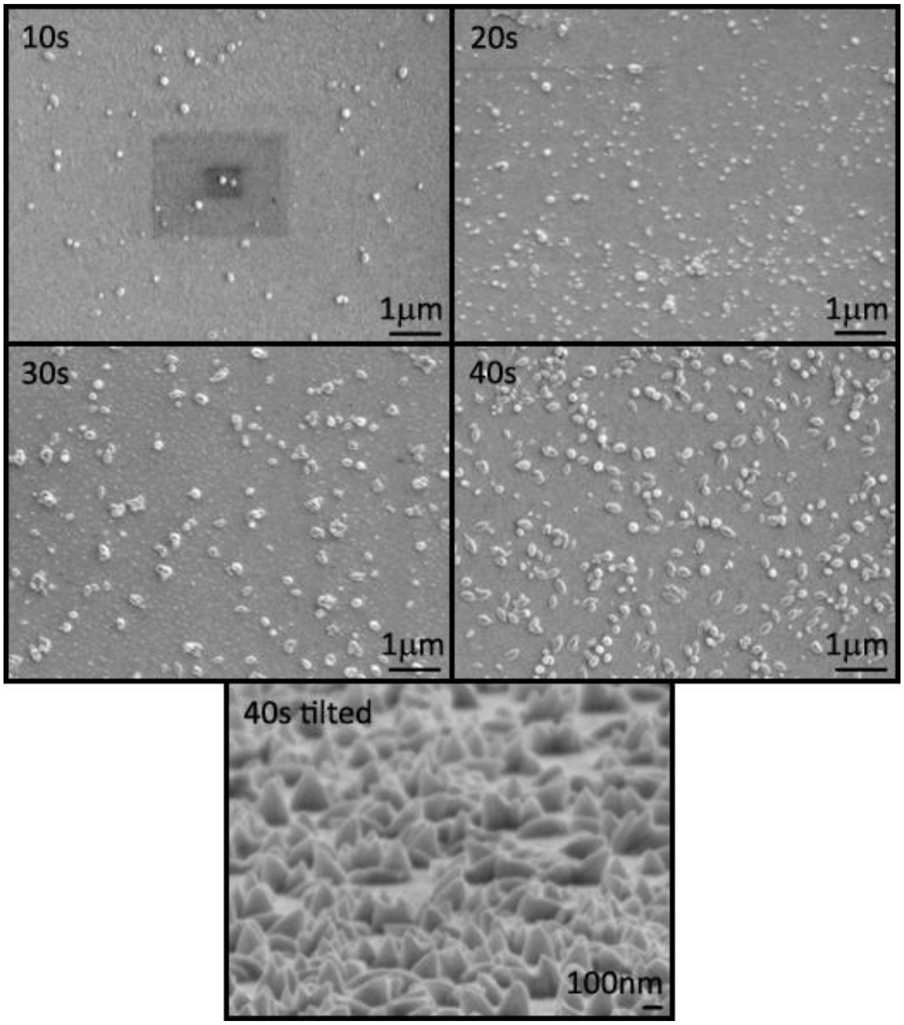

Electrodeposited Samples using 0.005M $ZnCl_2$ & 0.0025M H_2O_2 Solution				
Deposition time (s)	10	20	30	40
# of Particles	49	220	240	355
Average Diameter (nm)	105	102	155	148
Fraction of area Covered (%)	1	4	6	9

Figure 39: Time evolution studies for electrodeposition using 0.005M $ZnCl_2$ and 0.0025M H_2O_2 Solution at -1.1V, and 65ºC. (Top) Top-view SEM micrographs at different time intervals with magnified 40s sample that was tilted to 80^0. (Bottom) A table summarizing the number of particles, average diameter and the percentage of area covered in the image for each deposition.

The I-t curve in Figure 40 represents the electrodeposition current response for the pyramidal structures deposited at a 0.005M $ZnCl_2$ concentration in Figure 39. The first thing that can be seen is the very low current response at this low concentration compared to the current response at the 0.05M $ZnCl_2$ concentration. The initial current drop lasts slightly longer than that from the high concentration and the first local minimum is found to be at approximately 10s. Then there is a very slow linear increase in current which does not come to a local maximum.

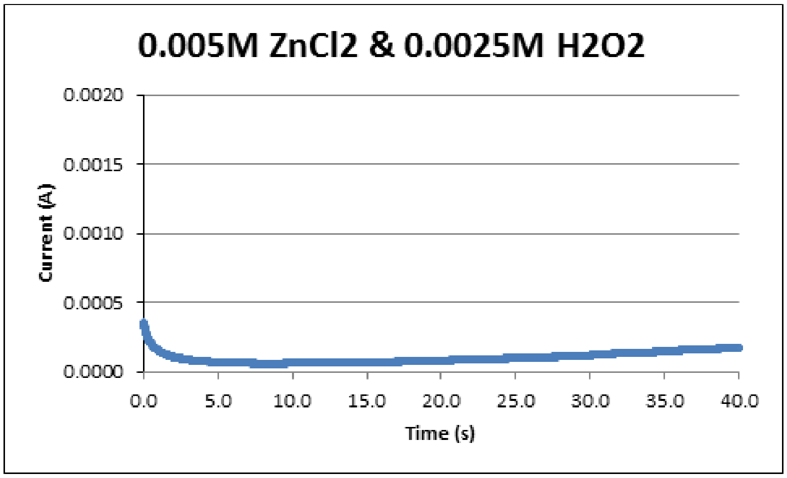

Figure 40: Current vs. time graph when using the 0.005M $ZnCl_2$ and 0.0025M H_2O_2 Solution for electrodeposition.

6.2.3: 0.05M $Zn(NO_3)_2$ and 0.025M H_2O_2 Solution

The Zinc chloride salt in the solution was then replaced with $Zn(NO_3)_2$, as it has also been used for ZnO deposition in the literature from Chong et al.[55] In literature the $Zn(NO_3)_2$ was used as the oxygen source, however, we added H_2O_2 as an additional source for oxygen because we expect the H2O2 to dissociate into two highly reactive oxygen radicals in the 65ºC bath, increasing the rate of electrodeposition.[30,43] The nitrate ions dissociate in solution by the following reaction:

$$NO_3^- + H_2O + 2e \rightarrow NO_2^- + 2OH^-$$

The goal was to attempt this rapid electrodeposition method from section 6.2.1 with another zinc salt to further demonstrate the tunability of the electrodeposited structures. In Figure 41, the SEM micrographs of the time evolution study are displayed for a 0.05M $Zn(NO_3)_2$ and 0.025M H_2O_2 Solution. At 10s the structures have a circular projection with an average diameter of 92 nm. There are approximately 920 structures that have formed in this area causing the coverage to be roughly 17% of the total area in the image. At 20s the coverage is similar except the structures have grown in size with an average diameter of 123 nm. However, there are only 726 structures that comprise 19% of the total image area. At 30s, the structures grow larger with an average diameter of 250 nm. The amount of these larger structures formed has decreased to 387 but the coverage has increased to approximately 36% of the total. By 40s, the electrode is fully covered with hemispherical structures covering approximately 95% of the total area. However, the average diameter and amount of structures could not be calculated accurately with the image j software due to the lack of spatially resolved structures in the image. However if we were to estimate the average diameter from visible observation it could be approximately be 400-500 nm. The 40s tilted sample shows that the preferred orientation is geared towards forming a smooth, thick layer. The spherical particles are growing laterally until all area is covered and new nucleation is no longer present. Comparing to the 0.05M $ZnCl_2$ deposited samples at 10s, the $Zn(NO_3)_2$ forms less dense structures that are smaller by approximately 400nm. As time continues over 20 and 30 s seconds, the $ZnCl_2$ growth produces more random oriented blades, whereas hemispherical structures are developed here. The advantage of this method is that the moth-eye hemispherical structure is formed; however the 400nm height and periodicity of 100 nm still need to be optimized because these structures are much larger with an approximate diameter of 500 nm and height of 800 nm measured using the optical point profilometer.

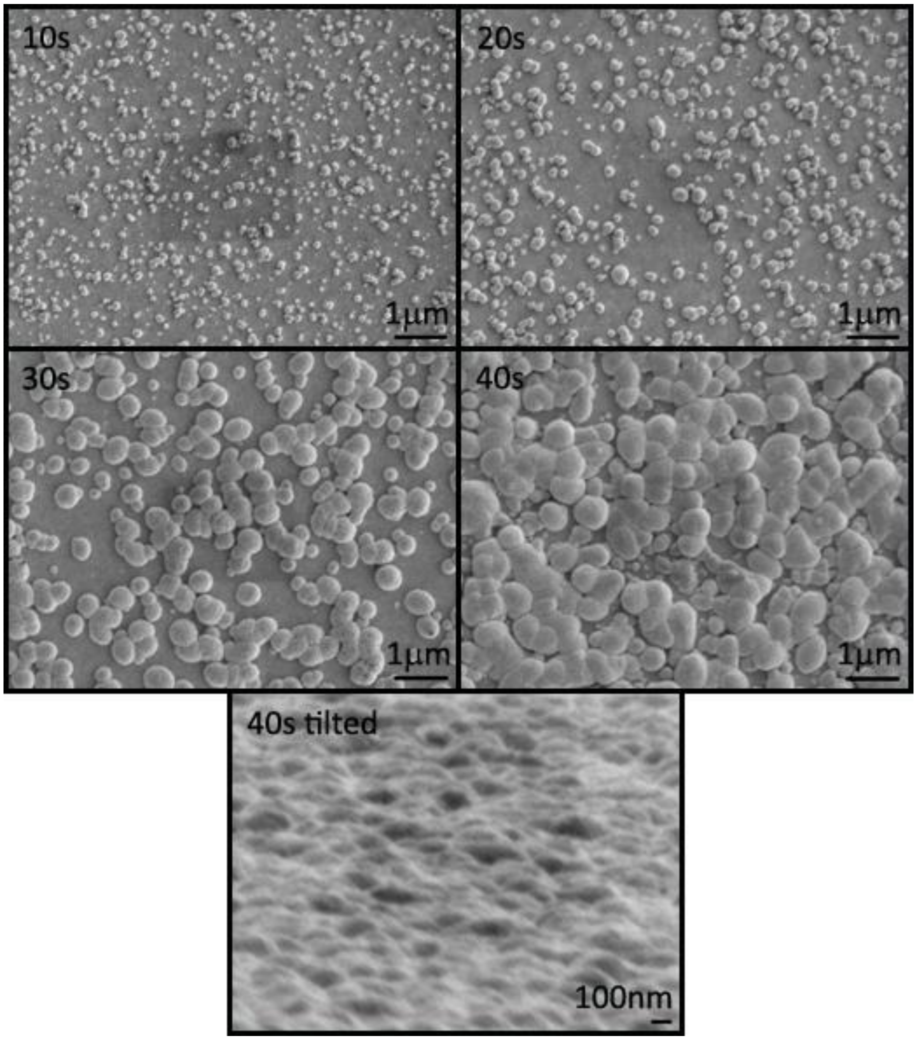

Electrodeposited Samples using 0.05M $Zn(NO_3)_2$ & 0.025M H_2O_2 Solution				
Deposition	10s	20s	30s	40s
# of Particles	920	726	387	N/A
Average Diameter (nm)	92	123	250	N/A
Fraction of Area Covered (%)	17	19	36	95

Figure 41: Time Evolution studies for electrodeposition using 0.05M $Zn(NO_3)_2$ and 0.025M H_2O_2 Solution at -1.1V, and 65^{o}C. (Top) Top-view SEM micrographs at different time intervals with magnified 40s sample that was tilted to 80^{0}. (Bottom) A table summarizing the number of particles, average diameter and the percentage of area covered in the image for each deposition.

The I-t curve in Figure 42 represents the electrodeposition current response for these hemispherical structures deposited in Figure 41 at -1.1V. The first thing that can be seen is the initial current drop to a local minimum at 8s. Then there is a linear increase in current and a gradual leveling off for the current at 40s. Comparing to the curve when the 0.05M $ZnCl_2$ solution was used, the overall current is lower when depositing with a $Zn(NO_3)_2$ solution. It also takes approximately an extra 7 seconds to level off at a steady current after the linear increase. Also, there is a tail end decrease in the $ZnCl_2$ around 35s compared to no visible decrease below.

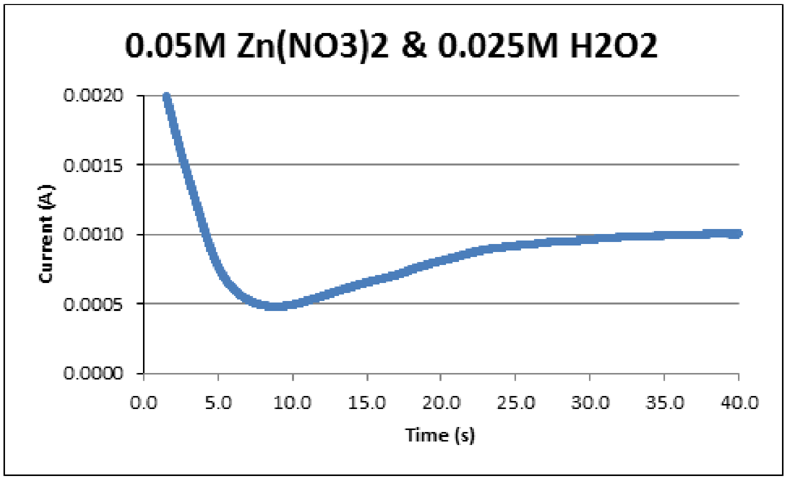

Figure 42: Current vs. time graph when using the 0.05M $Zn(NO_3)_2$ and 0.025M H_2O_2 Solution for electrodeposition.

6.2.4: 0.005M $Zn(NO_3)_2$ and 0.0025M H_2O_2 Solution

A lower concentration of $Zn(NO_3)_2$ was introduced with the goal of decreasing the structure diameter. Figure 43 demonstrates a series of SEM micrographs corresponding to electrodeposition performed in a 0.005M $Zn(NO_3)_2$

and 0.0025M H_2O_2 Solution at -1.1 V. At 10 s, only 2 structures are observed, however, at 20 s, nuclei have started to form and take a circular/oval shape with an average diameter of about 150 nm. However, only 17 particles are present contributing to a coverage that is less than 1% of the total area. At 30s, the average diameter of the structures has increased to almost 200 nm with roughly the same number of structures present (just under 40) with a negligible increase in the fraction of the surface area covered (half a percent). At 40s, the structure size has an average diameter of 200 nm which does increase from the 30s deposition but the amount of structures has drastically increased to 159. As a result the overall coverage change has increased to approximately 7.5% of the total area in the image. One feature to be noted in the 40s tilted image, is that the structure size and shape is similar to the structures formed with a lower concentration of $ZnCl_2$. One key difference is that when 0.005M $Zn(NO_3)_2$ is used, some structures connect with others forming a tulip shape compared to the pyramidal structure formed by 0.005M $ZnCl_2$. Also, when using the $ZnCl_2$ solution the most important observation is the drastic change in density. Using the $Zn(NO_3)_2$ instead of the $ZnCl_2$ caused less dense nucleation to form.

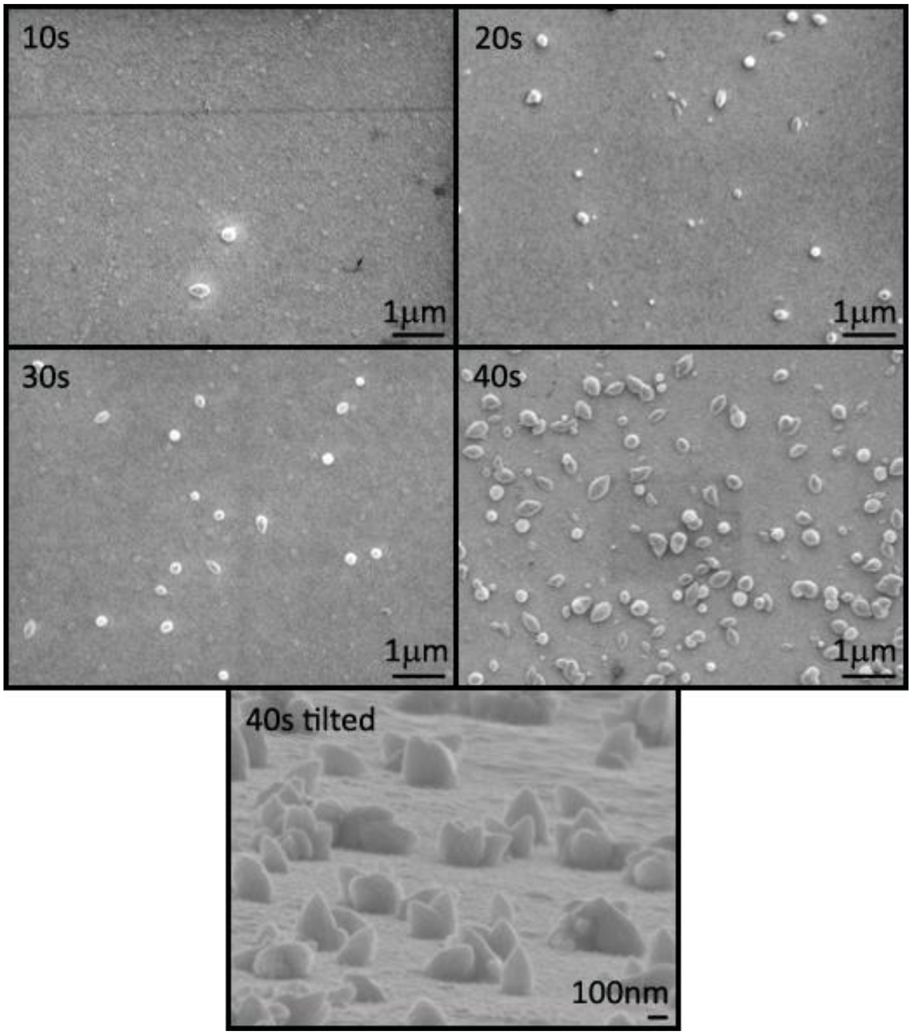

Electrodeposited Samples using 0.005M $Zn(NO_3)_2$ & 0.0025M H_2O_2 Solution				
Deposition	10s	20s	30s	40s
# of Particles	2	17	36	159
Average Diameter (nm)	366	154	195	200
Fraction of Area Covered (%)	0.3	1	2	8

Figure 43: Time Evolution studies for electrodeposition using 0.005M $Zn(NO_3)_2$ and 0.0025M H_2O_2 Solution at -1.1V, and 65°C. (Top) Top-view SEM micrographs at different time intervals with magnified 40s sample that was tilted to 80^0. (Bottom) A table summarizing the number of particles, average diameter and the percentage of area covered in the image for each deposition.

The I-t curve in Figure 44 represents the electrodeposition current response for the pyramidal structures deposited at low 0.005M $Zn(NO_3)_2$ concentration demonstrated in Figure 43. It is noted that very low current is observed at this low concentration compared to the low 0.005M $ZnCl_2$ deposition of Figure 39. The initial current drop lasts a lot longer than that from the high concentration and comes to a local minimum at 16s. Then there is a very slow linear increase in current which does not come to a local maximum. Comparing to the low concentration $ZnCl_2$ curve the decrease in current lasts for an extra 6s. The increase is also steeper in the 0.005M $ZnCl_2$ solution.

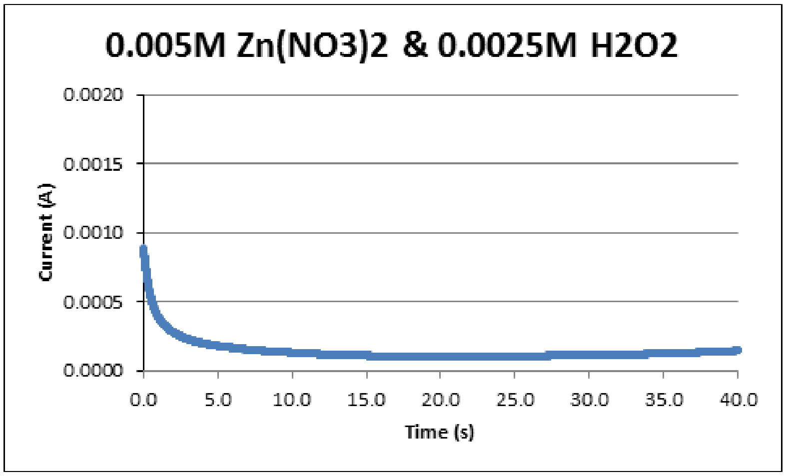

Figure 44: Current vs. time graph when using the 0.005M $Zn(NO_3)_2$ and 0.0025M H_2O_2 Solution for electrodeposition

From the results of the four time evolution studies, it can be concluded that structural size, morphology, and density are tunable. However the densities and size of these films still need to be optimized to form the desired moth-eye array. We hypothesize that lowering the potential (absolute value) at a high concentration of $Zn(NO_3)_2$ may form smaller structures like in research completed by Marotti et al. [42] Using a solution solely containing 0.1 M $Zn(NO_3)_2$, it was shown that structures decrease in size when reducing the potential from -1.1V to -0.8V. We also hypothesize that chloride ions in the $ZnCl_2$ solutions may be aiding in the development of a more dense structure which could help the growth of a moth-eye array with proper periodicity if incorporated with the zinc nitrate solutions. Research completed by Tena-Zaera,[47] display that the addition of KCl in a $ZnCl_2$ solution has a direct impact on deposition rate. Increasing the KCl concentration causes an increase in the deposition rate and enables the deposition of more faceted structures.[47] These two hypotheses regarding the role of the applied potential and chloride concentration are tested in the next two sections with the $Zn(NO_3)_2$ solution.

6.2.5: 0.05M $Zn(NO_3)_2$ and 0.025M H_2O_2 Solution with applied Potential of -0.8V

In order to reduce particle size compared to the structures formed in 6.2.3 and increase density compared to the structures formed in 6.2.4, a lower overpotential was used at a higher concentration of 0.05M of $Zn(NO_3)_2$ solution. In Figure 45, the particle size has decreased in comparison with the structures deposited at -1.1 V (particle diameter at 40s - 400-500nm) in the 0.05M $Zn(NO_3)_2$ solution (Figure 41) whereas the density has increased vastly in comparison to the samples deposited at lower concentration (0.005M) of zinc nitrate salt (Figure 43). At 10s nucleation can be seen and structures with an average diameter of 127 nm are deposited on the electrode surface. There were 408 structures deposited comprising of 9% of the total area in the image. At 20s there is an increase in the average diameter of the structures to approximately 174 nm, but the number of structures stayed roughly the same with 398 structures. Due to the increase in average diameter this increases the coverage of the thin film to 15% of the total area. At 30s, the structures have the same average diameter but the density has increased once again (563). This again noted an increase in overall covered area to 23%. At 40s deposition, the coverage has increased further through the increase in structure diameter (197 nm) and number of structures formed (613) giving a coverage of 31% with respect to the total area. In the tilted view image one is able to see that these hemispherical structures have a diameter of approximately 200 nm and a height a little over 200 nm. In this mode of electrodeposition, structures with three-dimensional geometries similar to those of a moth-eye are formed; however the structure density (100nm periodicity) and height (400 nm) are not optimal for an anti-reflective coating. In addition, there are uncoated areas where light can reflect directly from the initial substrate.

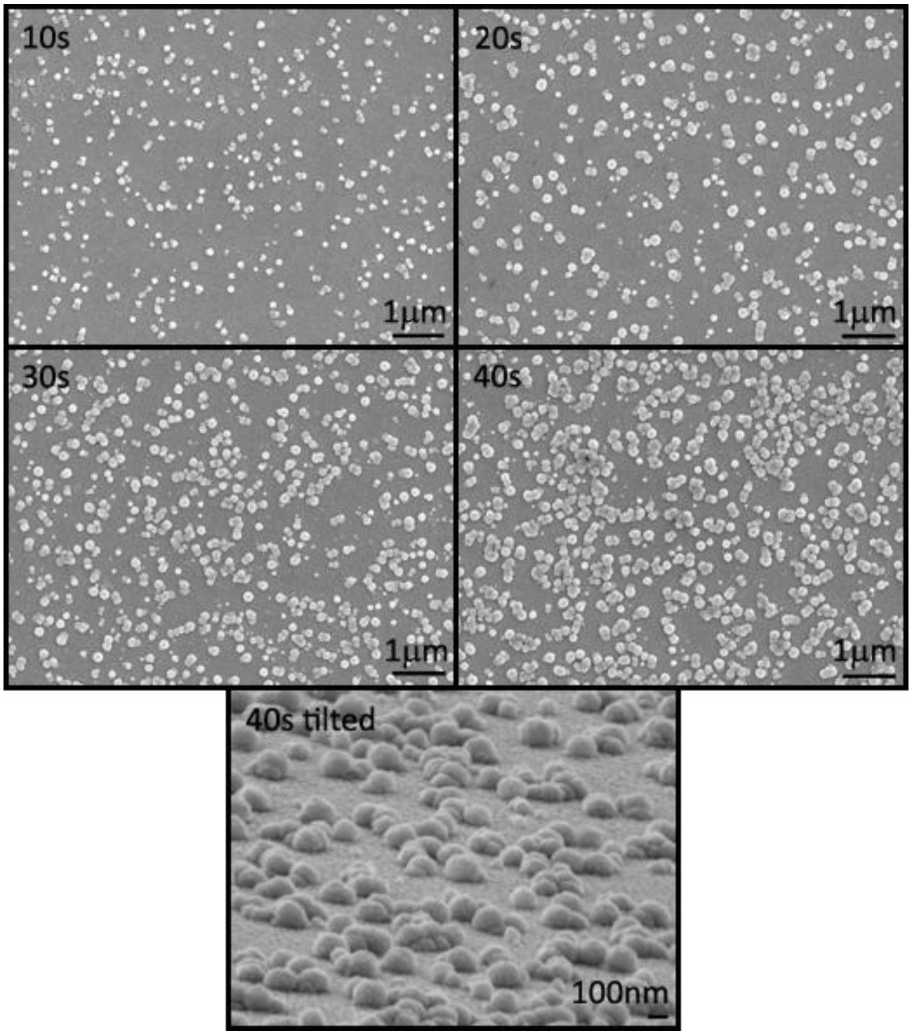

Electrodeposited Samples using 0.05M $Zn(NO_3)_2$ & 0.025M H_2O_2 Solution (-0.8)				
Deposition	10s	20s	30s	40s
# of Particles	408	398	563	613
Average Diameter (nm)	127	174	179	197
Fraction of Area Covered (%)	9	15	23	31

Figure 45: Time Evolution studies for electrodeposition using 0.05M $Zn(NO_3)_2$ and 0.025M H_2O_2 Solution at -0.8V, and 65°C. (Top) Top-view SEM micrographs at different time intervals with magnified 40s sample that was tilted to 80^0. (Bottom) A table summarizing the number of particles, average diameter and the percentage of area covered in the image for each deposition.

The I-t curve in Figure 46 represents the electrodeposition current response for the hemispherical structures deposited at with 0.05M $Zn(NO_3)_2$ at an applied potential of -0.8V in Figure 45. The initial current drop lasts longer than that from the high concentration zinc nitrate at -1.1V (Figure 42) but is much lower than the local minimum in the low concentration solution (Figure 44). It is decreasing to a local minimum at approximately 13s. Then there is a very slow linear increase in current which does not come to a local maximum. Comparing to the low concentration $ZnCl_2$ and $Zn(NO_3)_2$ solutions deposited at -1.1V (Figure 40 & 43 respectively), this current increase rate is much greater than depositions in both of the other solutions.

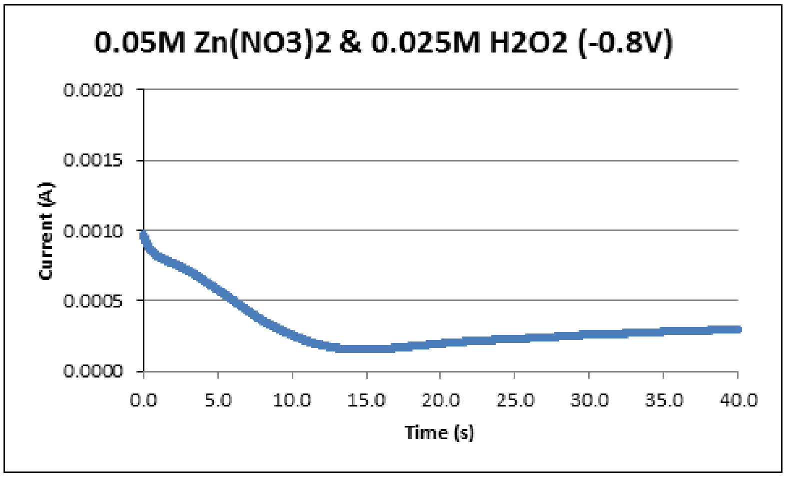

Figure 46: Current vs. time graph when using the 0.05M $Zn(NO_3)_2$ and 0.025M H_2O_2 Solution for electrodeposition with an applied voltage of -0.8V.

6.2.6: 0.05M $Zn(NO_3)_2$, 0.025M H_2O_2 and 0.05M NaCl Solution

Based on our second hypothesis, we designed an experiment to better understand the role of chloride ions in the electrodeposition of ZnO. In Figure 47, the density of the structures has significantly increased compared to the structures deposited without the NaCl using the same concentration (0.05M) of $Zn(NO_3)_2$ and at the same constant voltage (-1.1V) as in section 6.2.3. This was shown at all electrodeposition times (10-40 s) with the use of a solution of 0.05M $Zn(NO_3)_2$, 0.025M H_2O_2, and 0.05M NaCl. At 10s, 690 structures are visible in the image region with an average diameter of approximately 200 nm. The coverage of these structures comprises of 28% of the total image area. At 20s, the structure average diameter increases by 50 nm giving the average structure 250 nm. The number of structures present was similar to the number observed at 10 s with about 652 structures observed. However, this increase in size increased the coverage to 40% of the total area. At 30s, the amount of particles and the average diameter increased to 735 and 275 nm respectively. This small increase led to a coverage increase to 46% of the total. At 40 s, a considerable increase in coverage was displayed with approximately 96% of the total area being covered by the ZnO structures. The average diameter and amount of particles could not be calculated with the image j software because the thin film has formed spatially unresolved structures so this count would be inaccurate. However, an estimated diameter can be given by observation of the 40 s tilted sample. The structures are more faceted then those formed in section 6.2.3

(0.05M of $Zn(NO_3)_2$ and $0.025MH_2O_2$) and an approximate diameter of only 200 nm can be seen. Further fine-tuning of the NaCl and $Zn(NO_3)_2$ concentrations is needed in order to achieve proper periodicity for these self-assembled moth-eye arrays. Future work will consist of optimizing the 4:1 aspect ratio with regards to the height of these structures; the details of these proposed experiments are presented in the future work section of Chapter 7.

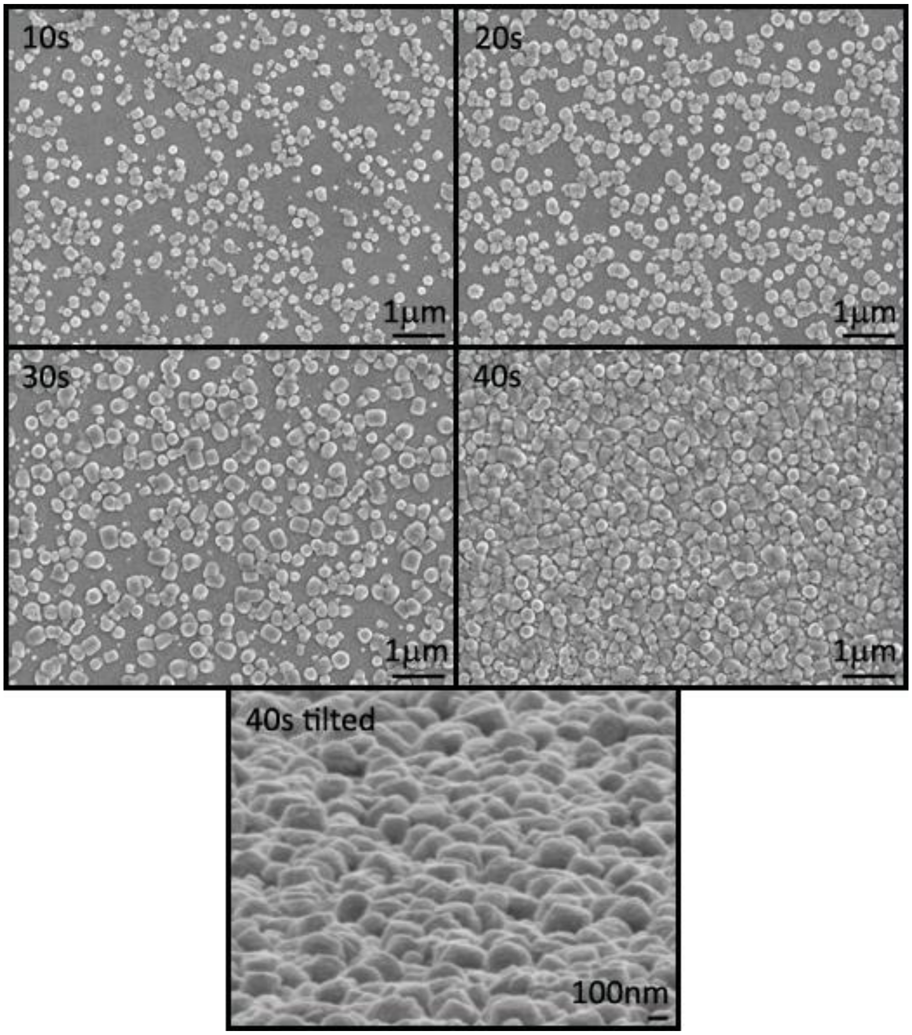

Electrodeposited Samples using 0.05M $Zn(NO_3)_2$ & 0.025M H_2O_2 & 0.05M NaCl Solution				
Deposition	10s	20s	30s	40s
# of Particles	690	652	735	N/A
Average Diameter (nm)	202	255	275	N/A
Fraction of Area Covered (%)	28	40	46	96

Figure 47: Time Evolution studies for electrodeposition using 0.05M $Zn(NO_3)_2$, 0.05M NaCl, and 0.025M H_2O_2 Solution at -1.1V, and 65^oC. (Top) Top-view SEM micrographs at different time intervals with magnified 40s sample that was tilted to 80^0. (Bottom) A table summarizing the number of particles, average diameter and the percetage of area covered in the image for each deposition.

The I-t curve in Figure 48 represents the electrodeposition current response for these faceted hemispherical structures deposited in Figure 47 with the addition of NaCl. It can be seen that the initial current sharply drops to a local minimum at 5s. Then there is a rapid linear increase in current to a maximum and then a gradual decline starts at 14s.

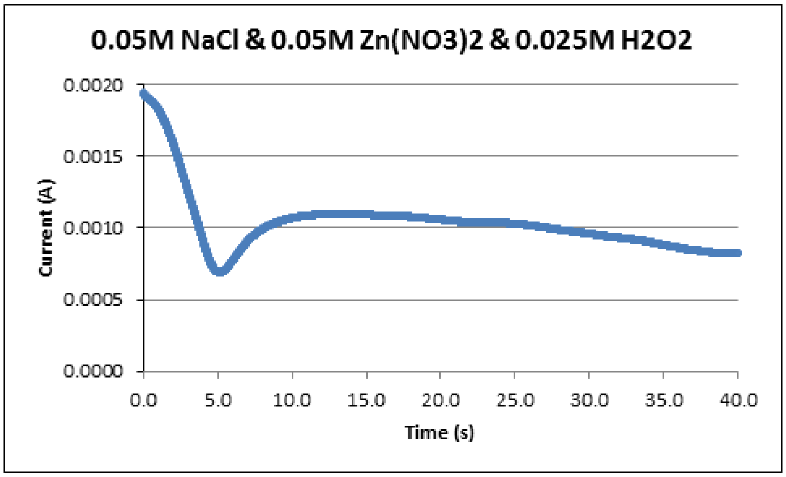

Figure 48: Current vs. time graph when using the 0.05M $Zn(NO_3)_2$, 0.05M NaCl and 0.025M H_2O_2 Solution for electrodeposition.

6.2.7 Sodium Chloride as an Additive to the Solution

The effect of NaCl concentration was experimentally tested by incrementally increasing the concentration as shown in Figure 49. By increasing the amount of chloride ions in the solution we are increasing the ionic strength of the solution which would increase conductivity. The first graph in Figure 49 represents the deposition using 0.05M $Zn(NO_3)_2$ and 0.025M H_2O_2 solution with an applied potential of -1.1V at 65°C. The initial current decrease lasts about 20s and then there is a linear increase for about 45s and then a level off at 1 mA.

The structures formed from this deposition were the hemispherical structures with a diameter of 700 nm approximately. The next sample had the addition of 0.005M of NaCl with all the same deposition parameters. The initial current decrease went to a local minimum at 5s and the current increase occurred over a longer time of about 25s. Then the leveling off of current occurred at 1.3 mA and the density of the structures increased. By increasing the NaCl concentration further to 0.05M the initial current decrease occurs for less than one second and then a very quick current increase occurs over less than 5s and a local maximum is formed at 1.4 mA, than a slow decrease occurs leveling out at 0.5 mA. In the SEM image, the density has increased once again forming more faceted structures with smaller diameters of approximately 400nm. On the last sample, the concentration of NaCl was increased again to 0.1M and a rapid decrease of current followed by an increase of current was visible, but the current increased to a higher value of 1.6 A and then gradually decreased. The SEM image displayed a larger density of smaller structures of approximately 200 nm. It seems that the higher concentration of NaCl the more dense and smaller the structures periodicity becomes.

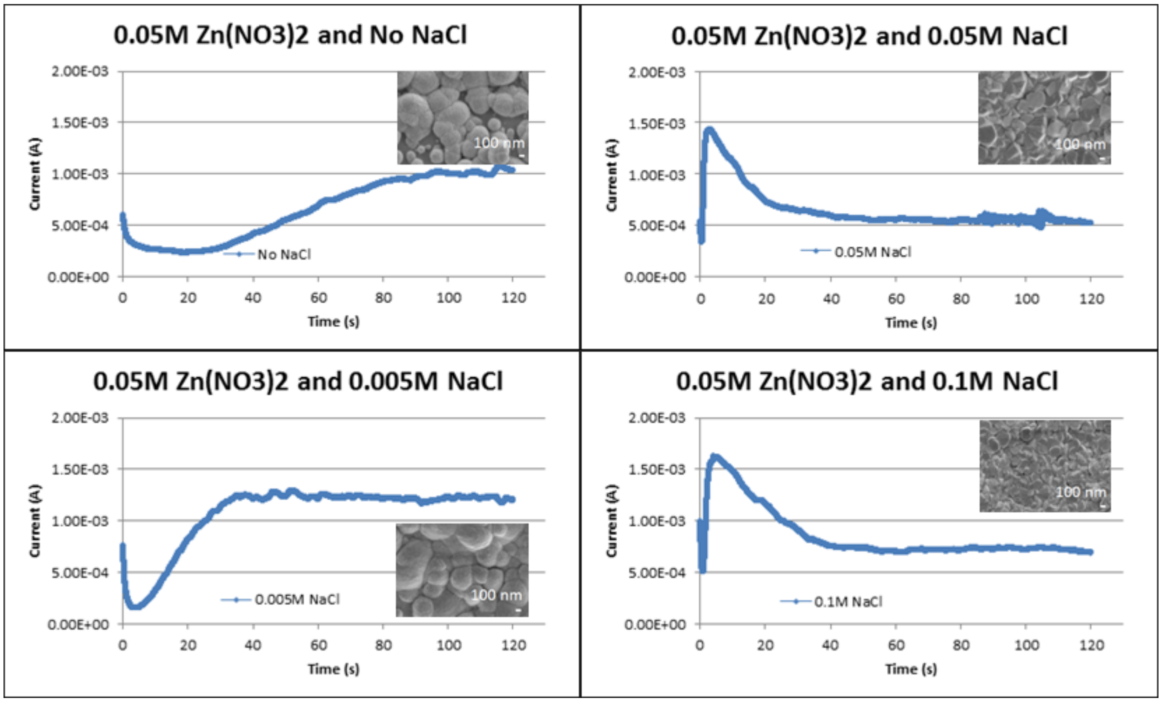

Figure 49: I-t Curves for incrementally increasing NaCl concentration.

Comparing the i-t curves and SEM images from all of section 6.2, we are able to display controllability of the ZnO structure and its dependence of the electrodeposition parameters. This can be completed with deposition times in the range of seconds and not hours which is most promising moving forward with this research.

6.3 Time Evolution Discussion

The growth of nuclei when electrodepositing ZnO can only take place by a faradaic process and the observed current is thus an exact measure of the combined rate of nucleation and growth of the mature nuclei or crystallites.[41] Therefore, one can analyze the different current versus time relationships to understand nucleation and growth. Overall, the ZnO depositions were analyzed and the ability to control and tune the nucleation and growth was studied.

6.3.1 The Effect of Applied Voltage

In sections 6.2.3 and 6.2.5, electrodeposition processes occur with depositing ZnO at -1.1V and -0.8V respectively. The current vs. time relationships for these depositions can also be seen in each section. For all ZnO depositions there is an initial decrease in current that is contributed to the charging of the double layer, then there is a rise in current as the electroactive area increases either by the growth of nuclei or the increase in the number of nuclei formed.[63] Once the curve comes to a maximum it eventually falls off. This is often explained by the formation of depletion or diffusion layers around the growing nuclei. These diffusion layers eventually overlap causing the hemispherical diffusion zones to coalesce to column diffusion zones as seen in Figure 50.[41,63] The nuclei growth and production can be compared between the -1.1V deposited sample and the -0.8V deposited sample.

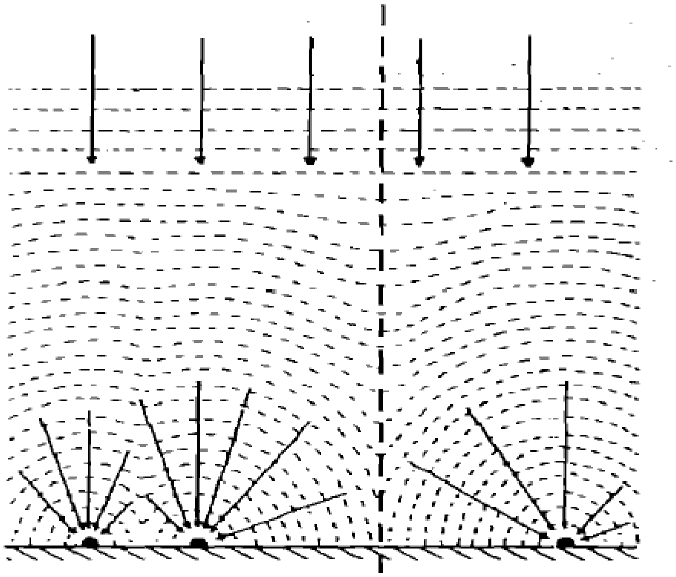

Figure 50: Schematic representation of the growth of diffusion zones and there eventual overlap.[41]

The rate at which these diffusion zones grow is:[41]

$$\delta_t = (kDt)^{1/2} \quad (6.3.1.1)$$

where k is a numerical constant determined by the parameters of the experiment such as concentration, molecular weight and density of material, D is the diffusion coefficient, and t is the time deposited. From this equation, the planar area of the diffusion area can be represented by $S = \pi\delta^2$ since these diffusion zones grow radially around a nuclei.[41] Therefore by using this area for a single nuclei and developing a representation of multiple nuclei the diffusion zone fractional area becomes:[41]

$$\theta_{ex} = N\pi kDt \quad (6.3.1.2)$$

where N is the nuclear number density over the whole area deposited. However, this assumes that no diffusion zones will overlap, which cannot be the case as shown in Figure 51 since the nuclei form randomly of the surface of the electrode. Avarmi theory is used which describes how materials transform from one phase to another.[64] He describes the kinetics in phase change and his number one assumption is that nuclei form randomly so the diffusion zones total area on the surface was defined as:[41,63,64]

$$\theta = 1\text{- } \exp(\theta_{ex}) \qquad (6.3.1.3)$$

From this we can directly relate the reduced amount of current to the fractional area of the diffusion zones formed on the surface of the electrode.

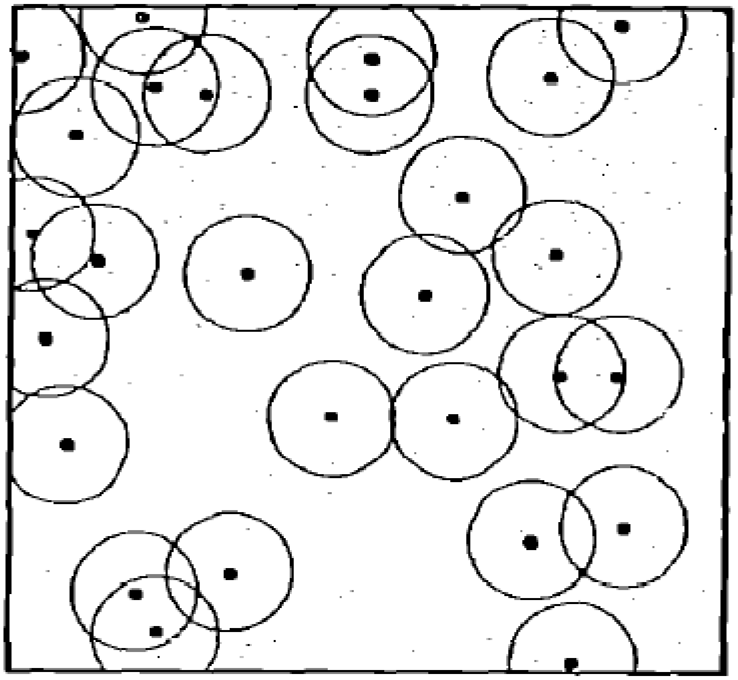

Figure 51: Randomly deposited nuclei (black dots) and their corresponding diffusion zones overlapping with one another.[41,63]

The current in both electrodeposition methods (the one at -1.1V and -0.8V) can be described by this current rate that has been derived and widely used in literature:[41,63]

$$I(t) = zF(2DC)^{3/2}M^{1/2}Nt^{1/2}/\rho^{1/2} \qquad (6.3.1.4)$$

where zF is molar charge of the depositing species, D is the diffusion coefficient, C is the concentration in mol/cm^3, M is the molecular weight, ρ is the density of the nuclei, N is the nuclear number density and t is the time. Nuclear number density is described by the steady state rate of nucleation:[41]

$$N(t) = N_\infty[1- \exp(-AN_\infty t)] \qquad (6.3.1.5)$$

where N is the number of nuclei, t is time deposited and A is the steady state nucleation constant per site. A is a function of overpotential, solution composition, and substrate surface free energy.[41] As A increases, this causes the differential of (6.3.1.5) to approach zero and N to approach N_∞, which is the maximum number of nuclei obtainable under those conditions. However, N_∞ might be thought of as the total number of available sites but experimentally this is controlled by other factors. For instance, for finite values of A, the limit imposed on N becomes the overlapping of diffusion zones.[41] From equation (6.3.1.4), the linear dependence of I on $t^{1/2}$ is widely used in literature[41,63] to study the rate of nucleation and growth processes. In Figure 52, the I vs. $t^{1/2}$ is plotted based on data presented in Figures 42 & 46 for the ZnO structures deposited at -1.1 V and -0.8V.

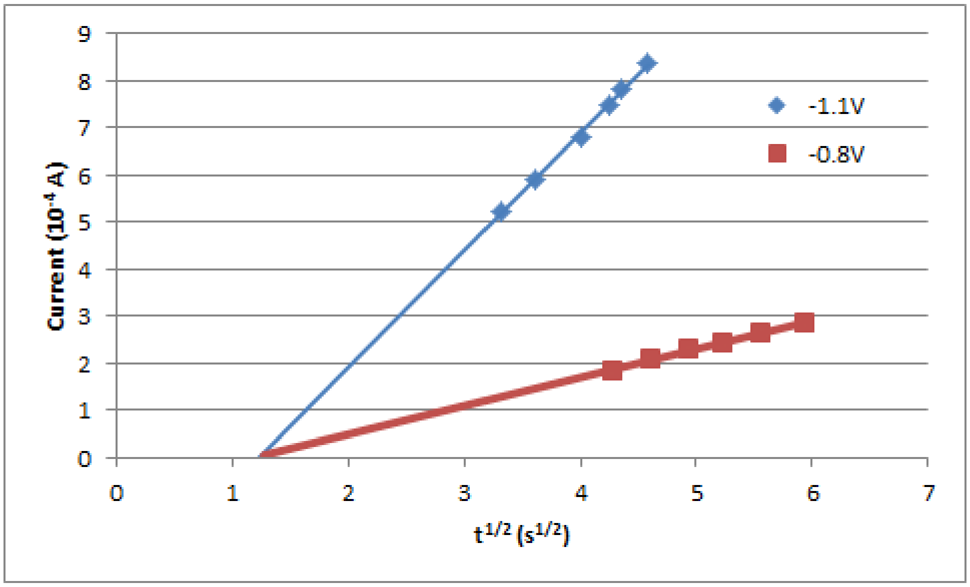

Figure 52: I vs. $t^{1/2}$ plotting the increase in current from the current transients in Section 6.2.3 and 6.2.5. Electrodeposited at -1.1V and -0.8V in a 0.05M $Zn(NO_3)_2$ and 0.025M H_2O_2 solution at 65ºC for 40s.

The linear I versus $t^{1/2}$ shows that the electroactive area increases either by the growth of nuclei or the increase in the number of nuclei formed. Therefore, one is able to see that growth and formation of nuclei is more rapid at the -1.1V when depositing ZnO. These results agree with the SEM characterizations of sections 6.2.3 and 6.2.5 and also agree with the previously published results .[41,63]

After this linear increase in current, we expect to reach a current maximum followed by a current decrease as described above. However, at -1.1V and at -0.8V, these expected current maxima are not seen in the current transients of sections 6.2.3 and 6.2.5. We suspect that during the time scale of the experiment, the structures formed are not yet large enough to create an overlapping depletion layer at the electrode surface.[41] At the -1.1 V, the i-t curve looks like it may be close to reaching a maximum value for current; however, experiments where electrodeposition is carried over for a longer time should be performed.

6.3.2 Effect of Concentration and Salt

In sections 6.2.1- 6.2.4, electrodeposition processes occur with depositing ZnO with different zinc salts and concentrations. In Section 6.2.1 a 0.05M $ZnCl_2$ and 0.025M H_2O_2 solution was used, in section 6.2.2 a 0.005M $ZnCl_2$ and 0.0025M H_2O_2 solution was used, in section 6.2.3 a 0.05M $Zn(NO_3)_2$ and 0.025M H_2O_2 solution was used, and in section 6.2.4 a 0.005M $Zn(NO_3)_2$ and 0.0025M H_2O_2 solution was used. All other parameters were kept constant (-1.1V, 65ºC) and the 40s current transients were observed. The rate of nucleation and growth can once again be extracted by the linear relationship of I vs. $t^{1/2}$ from section 6.3.1 to show how these salts at different concentrations affect the nucleation and growth processes.

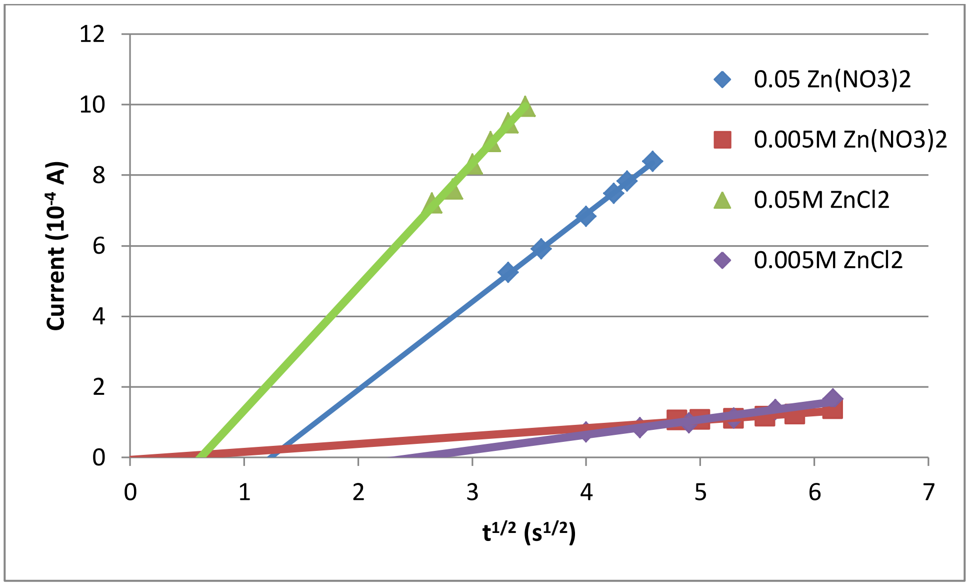

Figure 53: I vs. $t^{1/2}$ plotting the increase in current from the current transients in Section 5.2.3 and 5.2.5. Electrodeposited at -1.1V, 65ºC in a 0.05M $Zn(NO_3)_2$ and 0.025M H_2O_2 solution, 0.005M $Zn(NO_3)_2$ and 0.0025M H_2O_2 solution, 0.05M $ZnCl_2$ and 0.025M H_2O_2 solution, 0.005M $ZnCl_2$ and 0.0025M H_2O_2 solution for 40s.

Both salt concentrations and two different zinc salts used in electrodeposition can be compared in Figure 53. It is seen that by changing the concentration from 0.005M to 0.05M there is a clear increase in the slope of the I versus $t^{1/2}$ curve . This slope is directly related to the increase in the electroactive surface area caused by either the growth of nuclei or the increase in the number of nuclei formed. Therefore, the deposition rate is vastly increased at higher concentration which can also be seen in the SEMs at 20s also. By comparing different zinc salts present at the same concentration, another conclusion can be made: there is an increase in the electroactive surface area when electrodepositing with $ZnCl_2$ instead of $Zn(NO_3)_2$. All of these statements agree with the results seen in the SEM images at 20s displayed in Figures 37 and 41 respectively.

Only one of these ZnO depositions reaches a current maximum in their respective current transients demonstrated in section 6.2.1-4. The electrodeposition conducted with the 0.05M $ZnCl_2$ and H_2O_2 solution showed this maximum, which means that the nuclei on the surface of the electrode have grown large enough and are at close enough spacing's that their diffusion layers are overlapping. This is confirmed by the SEM image of Figure 37 showing the presence of densely packed deposits at 40 s, where the entire substrate looks to be covered. The other electrodeposited samples do not show this current maximum in the duration of the experiment. We expect similar current decreases to be observed when carrying these experiments for longer periods of time.

6.3.3 The Effect of NaCl

In section 6.2.7, four ZnO films were electrodeposited with the addition of NaCl. In this section, a 0.05M $Zn(NO_3)_2$ and 0.025M H_2O_2 solution was used, with the addition a) no NaCl, b) 0.005M NaCl, c) 0.05M NaCl, and d) 0.1M NaCl. All other parameters were kept constant (-1.1V, 65^oC) and the current transients were observed. The rate of nucleation and growth can once again be described by the linear relationship of I vs. $t^{1/2}$ from section 6.3.1.

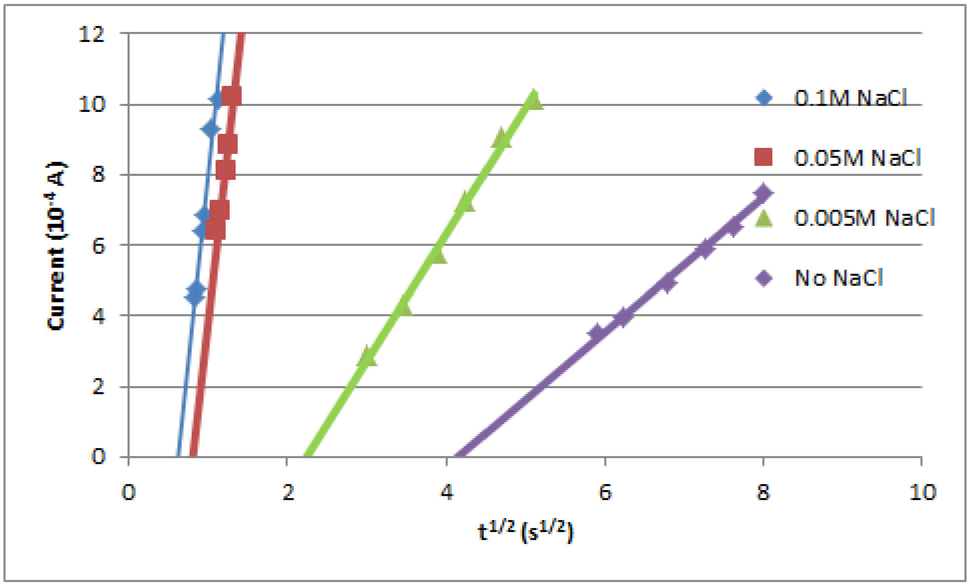

Figure 54: I vs. $t^{1/2}$ plotting the increase in current from the current transients in Section 5.2.7. Electrodeposited at -1.1V, 65°C in a 0.05M $Zn(NO_3)_2$ and 0.025M H_2O_2 solution with the addition to a) No NaCl, b) 0.005M NaCl, c) 0.05M NaCl and d) 0.1M of NaCl. All for samples were electrodeposited for 2mins.

Figure 54 shows the linear increase of current with respect to $t^{1/2}$. As explained in section 6.3.1, the rate of current increase is related to the rate of electroactive surface area increased caused by nucleation and growth. It can be seen in Figure 54 that the increase in NaCl concentration leads to the increase in the rate of current increase and therefore the nucleation and growth rate. Also as one increases the NaCl concentration, the gradual decrease in current after the current maxima is reached occurs at a faster rate (Figure 49). This is due to the larger density of nuclei formed in solutions containing larger concentrations of NaCl leading to the creation of overlapping diffusion zones causing the reduction in current just as explained from theory in section 6.3.1.

By increasing the amount of chloride ions in the solution we are effectively increasing the nucleation and growth rate of these structures. The increase in chloride concentration proves to increase deposition rate creating both more nucleation sites with faceted structures. This is contributed by the increase in reactant concentrations caused by the "salt effect".[44] The multiple nucleation sites and smaller hemispherical structures are just adjoining with their neighboring particle. This shows that the periodicity for a moth-eye array can be achieved, and more optimization is necessary using lower potential with the addition of these chloride ions to reduce the periodicity further. In summary, with the quantitative particle analysis derived from SEM imaging including structure size, density and number of deposited structures, coupled with the transient I-t curve analysis, we are able to understand the role of different electrodeposition parameters including: potential, type of salt, salt concentration, and electrolyte concentration. We can then use these findings to control and tune ZnO structures at the nanoscale which can eventually be optimized to electrodeposit structures for a moth-eye antireflection coating.

6.4: Layered ZnO Deposition

The main focus of this research was to show the control of ZnO electrodeposition. To demonstrate that the methods developed in sections 6.2.1 and 6.2.3 can be combined to create more complex structures; we designed a series of experiments where ZnO deposition was performed on previously electrodeposited layers. Figure 55 depicts a dual layer deposition. A 30s deposition was first completed using the 0.05M $ZnCl_2$ and 0.025M H_2O_2 Solution, followed by time evolution experiments using the 0.05M $Zn(NO_3)_2$ and 0.025M H_2O_2 Solution. This experiment was conducted to test whether using the $Zn(NO_3)_2$ solution could result in the further growth of the existing blade structures, cause the deposition of new blades, or create structures with a spherical morphology. The end result can be seen in Figure 55; the structures formed when electrodepositing in the $Zn(NO_3)_2$ solution formed small spheres between the blade structures. These spherical structures are estimated to be approximately less than 100 nm in diameter. At 10 s, spherical structures deposited by the nitrate solution are just starting to form on the ITO substrate. At 20s, an increase in the density of the spherical structures is seen but the blades are unchanged. At 30s, a further increase in density and an incremental increase in size of about 25 nm to the already existing 100 nm spheres were noted. At 40s the density is further increased and the spherical structures have started forming on the blade tips as seen in the tilted image. These structures are approximately 100 – 150 nm in diameter. It should be noted that based on the 40 s, tilted image, deposition has occurred on the planes of the blade structure having a normal parallel to the substrate.

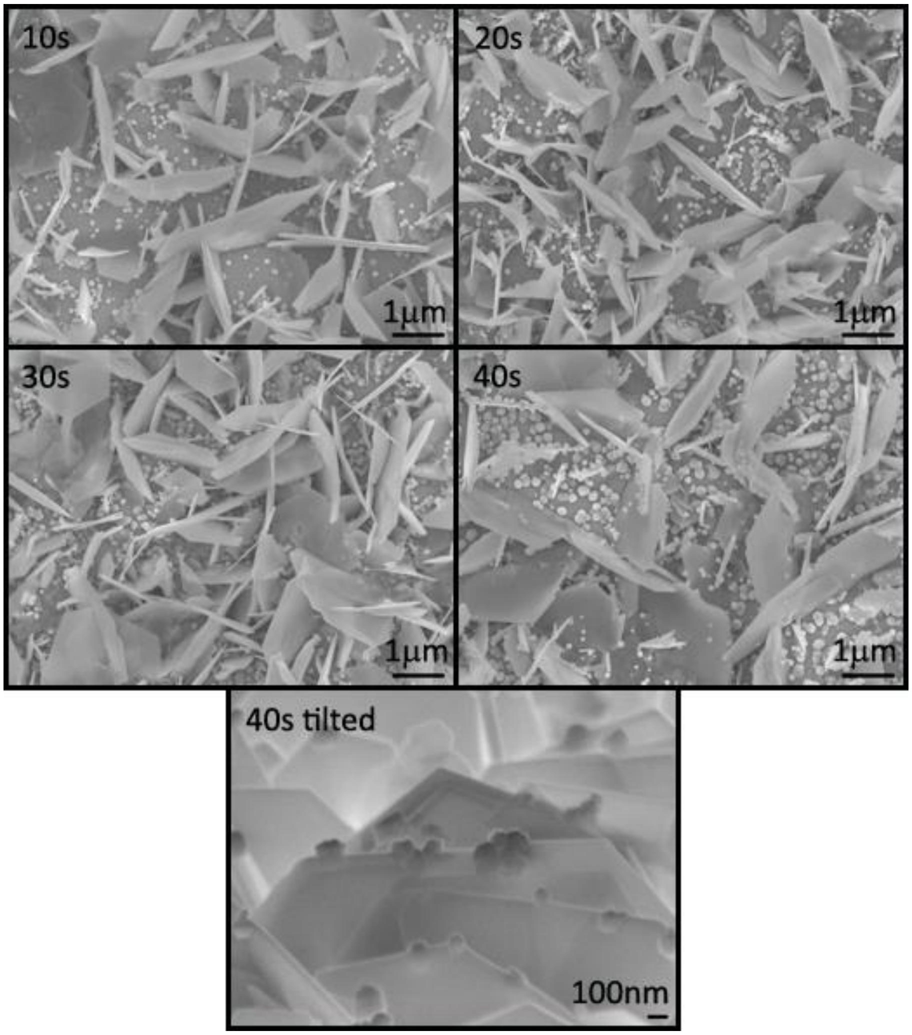

Figure 55: Electrodepositing a 0.05M $ZnCl_2$ and 0.025M H_2O_2 Solution for 30s then time evolution studies at 10 s, 20 s, 30 s, 40 s using 0.05M $Zn(NO_3)_2$, 0.025M and 0.05M H_2O_2 Solution at -1.1 V, and 65ºC with magnified 40s sample that was tilted to 80^0.

The I-t curve in Figure 56 represents the electrodeposition current response for the spherical deposition using the nitrate solution, on a pre-deposited layer of blade structures deposited for 30s with 0.05M $ZnCl_2$, and 0.025M H_2O_2 solution (section 6.2.1). The initial current drop reaches a local minimum at 6s. Then there is a very slow linear increase in current which does not come to a local maximum.

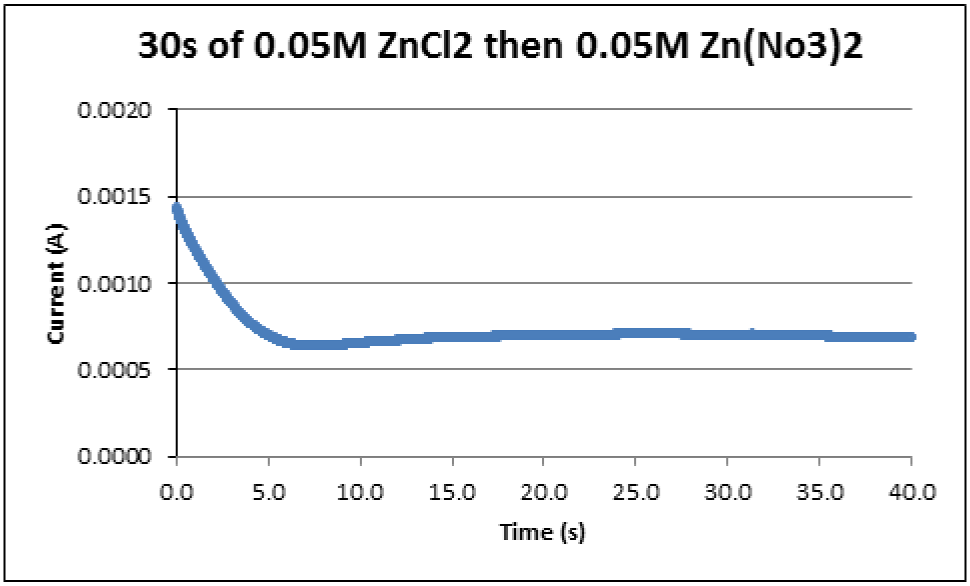

Figure 56: Current vs. time graph when using the 0.05M $Zn(NO_3)_2$,and 0.025M H_2O_2 Solution for a 40s electrodeposition on top of a layer that was deposited with 0.05M $ZnCl_2$,and 0.025M H_2O_2 Solution for 30s.

6.4.1 The Effect of substrate

Electrodepositing ZnO on top of another electrodeposited structure was tested above. This experiment was conducted by first electrodepositing a thin film using the 0.05M $ZnCl_2$ and 0.025M H_2O_2 solution at -1.1V, and 65^oC for 30s then depositing structures on top using the 0.05M $Zn(NO_3)_2$ and 0.025M H_2O_2 solution at -1.1V, and 65^oC for 10s-40s. The goal was to determine whether switching solutions would help the growth of the blade structures rather or form new structures on them. This was completed to see if the structures could be modified further through other means such as layer deposition. However, nucleation was preferred between the blades at first but once at 40s a second growth was observed on the peaks of the blades as well. Therefore, one can conclude that electrodepositing the nitrate solution on the blades does not promote blade growth.

The same theories that went into section 6.3 can be applied here with regards to nucleation and growth of electrodeposited thin films. In figure 57 the I vs. $t^{1/2}$ plots explained in section 6.3 are presented for two depositions: one for the electrodeposition using the 0.05M $Zn(NO_3)_2$ and 0.025M H_2O_2 solution at -1.1V, and 65ºC for 40s on ITO and the other the same exact deposition conditions were carried on the pre-deposited thin film. The current is an exact measure of the combined rate of nucleation and growth of nuclei which is linearly dependent on $t^{1/2}$.[41,63] From Figure 57, the current increases much faster when electrodepositing on the ITO substrate proving that the nucleation and growth of the structures is faster than on the pre-deposited film. From observing the deposition using the $Zn(NO_3)_2$ solution on the pre-deposited film it can be hypothesized that the ITO is more conductive then pre-deposited structures and the ZnO formed from the $Zn(NO_3)_2$ solution prefers growth on the ITO first due to less resistance. However, more research on these types of electrodeposition must be completed to prove this hypothesis. For now this readily displays a decrease in nucleation and growth compared to the same structures grown on ITO.

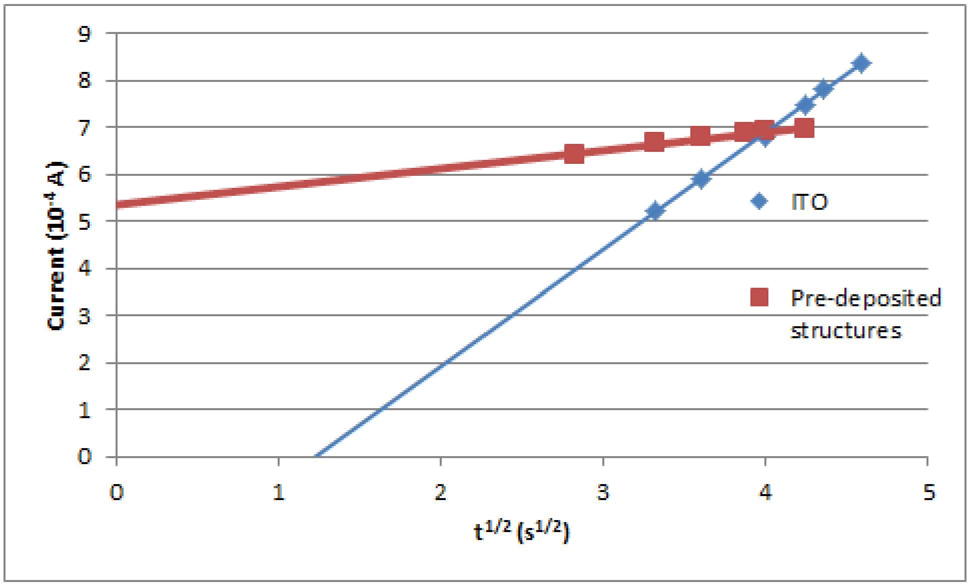

Figure 57: I vs. $t^{1/2}$ plotting the increase in current from the current transients in Section 5.2.3 and 5.4. Samples were electrodeposited at -1.1V, 65ºC in a 0.05M $Zn(NO_3)_2$ and 0.025M H_2O_2 solution on a) ITO or b) pre-deposited structures using a 0.05M $Zn(NO_3)_2$ and 0.025M H_2O_2 solution at -1.1V, 65ºC.

6.5 Composition Analysis

6.5.1 XRD and EDX Results

X-ray diffraction (XRD) and Energy Dispersive X-ray (EDX) spectroscopy were completed on the electrodeposited samples to show that ZnO was the deposited material. The XRD experiments were conducted by the XRD specialist Vicky Jarvis in McMaster's XRD lab. The energy dispersive X-ray spectroscopy was done using the JEOL 7000 scanning electron microscopy system. The results to follow are electrodepositions from four separate solutions. They include 0.05M $Zn(NO_3)_2$ and 0.025M H_2O_2 solution, 0.05 $Zn(NO_3)_2$, 0.05M NaCl and 0.025M H_2O_2 solution, 0.05M $ZnCl_2$ and 0.025M H_2O_2 solution, 0.005M $ZnCl_2$

and 0.0025M H_2O_2 solution. All these experiments were deposited at -1.1V and at 65^{0}C.

0.05M $Zn(NO_3)_2$ and 0.025M H_2O_2

XRD results on the deposition using the 0.05M $Zn(NO_3)_2$ and 0.025M H_2O_2 solution are depicted in Figure 58. The X-ray tube used to complete these results was the cobalt X-ray tube because of availability and its widespread use in crystallography. The observed ZnO peaks from left to right are the (100), (002), (101), (102) and (110). This can be confirmed with the EDX measurement in Figure 59. The zinc and oxygen are the strongest peaks, however due to the penetration of the electrons into the underlying ITO-coated glass substrate, additional peaks corresponding to the elements present in these substrate layers are also observed.

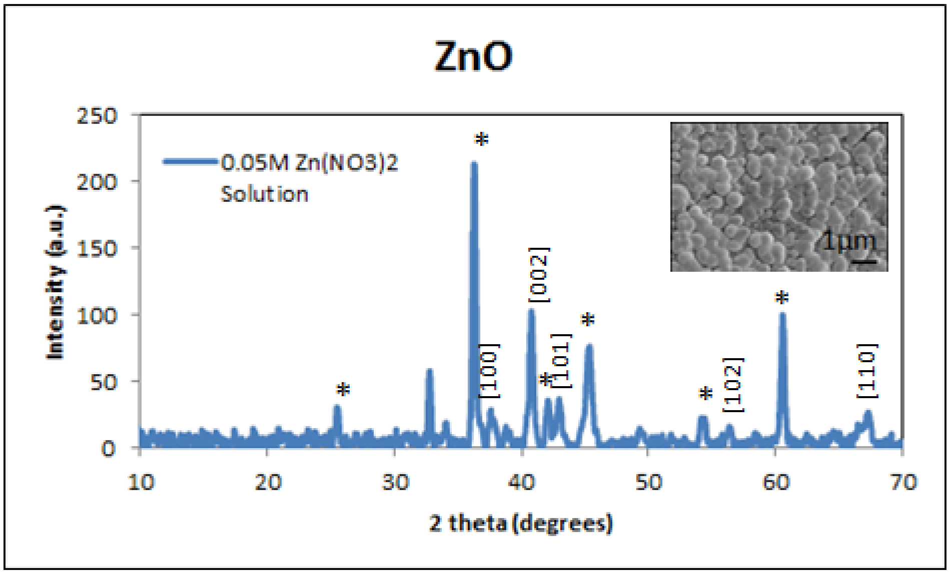

Figure 58: XRD analysis of thin film deposited with 0.05M $Zn(NO_3)_2$ and 0.025M H_2O_2 solution. * indicate peaks for ITO.

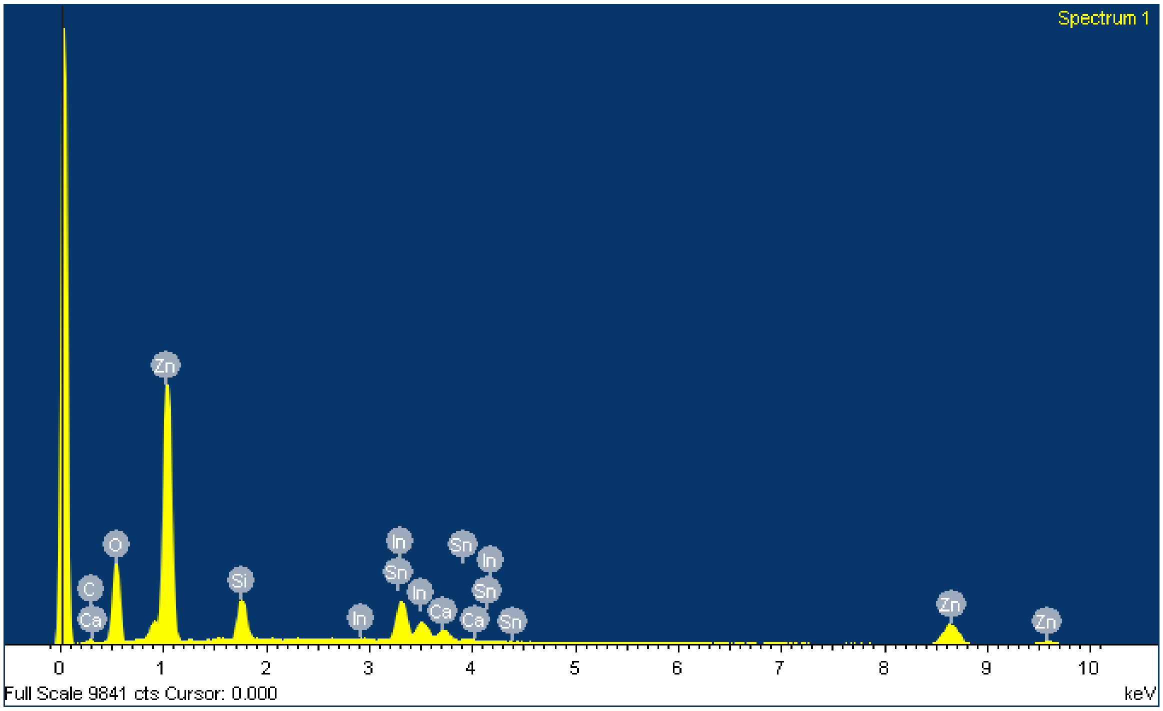

Figure 59: Energy dispersive x-ray results of the thin film deposited with the 0.05M $Zn(NO_3)_2$ and 0.025M H_2O_2 solution.

0.05M $Zn(NO_3)_2$, 0.05M NaCl and 0.025M H_2O_2

XRD analysis was then conducted using the 0.05M $Zn(NO_3)_2$, 0.05M NaCl and 0.025M H_2O_2 solution for electrodeposition. The same peaks are visible (Figure 60) which indicates that ZnO was successfully deposited; however note the 2 theta shift this causes another small ZnO peak to be displayed which would normally be past 70° the (103) peak. This shift occurred due to the use of a copper X-ray tube as opposed to the cobalt tube. This was due to maintenance issues and the unavailability of the cobalt tube. Other peaks were also found that were not attributed to ITO or ZnO. A small amount of silver paste from prior SEM analysis was mistakenly caught in the beam and was fitted to silver peaks in the database.

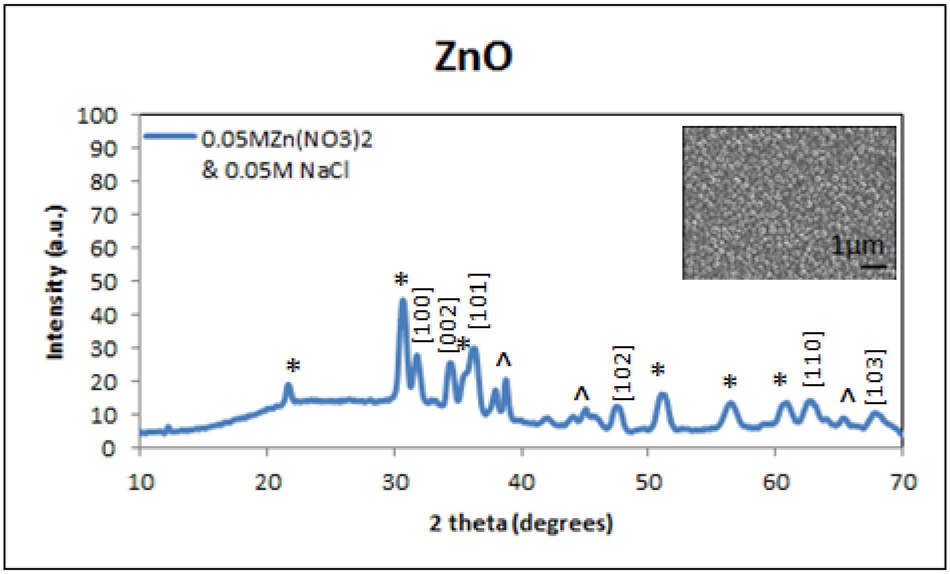

Figure 60: XRD analysis of thin film deposited with 0.05M $Zn(NO_3)_2$, 0.05M NaCl and 0.025M H_2O_2 solution.* indicate peaks for ITO, ^ indicate peaks of silver paste used.

0.05M $ZnCl_2$ and 0.025M H_2O_2

XRD results for the deposited sample in 0.05M $ZnCl_2$ and 0.025M H_2O_2 solution are depicted in Figure 61. In this sample ZnO has formed but it is not the predominate material deposited. All the peaks that are not labelled correspond to a different material which is zinc oxychloride or simonkolleite. It was previously observed that when using high concentrations of $ZnCl_2$ (above 10^{-2}M) zinc oxychloride is formed.[46] When using high concentrations, complex ions in the form of $ZnCl_2^-$ form causing complex structures to form on the surface such as $Zn_5(OH)_{12}Cl_2$ (Zinc oxychloride). As zinc oxychloride has a different preferred orientation than ZnO, this results in the formation of blade structures. These differences in structure can be seen when depositing in a solution with the $ZnCl_2$ concentration less than 10^{-2}M, which is shown in Figure 39 (section 6.2.2). EDX results can also be seen in Figure 62 for the 0.05M $ZnCl_2$ and 0.025M H_2O_2 solution. This confirms the XRD results collected were accurate, as chlorine is present in the thin film, unlike the EDX results collected when depositing in a solution of 0.05M$Zn(NO_3)_2$ solution above.

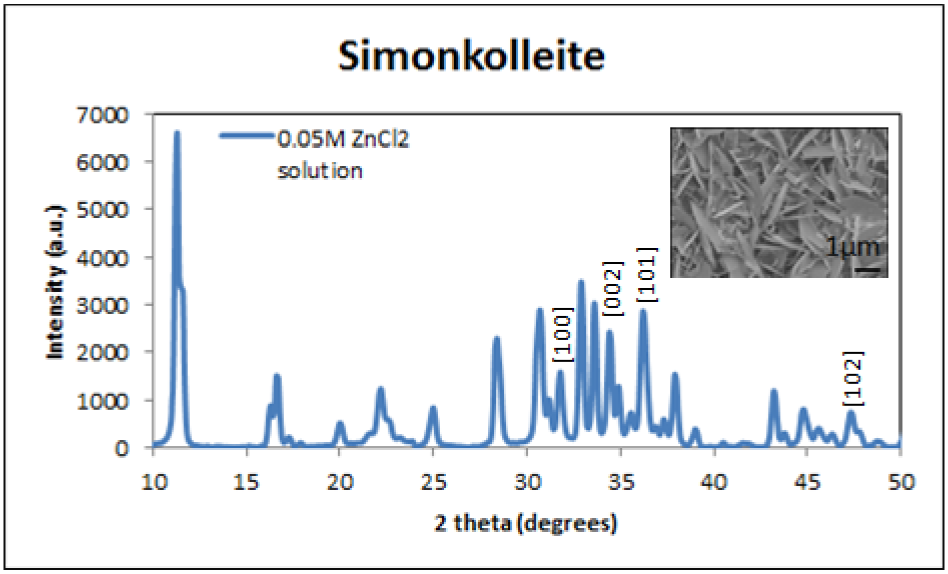

Figure 61: XRD analysis of thin film deposited with 0.05M $ZnCl_2$ and 0.025M H_2O_2 solution. All unmarked peaks are for simonkolleite.

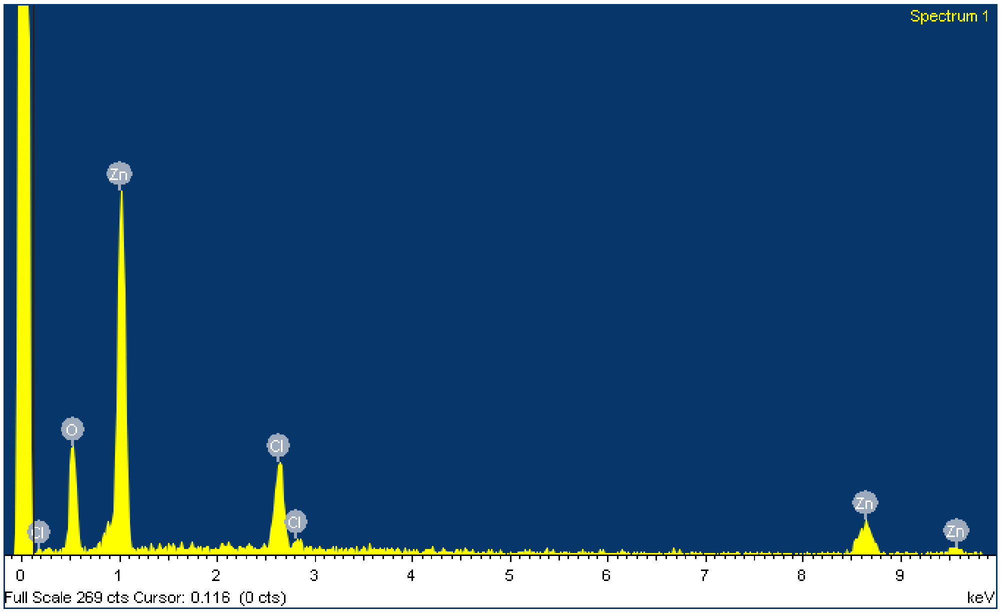

Figure 62: Energy Dispersive X-ray results of thin film deposited with 0.05M $ZnCl_2$ and 0.025M H_2O_2 solution.

0.005M $ZnCl_2$ and 0.0025M H_2O_2 solution

XRD results for a deposited film with a 0.005M $ZnCl_2$ and 0.0025M H_2O_2 solution are shown in Figure 63. Using a lower concentration $ZnCl_2$ results in a lower density thin film, and there is no indication of zinc oxychloride. ZnO peaks can be identified however at (100), (002), (101), (102), and (110). Once again the ITO is labelled with stars.

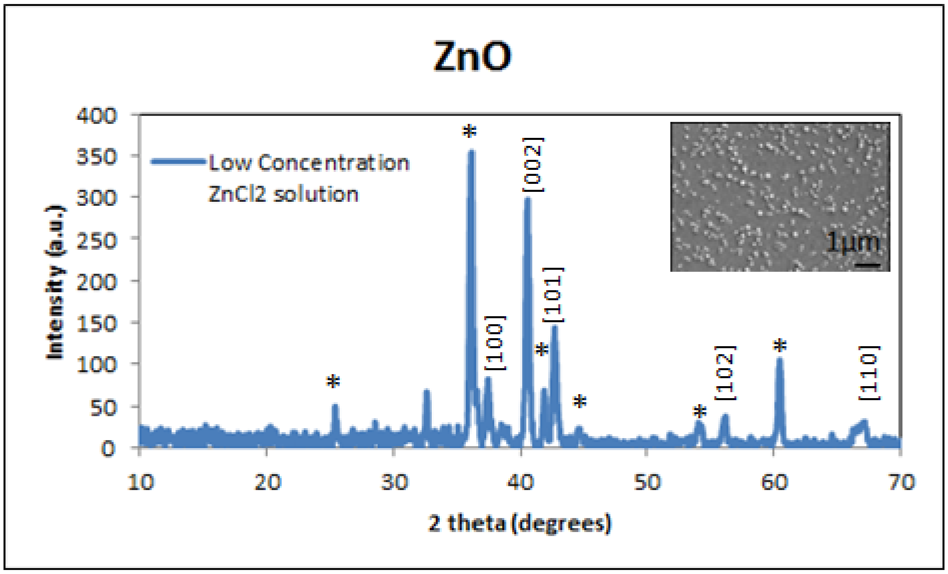

Figure 63: XRD analysis of thin film deposited with 0.005M $ZnCl_2$ and 0.0025M H_2O_2 solution.* indicate ITO peaks.

6.5.2 XRD and EDX Discussion

The above x-ray data concludes that ZnO (and zinc oxychloride on that one exception) is indeed forming on the surface of the ITO. Adding NaCl to solution increases the structure density while effectively decreasing structure size with no visible evidence of chloride being deposited. When using a high concentration (0.05M) $ZnCl_2$ solution for deposition, zinc oxychloride is the main material formed on the electrode but there are trace amounts of ZnO as well. This deposition using different $ZnCl_2$ salt concentrations was researched by Peulon et al[46] and it was concluded that the formation of complex ions such as $ZnCl_2^-$ present at these high concentrations resulted in the formation of Zinc oxychloride. More research is needed to study the solutions containing $ZnCl_2$ salts. Spectroscopy techniques may help in understanding the presence of these complex ions; however this was not the focus of this research. At low concentration, ZnO was formed, which is in accordance with Peulon's work.

6.6 UV-Vis Spectroscopy Results

6.6.1 Results

The ZnO thin films were also optically characterized through UV-Vis spectroscopy. UV-Vis spectroscopy was completed on ZnO structures deposited in a 0.05M $Zn(NO_3)_2$ and 0.025M H_2O_2 solution, at -1.1V, 65ºC, and 40s deposition time. Therefore, transmission results for 3 identical samples were completed and an average transmission was calculated.

In Figure 64, the first graph shows the transmission vs. wavelength for 3 identical 40s depositions. In 40s-1, there was a gradual decrease in transmission from 85% (in the IR) as the wavelength decreased all the way till approximately 375 nm then a sharp decrease was displayed and leveled off at 10% transmission in the UV. In 40s-2, another gradual decrease was observed from above 90% transmission in the IR. The gradual decrease occurred all the way till a wavelength of 380 nm and then another sharp decrease all the way until it leveled off just above 40% in the UV. In 40s-3, The gradual decrease occurred all the way till a wavelength of 385 nm and then another sharp decrease all the way until it leveled off just above 40% in the UV as the last sample. The second graph in Figure 64 represents the average transmission values over the specific wavelength range. In this averaged curve, the transmission starts off at just under 90% approximately and decreases gradually to a wavelength of 380 nm and then another sharp decrease is displayed to level off just above a transmission of 30%

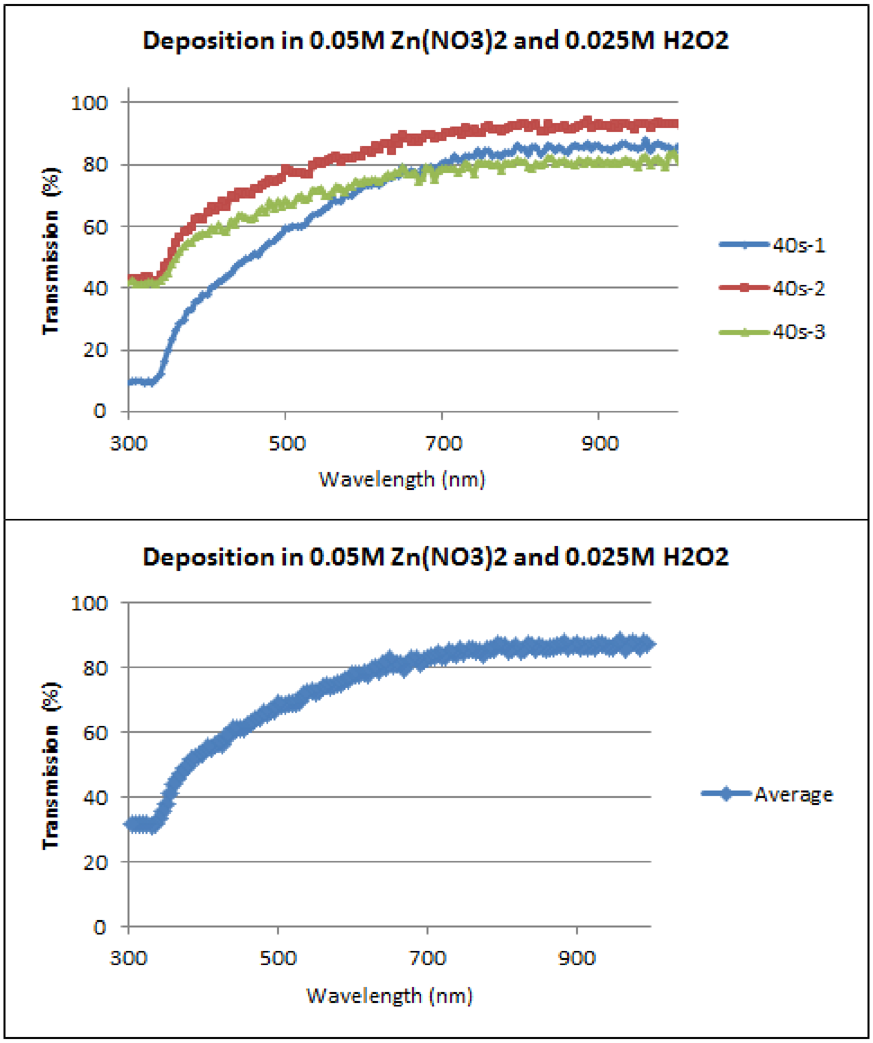

Figure 64: Transmission values for electrodeposited ZnO on ITO with an applied potential of -1.1V, at 65°C in a 0.05M $Zn(NO_3)_2$ and 0.025M H_2O_2 solution

6.6.2 Discussion

The transmission values for the electrodeposited ZnO show the ability to transmit light through this optical coating. However, large device to device variation is observed with these preliminary results and further optimization is required to more accurately control the experimental conditions and the deposition results. All the samples deposited at -1.1V, 65ºC in a solution of 0.05M $Zn(NO_3)_2$ and 0.025M H_2O_2 for 40 seconds displayed a sharp drop in transmission at an average value of 380 nm. This transmission is a result of ZnO's band gap energy.[42]

$$E = hc/\lambda$$

where h is the Planck's constant, c is the speed of light, and λ is the corresponding wavelength. Therefore, we can calculate the band gap for our electrodeposited thin film. The band gap energy for the average wavelength of the three 40s samples is 3.27 eV. The known average band gap for ZnO is 3.3 eV so our experimental value is very close to the known value from literature.[42] Further optimization of the ZnO thin film needs to be conducted to improve the reproducibility and to increase the transmission in the visible range.

6.7: Electrodeposition on Silicon

6.7.1 Results

ZnO electrodeposition was also completed on silicon to show that multiple substrates can to demonstrate that these anti-reflection coatings can be directly deposited on highly reflective (>30% reflectivity) semiconductors. Figure 65 a, b, and c demonstrate electrodepositions carried at 65ºC, at -1.1V, in a solution of 0.05M $Zn(NO_3)_2$ and 0.025M H_2O_2. The voltages, solution compositions, and temperatures were kept identical to the experiments performed on ITO substrates to study the effect of the substrate. Even though the same parameters were used, a visible change can be depicted comparing the results is section 6.2.3 (all deposition parameters the same except substrate) in Figure 65. In a) the deposition occurred for 2 minutes and in this time circular/oval structures formed with an average diameter of approximately 120 nm. The total amount of particles formed was 704 which made up 18% of the total area. In b) the structures grew in size to an average diameter of 165 nm and the coverage of the deposited area was increased to 22% of the total area, with the presence of 450 deposited structures. In c) pulsed deposition was completed, where two 2 minute pulses were applied. The deposited structures seem to have the same approximate size but this could not be confirmed with the image j software because the formation of spatially unresolved structures. However, the coverage of the film was still calculated to be about 46% of the total area which shows a great increase in the surface coverage compared to b) which was deposited at a constant voltage.

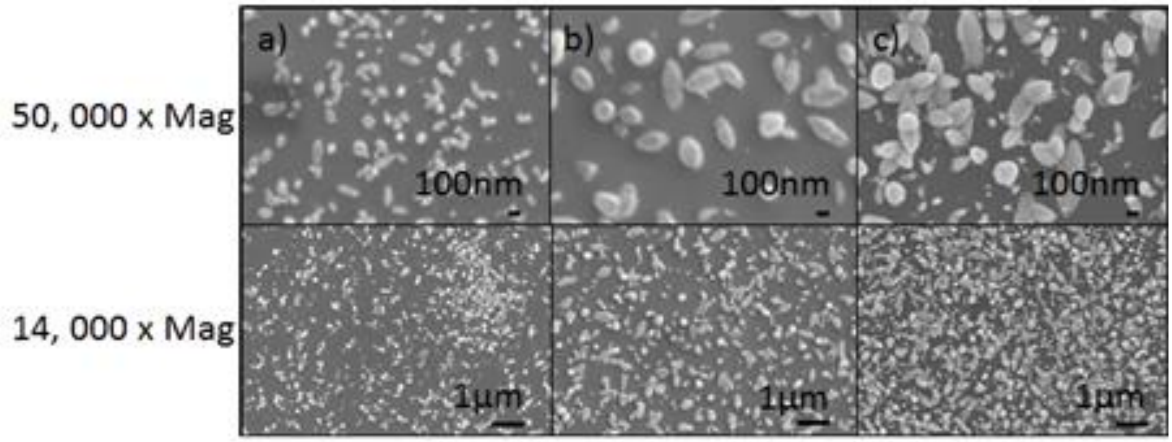

Electrodeposited Samples using 0.05M $Zn(NO_3)_2$ & 0.025M H_2O_2 Solution			
Deposition	a)	b)	c)
# of Particles	704	450	N/A
Average Diameter (nm)	120	165	N/A
Fraction of Area Covered (%)	19	22	46

Figure 65: ZnO electrodeposition on silicon at -1.1V, 65^{0}C, in a solution of 0.05M $Zn(NO_3)_2$ and 0.025M H_2O_2. (Top) Top-view SEM micrographs at different time intervals a) 2 mins, b) 4 mins, c) 2mins→ 20s off→ 2mins (Bottom) A table summarizing the number of particles, average diameter and the percentage of area covered in the image for each deposition at 14,000x magnification.

An i-t curve was examined for the deposition of ZnO on silicon for comparison with depositions performed under the same conditions on ITO in section 6.2.3. This deposition was performed for a duration six times longer than in case of ITO which lasted for 40 seconds. In figure 66 it is noticed that it took much longer to charge the electrical double layer, the local min value was at approximately 50s and the increase in current is still occurring at a very slow rate even nearing 240s (4 mins).

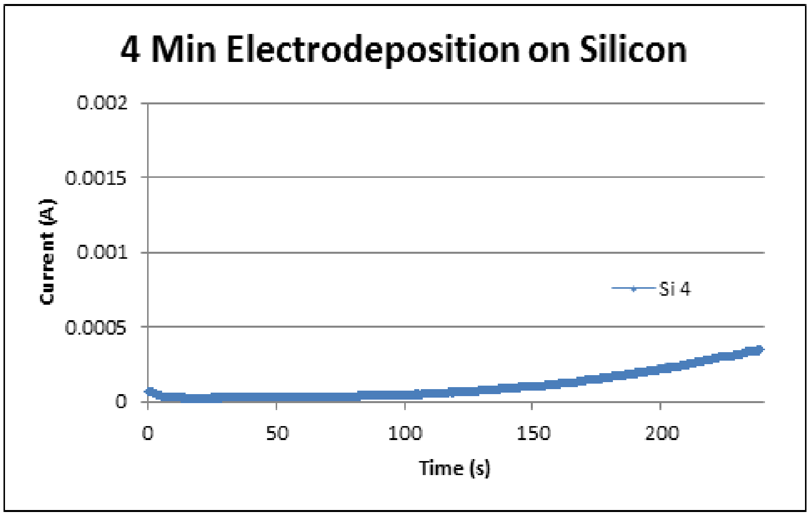

Figure 66: Current vs. time graph for ZnO deposited on silicon with a time of 4mins, applied voltage of -1.1V and at a temperature of 65°C.

6.7.2 Discussion

Silicon is a semiconductor who's conductivity is low in comparison to the ITO semiconductor substrate, so a drop in overall current was observed when comparing the I-t curves in section 6.2.3 and that in figure 66. When comparing SEM micrographs resulting from a constant potential deposition (Figure 65b) and a pulsed potential deposition of the same duration (Figure 65c), it is noted that there is an increase in particle density with the application of the pulsed potential. In electrodeposition there are three surface processes that contribute to increased nucleation and growth on the surface. These consist of population of adatoms, and the overpotential. This can occur either from the formation of a new nuclei or the buildup of existing crystals. In pulsed deposition there is an increase in the population of adatoms on the surface, compared to constant potential deposition.[36] This increase leads to the increased nucleation rate depicted in Figure 65 c). The control of nucleation in electrodeposition is the main objective when trying to self-assemble structures with a certain periodicity. Therefore, tuning the nucleation rate was the focus of ZnO electrodeposition presented in section 6.3. The ability to control this characteristic could aid in the development of devices for many optical applications.

6.8 Optical Characterization of ZnO on Silicon Substrate

6.8.1 Results

Up to this point optical characterization was conducted on films with an ITO substrate. The following section will describe the anti-reflective properties of ZnO on silicon. Reflection measurements were conducted at our industrial partner's lab in the Toronto area. To test the reflectance of the ZnO-coated silicon samples, reflection measurements were performed; the ZnO thin films were placed in a pivoting holder so reflection measurements could be conducted at multiple angles. The angles used were at 10º intervals from 10º - 70º for each sample.

The samples used for these reflection measurements were deposited on [100] silicon. The substrate was prepared using methods described in Appendix A, then put into a solution containing 0.05M $Zn(NO_3)_2$ and 0.025M H_2O_2. ZnO was deposited with a voltage of -1.1V at 65ºC. Three samples were tested, each with a different deposition time as demonstrated in the SEM micrographs of Figure 65 in section 6.6. Table 2 summarizes the preparation method of samples used in the following optical measurements.

Samples	Electrodeposition Time	Method
a) Si 5	2mins	Constant Voltage
b) Si 4	4mins	Constant Voltage
c) Si 10	2mins→20s off→2mins	Pulsed Voltage

Table 2: Silicon electrodeposition times and methods.

Reflection data is presented in two ways. In Figure 67, the reflectance is plotted versus wavelength at every angle the sample was positioned with respect to the incoming beam. In Figure 68, the reflectance is plotted versus angle of incidence at fixed wavelengths of 400nm, 600nm, and 1000nm.

In Figure 67, the reflection results for all three samples as well as for a plain piece of silicon substrate are displayed at 7 different angles from 10º-70º. The plain piece of silicon has a reflectance greater than 35% in the UV, visible, and infrared range, while all deposited thin film samples' reflectance are much lower. The Si 5 sample showed the strongest reflection of the three. In the visible range it displayed a 20% decrease in in reflection compared to bare silicon. As the wavelength increased this reflection difference became smaller until it reaches the reflectance value of bare silicon in the IR. Si 4 on the other hand displayed good antireflective properties by showing less than 5% reflectance all the way to approximately 600 nm. At that point the reflectance is increased to 10% until entering the Infrared where it increases to 20%. The Si 10 sample behaves in the similar manor, displaying <10% total reflectance until 600nm where it increases in reflectance to between 10% and 20% in the IR.

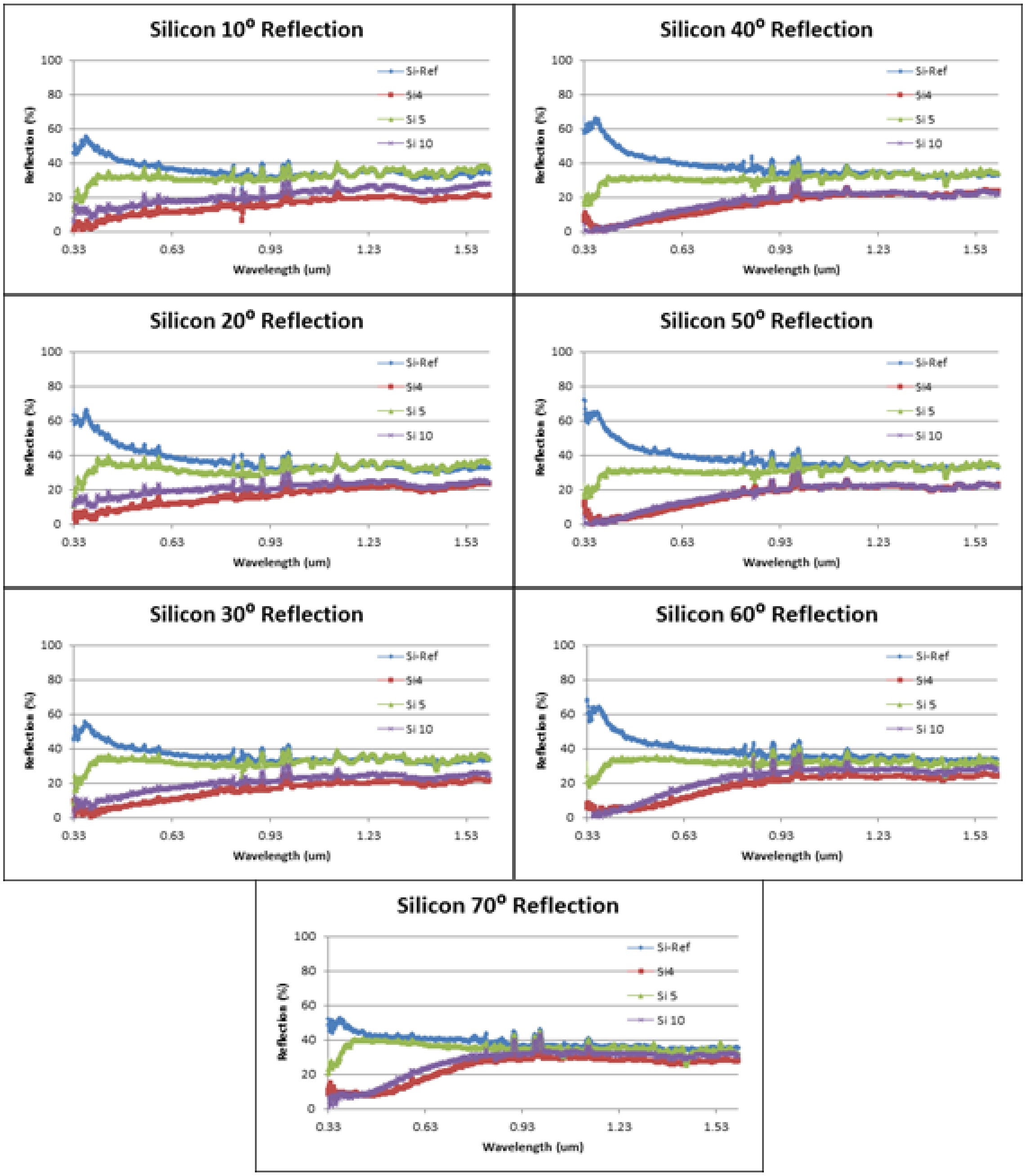

Figure 67: Seven different angles of reflection vs. wavelength results collected for ZnO deposited on silicon.

The results shown in Figure 68 depict the relationship between the reflection of light vs. the angle of incoming light. These results show the difference between the silicon reference sample and the ZnO deposited samples. At a wavelength of 400 nm Si5 is steady at 30% (reflection at all angles), Si 4 is steady at less than 5% for all angles, and Si10 has an increased total reflection at low angles (approx. 10%) but at higher angles its reflection is under 5% . At 600 nm, Si 5's reflection increased to roughly 30%, Si 4's reflection has also increased to a steady value of 10%, and Si10's reflection has also increased by 10% showing the same trend of higher reflection at lower angles. At 1000 nm, Si 5's reflection is approaching that of bare silicon around 35%, Si 4's reflection is just around 20% at all angles and Si 10's is just under 25% at all angle except the last one where an increase to 30% reflection is observed at the 70º tilt.

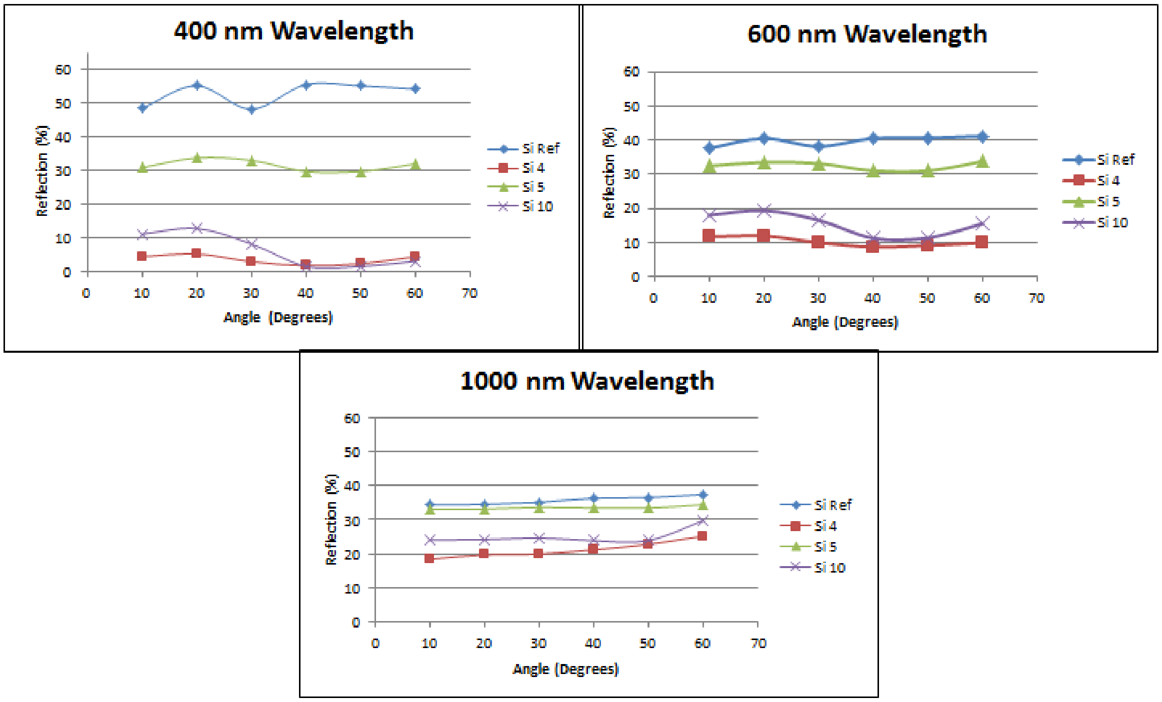

Figure 68: Results for reflection of light vs. angle of incoming light for ZnO films deposited on silicon.

6.8.2 Discussion

These 3 ZnO depositions on silicon show initial promise for reducing the overall amount of reflection but more research is needed to study their transmission properties and reproducibility. Si 4 and Si 10 showed the most promise reducing the amount of reflection to less than 15% on average in the visible range. These decreased reflections are due to the ZnO structure and density; however these structures do not hold the dimensions needed for an optimal moth-eye array. The structures have the desired lateral dimension, while their heights do not provide the 4:1 aspect ratio needed for optimal anti-reflective properties. This can also be shown in the data as the wavelength moves into the IR, the reflection increases in all samples. In spite of this, the initial goal was achieved which was to show that this ZnO thin film does reduce the reflection on a silicon substrate.

6.9 Patterning of Electrodeposited ZnO

In order to engineer materials that are controllable in the micro/nanoscale for achieving specific optical properties such absorption, reflection and photoluminescence , which are additionally tunable in the micro/millimetre length scale for effective electrical biasing and contact, a new fabrication method was created based on top-down and bottom-up fabrication and patterning of semiconductive materials. The electrodeposition process used in both methods described below was performed at a potential of -1.1V at 65°C for 2 minutes with the same procedure described in Appendix A. The solution consisted of 0.05M $Zn(NO_3)_2$ and 0.025M H_2O_2. The substrate used was ITO fabricated using the methods described in Appendix A. Figure 69 shows the schematics describing the fabrication and photolithography processes used for patterning ZnO.

The Top-down + bottom-up method (a) was performed by first patterning the ITO substrate using photolithography (full procedure in Appendix A), followed by electrodeposition of ZnO. In the bottom up + top-down method (b) ZnO deposition was performed first, forming a thin film that was then patterned with photolithography and etching (full procedure in Appendix A).

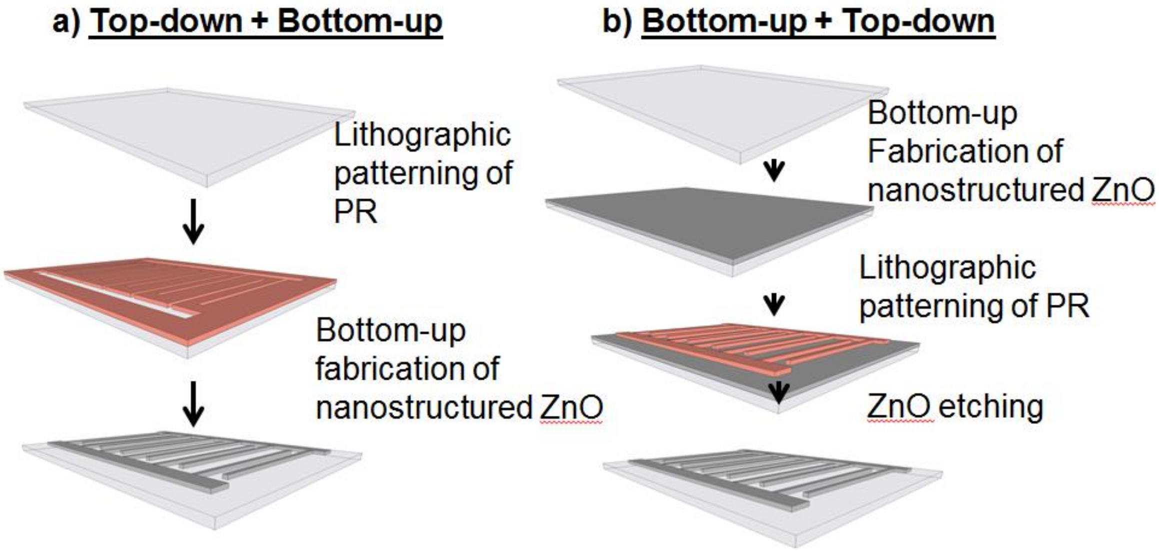

Figure 69: ZnO patterning fabrication a) top-down + bottom-up, b) bottom-up + top-down.

Figure 70 shows the SEM images of the patterned ZnO film. ZnO was deposited for two minutes in both cases. The first method a) Top-down + bottom-up demonstrated electrodeposition on a pre-patterned area with rails (40 µm thick) staggered one over the other. It is seen that the deposited area has the overall dimensions and geometry of the utilized photomask, with the addition of a ZnO layer containing spherical structures. This enables one to form structures that have a periodicity of hundreds of nanometers in a template containing microscale features.

Fabrication using the second method of Bottom-up + top-down processing is shown in Figure 69 b. In this case, the ZnO layer was deposited over the entire surface and was then lithographically patterned and etched. It is seen in Figure 70 that although the same photomask was used for both a) and b), the rails in b appear to be have a smaller width. This is due to isotropic wet etching process causing the etching of the ZnO regions under the etch mask. Despite this, it is possible with further optimization and the use of a dry etching process to avoid the overetching of the ZnO lines.

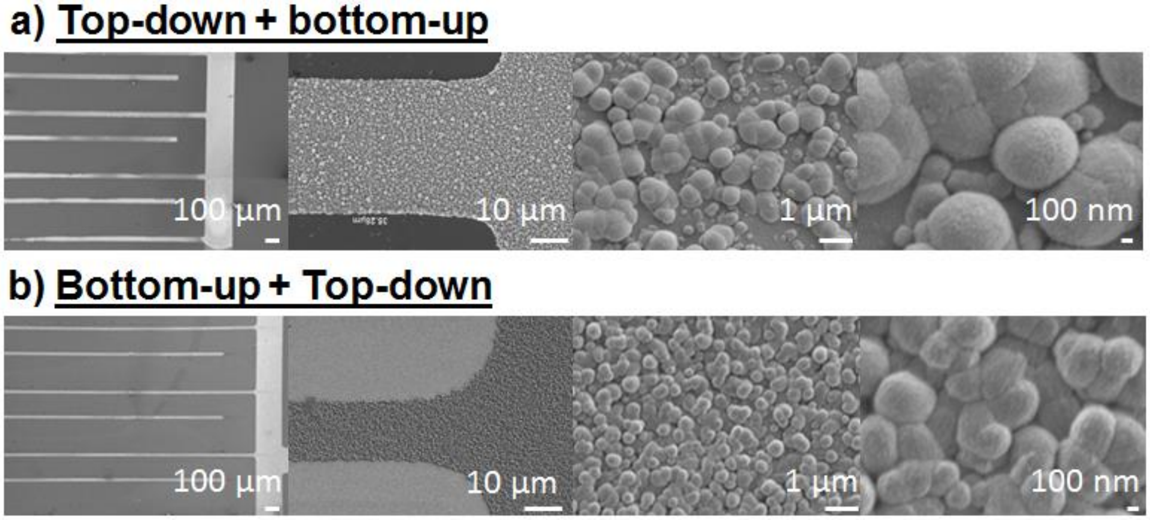
a) Top-down + bottom-up

b) Bottom-up + Top-down

Figure 70: SEM images for ZnO patterning fabrication method a) top-down + bottom-up b) bottom-up + top-down.

From the results above we have successfully patterned ZnO using photolithography techniques. A top-down + bottom-up fabrication method was developed to accurately pattern micron scale rails. This method consisted of patterning using a photo-mask and then electrodepositing ZnO in the patterned areas. The bottom-up + top-down fabrication method was also developed where a thin layer of ZnO was first deposited and then patterned and followed by a wet etch which changed the dimensions of the rails. These photolithography processes could be used in multiple applications such as the formation of a moth-eye array used as an anti-reflection coating for solar cells, UV photodetectors, or dye-sensitized solar cells.

The main conclusions derived from the results and discussions presented in this chapter will be presented in Chapter 7.

Chapter 7: Conclusion and Recommended Future Work

7.1 Concluding Statement

The main objective of this work, as described in detail in Chapter 1, was to fabricate tunable ZnO nanostructures through the process of electrodeposition and to study the role of different deposition parameters such as temperature, overpotential, type and concentration of the reaction precursors, and type of substrate on the morphology, size, and density of the deposited structure. The next set of objectives were to display the tunability and control of the electrodeposited ZnO structures over multiple length scales (nano and micron scales), pattern electrodeposited ZnO using conventional top-down techniques such a photolithography, and tune the optical properties of substrate materials and create anti-reflection coatings with hemispherical protuberances similar to those observed in moth-eyes. In Chapter 2, the theory and background related to anti-reflection coatings were presented and previous work in the area of moth-eye anti-reflection coatings was reviewed. From these findings we were able to see the major drawbacks to single layer coatings and double layer coatings over a broader spectrum. Also we were able to use the previously-performed studies on moth-eye structures to a design a nature-inspired anti-reflection coating for photovoltaic application. The moth-eye array with a height of 400 nm and periodicity of 100 nm would have optimal dimensions for reduction of reflection over a broad range of wavelengths and angles of incidence. In Chapter 3, the electrodeposition technique was discussed in full detail. Both theory and previous literature on ZnO depositions were studied to find a way to create a self-assembled moth-eye array. In Chapter 4, the different equipment and processes used for the fabrication of ZnO arrays were outlined. In Chapter 5, the characterization techniques were explained. Finally, In Chapter 6, the experimental results and analyses were presented and discussed.

Electrodeposition of ZnO thin films was successfully completed under different conditions and was characterized using: scanning electron microscopy, energy dispersive X-ray spectroscopy, X-ray diffraction, and UV-VIS spectroscopy. SEM was used to study the electrodeposited structures and their characteristics including morphology, size and dimensions. EDX was used to identify the elements present and their relative abundance in the material under investigation. XRD was used to confirm the composition of ZnO formed on the surface. UV-VIS was first used to measure the transmittance of these materials and to show that the measured band gap agreed with previously reported values for ZnO. Afterwards, reflection mode UV-VIS spectroscopy was used on highly reflective substrates such a polished silicon and electrodeposited samples. Electrodeposited substrates showed at best, a less than 5% reflectance (at ~660nm), compared to ~40% for silicon.

The effect of multiple electrodeposition parameters including temperature, applied potential, type of zinc salt, concentration of electrodeposition precursors, concentration of additives, and type of substrate on the rate of electrodeposition was studied. Furthermore, the role of these parameters in tuning the size, density and morphology of electrodeposited structures was investigated. As temperature was increased the rate of reaction was also increased and the uniformity of the thin film could be controlled. As the applied potential was varied, we were able to alter the morphology and of the deposited structures and the thickness of the thin film. When using the $ZnCl_2$ salt (section 6.1.2) in the deposition solution, by increasing the voltage (-1.1V→-1.7V) the morphology was altered from blade-like structures to nodular structures combining with each other to form snake-like features. When using the $Zn(NO_3)_2$ salt (section 6.2.3 and 6.2.5) and applying a lower absolute potential (-1.1V→-0.8V) we observed the hemispherical structures deposited at 40s changed in size from an average diameter of 500nm to <200nm. The densities with this voltage change also changed from a deposition at -1.1V covering 95% of the total area, to only 31% of the total area when deposited at -0.8V. As different zinc salts were used the ability to tune the thin film became evident. By changing the salt the deposition rate, the morphology, and the density could all be tuned and controlled. The change in concentration added to the effect of changing morphologies and sizes. The ability to transfer from micron-sized blades to 200 nanometer pyramidal structures was shown when $Zn(NO_3)_2$ salt was used instead of $ZnCl_2$. Also the change from large hemispherical structures (diameter 500nm) to small pyramidal structures (diameter 150nm) was seen as the salt concentration was varied from 0.05 M to 0.005 M. The additives to the solution were experimented with: NaCl was used to increase the nucleation rate rather than promote build-up of existing large particles. This technique ended up creating the periodicity needed for the early stage moth-eye array. By inputting different concentrations of this additive one was able to control the deposition rate, density, structure size and even morphology. More specifically, increased NaCl concentration resulted in the deposition of more faceted structures that were smaller and were developed with a high nucleation rate. From the time evolution results with the additive of 0.05M NaCl (section 6.2.6), the 40s deposition displayed multiple structures closely packed that had an average diameter of roughly 200 nm that covered 96% of the total area under observation. Layered deposition was also completed through the electrodeposition with a solution of $ZnCl_2$ salt first and then $Zn(NO_3)_2$ salt. First, blades were deposited on the surface and then hemisphere structures were deposited after which grew preferentially between the blade structures. The last parameter adjusted was effectively changing the substrate. By changing the substrate from ITO to silicon, the structures were much smaller and formed oval/circular structures compared to using all the same parameters but on ITO. The use of pulsed electrodeposition was conducted on silicon substrates and showed an increase in the density of electrodeposited structures, compared to structures deposited under DC conditions for the same duration.

Top-down methods such as photolithography and etching were combined with bottom-up electrodeposition methods developed in this work to introduce controllability in a broad range of lengthscales ranging from the nanoscale to the microscale. Two fabrication methods were developed; top-down + bottom -up and bottom-up + top-down fabrication. Top-down + bottom-up method consisted of first patterning a spin-coated photoresist using a photo-mask and then electrodepositing ZnO in the patterned areas. The pattern was 40 µm thick rails. The bottom-up + top-down fabrication method was developed by first electrodepositing a thin layer of ZnO and then patterning the deposited layer using lithography followed by a wet etch technique, which etched the ZnO and formed a staggered rail pattern with 10 µm thick rails. The feature sizes of the two developed methods were different due to the isotropic wet etch used for the bottom-up + top-down technique, which could be used for creating smaller features for use in photovoltaics.

Transmission-mode UV-VIS spectroscopy experiments were performed on ZnO films electrodeposited on ITO substrates; whereas reflection-mode measurements were performed on ZnO-coated silicon substrates. The results of transmission mode measurements indicated that the band gap of this material deposited was 3.27 eV which agrees with theoretically previously reporter values for ZnO to (3.20 eV -3.40 eV).[42] The results of reflection mode measurements indicated that – compared to the bare silicon (>35% reflectance) sample – the reflectance of the deposited films were lower (shown to be as low as 5%-10% reflectance in visible range).

In addition to the abovementioned results, XRD and EDX measurements confirmed that the electrodeposited structures were indeed ZnO.

7.2 Future Work

Future work for this project is necessary to achieve the main goal of fabricating a self-assembled moth-eye array. The proposed future work is divided with respect to fabrication and characterization and is summarized below.

7.2.1 Fabrication

The main goal would be to reproducibly electrodeposit structures with a 4:1 aspect ratio so they would have a peak height of 400 nm and a periodicity of 100 nm. Further optimization can be done with different combinations of NaCl concentration in the $Zn(NO_3)_2$ solution at lower overpotentials to perform electrodepositions in the regime controlled by surface kinetics. By electrodepositing in a solution of $Zn(NO_3)_2$, NaCl, and H_2O_2 at -0.8V I believe that the proper periodicity can be achieved. Pulsed deposition should be further investigated, as it would cause more adatom adsorption on the surface of the electrode which would increase the nuclear density effectively giving us another way to achieve the proper periodicity. To achieve the peak height of 400nm for these structures more research is required. One possibility is depositing ZnO nanowires through electrodeposition using previously developed methods,[45,47] Lastly, patterning a photoresist layer using laser interference lithography could be experimentally tested with an ArF laser to develop a template-assisted electrodeposition technique. Then deposition can be completed in the patterned photoresist array to create the moth-eye array with the height and periodicity.

7.2.2 Characterization

The refractive indexes should be measured using ellipsometry techniques to understand and demonstrate the gradual increase in refractive index. Transmission mode UV-VIS should be performed on silicon substrates to understand the optical characteristics of ZnO in the infrared. After a working moth-eye array is formed, device to device reproducibility has to be characterized by all aforementioned characterizing techniques in this study, to demonstrate that this self-assembled ZnO moth-eye array is robust enough for industry use and mass produced in the future to come.

References

1. Klein, J. & Rednam, A. Comparative Costs of California Central Station Electricity Generation Technologies. (2007).

2. Sohrabi, F., Nikniazi, A. & Movla, H. Optimization of Third Generation Nanostructured Silicon-Based Solar Cells. (2013).

3. Solanki, C. S. *Solar photovoltaics: fundamentals, technologies and applications*. (PHI Learning Pvt. Ltd., 2011).

4. Swatowska, B., Stapinski, T., Drabczyk, K. & Panek, P. The role of antireflective coatings in silicon solar cells–the influence on their electrical parameters. *Optica Applicata* **41,** 487–492 (2011).

5. Wilson, S. J. & Hutley, M. C. The optical properties of'moth eye'antireflection surfaces. *Journal of Modern Optics* **29,** 993–1009 (1982).

6. Yamada, N., Kim, O. N., Tokimitsu, T., Nakai, Y. & Masuda, H. Optimization of anti-reflection moth-eye structures for use in crystalline silicon solar cells. *Progress in Photovoltaics: Research and Applications* **19,** 134–140 (2011).

7. Sun, C.-H., Jiang, P. & Jiang, B. Broadband moth-eye antireflection coatings on silicon. *Applied Physics Letters* **92,** 061112–061112 (2008).

8. Boden, S. A. & Bagnall, D. M. Optimization of moth-eye antireflection schemes for silicon solar cells. *Progress in Photovoltaics: Research and Applications* **18,** 195–203 (2010).

9. Raut, H. K. *et al.* Porous SiO< sub> 2</sub> anti-reflective coatings on large-area substrates by electrospinning and their application to solar modules. *Solar Energy Materials and Solar Cells* **111,** 9–15 (2013).

10. Cui, H., Pillai, S., Campbell, P. & Green, M. A novel silver nanoparticle assisted texture as broadband antireflection coating for solar cell applications. *Solar Energy Materials and Solar Cells* **109,** 233–239 (2013).

11. Chen, Q. *et al.* Broadband moth-eye antireflection coatings fabricated by low-cost nanoimprinting. *Applied Physics Letters* **94,** 263118–263118 (2009).
12. Diedenhofen, S. L. *et al.* Broad-band and Omnidirectional Antireflection Coatings Based on Semiconductor Nanorods. *Advanced Materials* **21,** 973–978 (2009).
13. Christian, G. D. *Analytical chemistry*. (Wiley, 2003).
14. Fowles, G. *Introduction to Modern Optics*. (Dover Publications Inc., 1989).
15. Pedrotti, F. L., Pedrotti, L. S. & Pedrotti, L. M. *Introduction to Optics*. (Pearson Prentice Hall, 2008).
16. Kumar, B., Baskara Pandian, T., Sreekiran, E. & Narayanan, S. Benefit of dual layer silicon nitride anti-reflection coating. in *Photovoltaic Specialists Conference, 2005. Conference Record of the Thirty-first IEEE* 1205–1208 (2005).
17. Zhao, J. & Green, M. A. Optimized antireflection coatings for high-efficiency silicon solar cells. *Electron Devices, IEEE Transactions on* **38,** 1925–1934 (1991).
18. Aydin, C., Zaslavsky, A., Sonek, G. J. & Goldstein, J. Reduction of reflection losses in ZnGeP2 using motheye antireflection surface relief structures. *Applied Physics Letters* **80,** 2242–2244 (2002).
19. Wenham, S. R., Green, M. A., Watt, M. E., Corkish, R. & Sproul, A. *Applied photovoltaics*. (Routledge, 2011).
20. Solak, H. H. *et al.* Sub-50 nm period patterns with EUV interference lithography. *Microelectronic engineering* **67,** 56–62 (2003).
21. Hobbs, D. S. *et al.* Automated interference lithography systems for generation of sub-micron feature size patterns. in *Proc. SPIE* **3879,** 124 (1999).
22. Hobbs, D. S. & MacLeod, B. D. Design, fabrication, and measured performance of anti-reflecting surface textures in infrared transmitting materials. in *Proc. SPIE* **5786,** 349–364 (2005).

23. Jiang, P. & McFarland, M. J. Large-scale fabrication of wafer-size colloidal crystals, macroporous polymers and nanocomposites by spin-coating. *Journal of the American Chemical Society* **126,** 13778–13786 (2004).

24. Jiang, P., Prasad, T., McFarland, M. J. & Colvin, V. L. Two-dimensional nonclose-packed colloidal crystals formed by spincoating. *Applied Physics Letters* **89,** 011908–011908 (2006).

25. Kanamori, Y., Roy, E. & Chen, Y. Antireflection sub-wavelength gratings fabricated by spin-coating replication. *Microelectronic Engineering* **78–79,** 287–293 (2005).

26. Wu, J.-J. & Liu, S.-C. Low-temperature growth of well-aligned ZnO nanorods by chemical vapor deposition. *Advanced Materials* **14,** 215 (2002).

27. Kong, Y. C., Yu, D. P., Zhang, B., Fang, W. & Feng, S. Q. Ultraviolet-emitting ZnO nanowires synthesized by a physical vapor deposition approach. *Applied Physics Letters* **78,** 407–409 (2001).

28. Sun, X. W. & Kwok, H. S. Optical properties of epitaxially grown zinc oxide films on sapphire by pulsed laser deposition. *Journal of Applied Physics* **86,** 408–411 (1999).

29. Islam, M. R. & Podder, J. Optical properties of ZnO nano fiber thin films grown by spray pyrolysis of zinc acetate precursor. *Crystal Research and Technology* **44,** 286–292 (2009).

30. Pauporté, T. & Lincot, D. Hydrogen peroxide oxygen precursor for zinc oxide electrodeposition I. Deposition in perchlorate medium. *Journal of the Electrochemical Society* **148,** C310–C314 (2001).

31. Goux, A., Pauporté, T., Chivot, J. & Lincot, D. Temperature effects on ZnO electrodeposition. *Electrochimica acta* **50,** 2239–2248 (2005).

32. Peulon, S. & Lincot, D. Cathodic electrodeposition from aqueous solution of dense or open-structured zinc oxide films. *Advanced Materials* **8,** 166–170 (2004).

33. Mahalingam, T., John, V. S., Raja, M., Su, Y.-K. & Sebastian, P. J. Electrodeposition and characterization of transparent ZnO thin films. *Solar energy materials and solar cells* **88,** 227–235 (2005).

34. Fahoume, M. *et al.* Growth and characterization of ZnO thin films prepared by electrodeposition technique. *Solar energy materials and solar cells* **90,** 1437–1444 (2006).

35. Elias, J., Tena-Zaera, R. & Levy-Clement, C. Effect of the Chemical Nature of the Anions on the Electrodeposition of ZnO Nanowire Arrays. *J. Phys. Chem. C* **112,** 5736–5741 (2008).

36. Puippe, J. C. & Leaman, F. *Theory and Practice of Pulse Plating*. (American Electroplater and Surface Finishers Society, 1986).

37. Bard, A. & Faulkner, L. *Electrochemical Methods: Fundamentals and Applications.* **2,** (Wiley, 1980).

38. Budevski, E. B., Staikov, G. T. & Lorenz, W. J. *Electrochemical phase formation and growth: an introduction to the initial stages of metal deposition*. (John Wiley & Sons, 2008).

39. Budevski, E., Staikov, G. & Lorenz, W. J. Electrocrystallization: nucleation and growth phenomena. *Electrochimica Acta* **45,** 2559–2574 (2000).

40. Guo, L. & Searson, P. C. On the influence of the nucleation overpotential on island growth in electrodeposition. *Electrochimica Acta* **55,** 4086–4091 (2010).

41. Gunawardena, G., Hills, G., Montenegro, I. & Scharifker, B. Electrochemical nucleation: Part I. General considerations. *Journal of Electroanalytical Chemistry and Interfacial Electrochemistry* **138,** 225–239 (1982).

42. Marotti, R. E., Guerra, D. N., Bello, C., Machado, G. & Dalchiele, E. A. Bandgap energy tuning of electrochemically grown ZnO thin films by thickness and electrodeposition potential. *Solar energy materials and solar cells* **82,** 85–103 (2004).

43. Pauporté, T. & Lincot, D. Hydrogen peroxide oxygen precursor for zinc oxide electrodeposition II—Mechanistic aspects. *Journal of Electroanalytical Chemistry* **517,** 54–62 (2001).

44. Liu, X., Jin, Z., Bu, S., Zhao, J. & Liu, Z. Growth of ZnO films with controlled morphology by aqueous solution method. *Journal of the American Ceramic Society* **89,** 1226–1231 (2006).

45. Elias, J., Tena-Zaera, R. & Levy-Clement, C. Electrochemical deposition of ZnO nanowire arrays with tailored dimensions. *Journal of Electroanalytical Chemistry* **621,** 171–177 (2008).

46. Peulon, S. & Lincot, D. Mechanistic study of cathodic electrodepositionof zinc oxide and zinc hydroxychloride films from oxygenated aqueous zinc chloride solutions. *Journal of electrochemical society* **145,** 864–874

47. Tena-Zaera, R., Elias, J., Wang, G. & Levy-Clement, C. Role of Chloride Ions on Electrochemical Deposition of ZnO Nanowire Arrays from O2 Reduction. *Journal of Physical Chemistry C* **111,** 16706–16711 (2007).

48. Sigmund, P. *Sputtering by ion bombardment theoretical concepts*. (Springer, 1981).

49. Sigmund, P. Mechanisms and theory of physical sputtering by particle impact. *Nuclear Instruments and Methods in Physics Research Section B: Beam Interactions with Materials and Atoms* **27,** 1–20 (1987).

50. Bertran, E. *et al.* RF sputtering deposition of Ag/ITO coatings at room temperature. *Solid State Ionics* **165,** 139–148 (2003).

51. Hiramatsu, H. *et al.* Preparation of transparent p-type (La< sub> 1- x</sub> Sr< sub> x</sub> O) CuS thin films by rf sputtering technique. *Thin Solid Films* **411,** 125–128 (2002).

52. East, G. A. & del Valle, M. A. Easy-to-make Ag/AgCl reference electrode. *Journal of Chemical Education* **77,** 97 (2000).

53. Model 600D Series Electrochemical Analyzer/workstation - User manual. (2011).

54. Chen, Q.-P., Xue, M.-Z., Sheng, Q.-R., Liu, Y.-G. & Ma, Z.-F. Electrochemical growth of nanopillar zinc oxide films by applying a low concentration of zinc nitrate precursor. *Electrochemical and solid-state letters* **9,** C58–C61 (2006).

55. Chong, W., Fei-Fei, W., Xing-Qiu, F. & Tai-Hong, W. Electrodeposition of aligned ZnO sheet array on ITO substrate and their field emission characteristics. *Chinese Physics* **16,** 3545 (2007).

56. Vayssieres, L. Growth of arrayed nanorods and nanowires of ZnO from aqueous solutions. *Advanced Materials* **15,** 464–466 (2003).

57. Campos, L. C., Guimaraes, M. H. D., Goncalves, A.-M. B., de Oliveira, S. & Lacerda, R. G. *ZnO UV photodetector with controllable quality factor and photosensitivity*. (2013).

58. Zhang, X., Huang, X., Li, C. & Jiang, H. Dye-Sensitized Solar Cell with Energy Storage Function through PVDF/ZnO Nanocomposite Counter Electrode. *Advanced Materials* **25,** 4093–4096 (2013).

59. Goldstein, J. *et al. Scanning electron microscopy and X-ray microanalysis*. (Springer, 2003).

60. Scanning electron microscopy 'Short review of SEM principles'.

61. He, B. B. *Two-dimensional x-ray diffraction*. (Wiley, 2009).

62. Gal, D., Hodes, G., Lincot, D. & Schock, H.-W. Electrochemical deposition of zinc oxide films from non-aqueous solution: a new buffer/window process for thin film solar cells. *Thin Solid Films* **361,** 79–83 (2000).

63. Scharifker, B. & Hills, G. Theoretical and experimental studies of multiple nucleation. *Electrochimica Acta* **28,** 879–889 (1983).

64. Avrami, M. Kinetics of phase change. I General theory. *The Journal of Chemical Physics* **7,** 1103 (1939).

Appendix A

Sample Preparation Procedures

In this case, ITO was the target and glass microscope slides were the substrates. The VWR microscope glass slides were cleaned by spraying ACS (American Chemical Society) grade isopropanol (Caledon Laboratory Chemicals) on the glass and then wiped with a Kim wipe. Three glass slides were inserted into the Centre of Emerging Device Technologies (CEDT) sputtering machine. The chamber was then sealed and brought down to vacuum pressure (~10^{-6}-10^{-7} Torr), which took approximately 6 hours. Once at vacuum pressure, the parameters were set. The thickness of the layer was inputted to be 200 nm, the potential at the target using RF was set to 60V, and the glow tube used to create the argon plasma was set to 20V. The system was then initiated and the deposition rate recorded by the system was approximately 10 nm per minute. After approximately 20 minutes, the sputtering machine would shut off when the required thickness of 200 nm of ITO on the glass substrate was reached. The ITO samples were then put into a rapid thermal annealer (RTA) directly after deposition, in order to change the electrical properties of the ITO. Before being placed in the RTA, the resistance of the ITO was measured using a multi-meter and two leads separated by approximately half a centimeter; the recorded resistance was over 1000 ohms in multiple locations. Then the samples were inserted into the RTA for 300 seconds at 400ºC. After a cooling down period of 10 minutes, the samples' resistances were in the range of 80-100 ohms in multiple locations. After sputtering the Glass-ITO substrates, they were cleaned by sonication in reagent ACS grade acetone and methanol (Caledon Laboratory Chemicals) for 20 minutes in each solution, and then rinsed in deionized water. Lastly, the samples were dried with an air gun and ready for electrodeposition.

Electrodeposition Procedures

Our vision was to use both $ZnCl_2$ (Sigma Aldrich) and $Zn(NO_3)_2$ (Sigma Aldrich) salts, while using hydrogen peroxide (reagent ACS grade from Caledon Laboratory Chemicals) as the oxygen precursor, to form structures in the nanoscale with a deposition time of under a minute. However, when using high concentrations of both of these salts, other materials can become deposited on the surface of the electrode so precautions are needed.[30,43] The following procedure was used for the ZnO depositions in this research.

The procedure for the electrodeposition of ZnO was completed in the following steps, and this is a general procedure. The specific solutions and parameters used are summarized in Table 1.

1) ITO-coated glass samples from Table 1, which were cleaned and processed using the method in Section 4.3.1, were used for electrodeposition.
2) A 6x6mm square area was created in Adobe Illustrator. The pattern was reproduced 60 times with each square positioned 2cm away from the other, over the entire sheet. This desired pattern was cut into self-adhesive vinyl sheets (FDC-4300, FDC graphic films, South Bend,

Indiana) using a Robo Pro CE5000-40-CRP vinyl cutter (Graphtec America Inc., Irvine, CA) equipped with a CB09UA supersteel blade with force, quality and speed set at 10, 1, and 1 respectively.

3) The origin on the vinyl cutter was set to the bottom left of the page to correspond with the bottom left of the page of the masked pattern (60 - 6x6mm squares per page) referenced as its starting point.

4) The 60 squares were cut using the cutter tool which was interfaced with the computer.

5) The self-adhesive vinyl sheets were cut to match the exact dimensions of the ITO sample (different dimensions for all pieces, but approximately 1.5x0.8cm) with the 6x6mm square exposed in the centre. Before adhesion, a small manual cut was made outside the deposition area for the working electrode wire to make its connection to the ITO.

6) The self-adhesive vinyl was then attached to the ITO.

7) The 25mL solution from Table 1 was heated to the required temperature also in Table 1.

8) Once the solution reached the required temperature, a 2 minute wait was initiated to allow the solution to stabilize.

9) During this time, the masked substrate was connected to the mini-grabber which was connected to the working electrode-labelled wire of the potentiostat.

10) The chronoamperometry technique was selected in the CHI660d beta software and a ‘Parameters’ window was then displayed. The voltage and time used correspond to values in Table 1. The quiet time was always set to zero, the sensitivity was set to 0.001 A so the measurement was recorded on the milliampere scale, and the sample interval was set to 0.001 seconds. These three parameters hold constant for all electrodeposition experiments.

11) Once the 2 minutes passed, the 3 electrodes were placed in solution with the reference electrode 1-2 mm away from the other 2 in an equilateral triangular formation.

12) The experiment was then run and an I vs. t curve was displayed for the deposition completed.

13) The 3 electrodes were taken out of the solution, washed in deionized water, and the electrodeposited surface was dried with an air gun.

14) The solution was then cooled and thrown into the proper waste container.

15) This procedure was repeated until all samples were completed.

Substrate	Voltage (V)	Time(s)	Solution	Solution Temp. (^oC)	Deposition Method
ITO	-1.1	120	0.05M $ZnCl_2$ and 0.025M H_2O_2	25,65,80	Constant Voltage
ITO	-0.8,-1.1,-1.4,-1.7,-2.0	120	0.05M $ZnCl_2$ and 0.025M H_2O_2	65	Constant Voltage
ITO	-1.1	10-20-30-40	0.05M $ZnCl_2$ and 0.025M H_2O_2	65	Constant Voltage
ITO	-1.1	10-20-30-40	0.005M $ZnCl_2$ and 0.0025M H_2O_2	65	Constant Voltage
ITO	-1.1	10-20-30-40	0.05M $Zn(NO_3)_2$ and 0.025M H_2O_2	65	Constant Voltage
ITO	-1.1	10-20-30-40	0.005M $Zn(NO_3)_2$ and 0.0025M H_2O_2	65	Constant Voltage
ITO	-0.8	10-20-30-40	0.05M $Zn(NO_3)_2$ and 0.025M H_2O_2	65	Constant Voltage
ITO	-1.1	10-20-30-40	0.05M $Zn(NO_3)_2$, 0.05M NaCl and 0.025M H_2O_2	65	Constant Voltage
ITO	-1.1	120	0.05M $Zn(NO_3)_2$, 0.05M NaCl and 0.025M H_2O_2	65	Constant Voltage
ITO	-1.1	120	0.05M $Zn(NO_3)_2$, 0.025M H_2O_2	65	Constant Voltage
ITO	-1.1	120	0.05M $Zn(NO_3)_2$, 0.005M NaCl and 0.025M H_2O_2	65	Constant Voltage
ITO	-1.1	120	0.05M $Zn(NO_3)_2$, 0.1M NaCl and 0.025M H_2O_2	65	Constant Voltage
Silicon	-1.1	120	0.05M $Zn(NO_3)_2$ and 0.025M H_2O_2	65	Constant Voltage
Silicon	-1.1	240	0.05M $Zn(NO_3)_2$ and 0.025M H_2O_2	65	Constant Voltage
Silicon	-1.1	120-30s off-120	0.05M $Zn(NO_3)_2$ and 0.025M H_2O_2	65	Pulsed Voltage

Table 1: Electrodeposition Parameters

Electrodeposition on Silicon

The silicon [(100) one side-polished silicon] used for electrodeposition was also properly cleaned using the following procedure that effectively cleans the silicon substrate and removes the silicon dioxide layer prior to electrodeposition (this cleaning method is from the McMaster University ENG PHYS 4U04 Solar Cell Fabrication course):

1) A solution containing 150 mL of H_2O_2 (30%) (Caledon Laboratory) and 75 mL of sulfuric acid (95-98%) (ACS reagent grade from Sigma Aldrich) was brought to a temperature of 80^{o}C.
2) The silicon substrates were inserted into the solution for 10 minutes.
3) The substrates were then taken out and rinsed with deionized water for 5 minutes.
4) A solution of 100 mL of deionized water, 25 mL of H_2O_2 (30%), and 25 mL of ACS reagent grade hydrochloric acid (37%) (Sigma Aldrich) was brought to a temperature of 80^{o}C.
5) The silicon substrates were inserted into the solution for 10 minutes.
6) The substrates were then taken out and rinsed with deionized water for 5 minutes.
7) A solution of 100 mL of deionized water and 25 mL of ACS reagent grade hydrofluoric acid (48%) (Sigma Aldrich) was made at room temperature.
8) The silicon substrates were inserted into the solution for 2 minutes.
9) The substrates were then taken out and rinsed with deionized water for 5 minutes.
10) The electrodeposition procedure then commenced.

Patterning ZnO

The Top-down + bottom-up method used for fabrication:

1) Futurrex NR9-1500 negative photoresist was spun on the ITO at 4000 rpm for 30 seconds.

2) A UV mask aligner was used that had exposure energy of 40mJ, which corresponds to an exposure time of approximately 9 seconds.

3) The sample was then developed in RD6 Developer at room temperature for 1 minute.

4) The electrodeposition procedure from Section 3.4 was then conducted.

5) The sample was then rinsed in acetone until photoresist was fully removed (approximately 2 minutes) and then rinsed in deionized water and dried with the air gun.

In the Bottom-up + top-down method, electrodeposition took place first (general procedure in Section 4.3.2) and the lithographic steps followed:

1) S1827 positive photoresist was spun on at 4000 rpm for 30 seconds.

2) The sample was then exposed at 116mJ, which corresponds to an exposure time of approximately 2 minutes.
3) The sample was developed in microdeposit 351 at room temperature for 40 seconds. The same pattern shown in Figure 29 was created over a layer of ZnO (Figure 30b).

4) The sample was then etched with a 1:1:30 solution of phosphoric acid (2mL) (85% - reagent grade from Fisher Scientific), acetic acid (2mL) (99.7%, Glacial from Caledon Laboratories) and deionized water (60mL) for 25 seconds at room temperature.

5) The sample was then rinsed in acetone until photoresist was fully removed (approximately 2 minutes) and then rinsed in deionized water and dried with the air gun.

6) The result was the completion of two patterning fabrication methods for these ZnO electrodeposited films.

Appendix B

Scanning Electron Microscopy

Scanning electron microscopy is a characterization technique used to show the topographical images of a specimen with a resolution in the nanometer scale. It also has the advantage of being integrated with an X-ray detector for elemental analysis. The SEM system used to analyze all of the samples was the JEOL 7000 located in the Canadian Centre for Electron Microscopy (CCEM).

The SEM system consists of many parts that help capture an image, which are shown in Figure B1. The electron gun is the source that generates a stable electron beam with adjustable energy.[59] This electron beam then travels through condenser lenses, which are magnetic lenses that concentrate the electron beam. The condenser lens concentrates the electron beam using the magnetic Lorentz force.

$$F = qv \times B \tag{5.1.1}$$

By applying a magnetic field on an electron moving with the speed of v, one can effectively force the electron on a certain path. The beam then travels through the scan coils – excited by an applied current – which affects the overall magnification of the image. These coils are electromagnetic deflection coils, which cause the beam to deflect over certain distances. For example, for a high magnification image (zoomed in image), a low current is applied to the scan coils so the resulting magnetic field cannot deflect the beam over a large distance and consequently, the beam is focused on a smaller area on the sample.[59] Therefore, strongly excited coils, through a high applied current, can force the electron beam to deflect over larger distances causing the image to be at a smaller magnification. This is not the only control with respect to magnification; the working distance also affects the image. This is the distance from the final lens (the objective lens) and the sample. As aforementioned, the beam finally passes through the objective lens and focuses the electron beam on the sample. This lens also helps with additional demagnification. The objective lens is controlled by the current that is supplied through its windings by the use of the focus knob. Between this lens is a stigmator and a beam limiting aperture which minimize aberrations and control the depth of focus.[59] The stigmator corrects for astigmatism, which is when electrons diverge from a certain point and produce two separate line foci which create two different focusing planes that do not coincide. This causes the image to be blurred due to overlapping planes of focus. The stigmator, which is a series of small electromagnetic coils, supplies a weak magnetic field to the beam correcting for the objective lens and making it symmetric to the electron beam, which effectively forces the two line foci to coincide.[59]

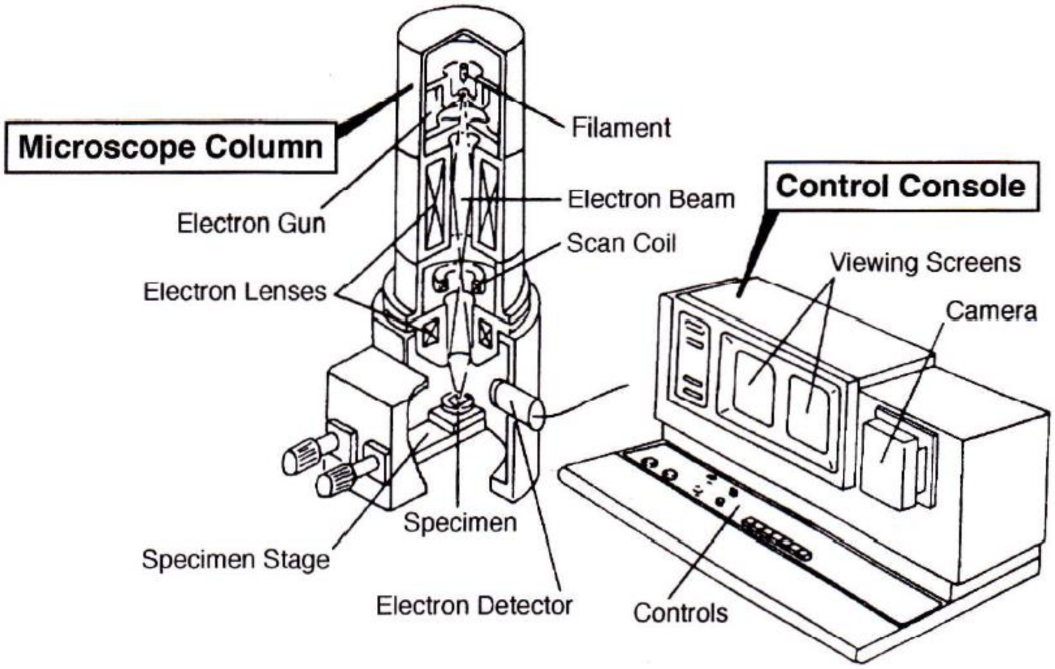

Figure B1: Diagram of a scanning electron microscopy system.[59]

The incident electron beam then interacts with the surface of the specimen, generating secondary (SE) and backscattered (BSE) electrons which are then detected by electron detectors. Secondary electrons are emitted from the surface as they are knocked out of the valence orbitals of the surface atoms.[59] These electrons create a 3D quality image of the surface in the area of interest. The SE projection depends on the angle of the incoming beam; therefore, steep surfaces and edges appear brighter, resulting in an image that has defined features.[59] When a SE hits the detector it collides with a scintillator/phosphor and light is emitted.[59] The light goes through total internal reflection in a light guide, then enters the photomultiplier where at the photocathode the photons are converted back into electrons and converted to point-by-point intensity changes on the screen, generating an image.[59] BSEs are beam electrons which escape the sample as a result of multiple elastic scattering, carrying information on sample composition, topography, and crystallinity.[59] BSEs usually have energies higher than 10keV, while 90% of SE energies are lower than 10keV.[59] Therefore, BSE detectors have only a passive phosphor so that SEs without high enough energy are not allowed to pass through, allowing only BSEs to be collected.

X-ray Diffraction

XRD occurs when a monochromatic X-ray beam hits a sample at a certain angle, at which the diffracted X-rays scatter away from the sample at the same angle and wavelength. This is shown in Figure B2.[61]

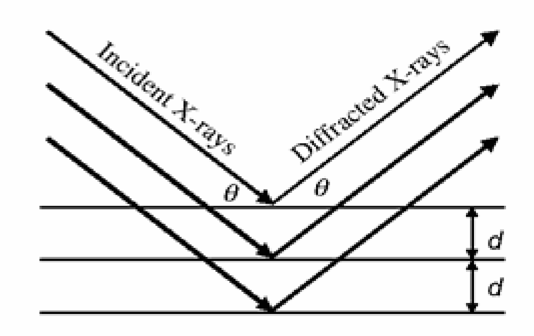

Figure B2: X-ray diffraction: The incident and diffracted X-rays symmetric to the normal of the crystal plane.[61]

This angle is known as the Bragg angle. At this angle, diffraction maxima can occur based on atomic arrangement. However, this is only true if Bragg's Law is satisfied:

$$n\lambda = 2d\sin\theta \tag{5.3.1}$$

where λ is the wavelength of the monochromatic X-ray, d is the distance between each adjacent atomic plane, θ is the Bragg angle, and n is an integer number referred to as the order of reflection.[61] When using a single wavelength, the order of reflection is always 1. The order of reflection is used for multiple wavelength analysis to define equivalent XRD patterns. For example, it shows that θ can be calculated at a wavelength of 0.4 μm and is equal to θ at 0.8 μm due to both wavelengths having the same diffraction pattern for the given d-spacing, which stays constant.[61] In order to find the composition of a certain material, two-dimensional X-ray diffraction is implemented by taking Bragg's Law and expanding it in 3D space to form a 2θ diffraction cone which is demonstrated in Figure B3. Θ is the angle of the diffracted beam normal to the surface on both sides of the substrate, forming a cone. This diffraction pattern is what the detector collects and displays. There are five major parts to an XRD system, also shown in Figure B3. The first part is an X-ray source that produces a beam of monochromatic X-rays. X-rays are formed in an X-ray tube when a high voltage is used to accelerate electrons from a cathode to a metal target (the anode); the end result is the production of X-rays. Second are the X-ray optics; diverging X-rays from the X-ray tube come in contact with a device called a Gobel mirror, which is a single crystal mirror that is curved in a way that produces parallel beams of X-rays.[61] The intensity of these X-rays is calculated using an intensity meter in place of the sample holder. The Gobel mirror is adjusted until the intensity is optimized, controlling the focus of the X-ray beams. If out of focus, some X-ray beams may be diverging, which causes the diffraction pattern features to be larger. For example, diffraction rings would have larger thicknesses than normal. The third major part is the sample holder, which helps adjust the position between the detector and X-ray source. Fourth is the sample alignment and monitor to keep the sample in position. Lastly is the detector, which transfers the diffraction pattern to a 2D image. The detector used in the McMaster XRD facility is the 2D Smart 6000 Detector with a 512x512 pixel range. It uses a charge-coupled device (CCD), which detects X-ray photons indirectly.[61] Most CCD X-ray detectors first convert the X-ray photons to visible light photons by passing through a material layer known as a phosphor. The phosphor absorbs X-ray photons and emits visible photons that are detected by the CCD. This detector is cooled (to -54ºC) by a chiller to help reduce electronic noise. The XRD pattern is then displayed in a 2D image.

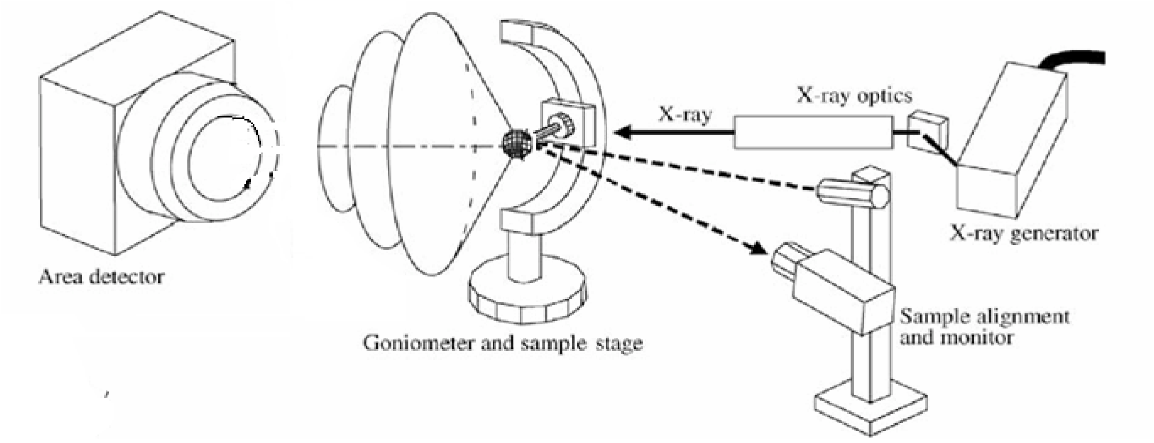

Figure B3: X-ray diffraction experimental apparatus with magnified 2θ diffraction cone pattern.[3]

UV-Vis Spectroscopy

Incident light can behave in three different ways when coming into contact with an interface between two media; it can be reflected, transmitted, or absorbed. This is shown in Figure B4 and explained in detail in Section 2.1. The molecules in the sample can absorb radiation in three different ways. The first is through a rotational transition. As the molecules are rotating with a definite energy, they can absorb radiation and move into a higher rotational energy state.[13] This occurs mostly in the infrared. The second type of transition is a vibrational transition. This occurs near the infrared, acts the same as the rotational transition, and can also have a mixed rotational and vibrational transition. The third transition which occurs mainly in the ultraviolet and visible range is the electronic transition. This occurs when radiation at small wavelengths is absorbed by the electrons which then force them into a higher electron energy state. Once the energy is absorbed however, it does not stay in the excited state very long and will usually transition back to its ground state.[13]

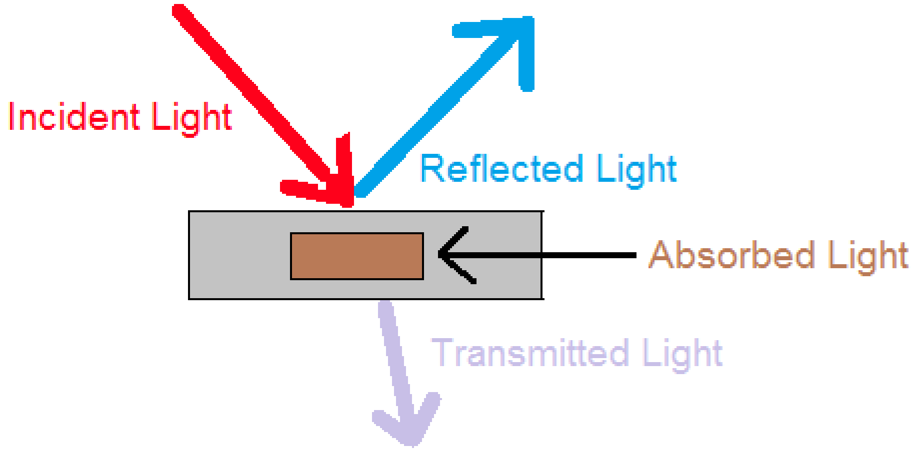

Figure B4: The three ways incident light can behave at the interface of two media.